ANNUAL REPORT 2002

Optoelectronics Department

University of Ulm

Contents

1: Eckart Schiehlen
2: Martin Stach
3: Christoph Eichler
4: Eckard Deichsel
5: Manfred Mundbrod
6: Hendrik Roscher
7: Marcus Scherer
8: Rainer Michalzik
9: Georgi Stareev
10: Jürgen Mähnß
11: Steffen Lorch
12: Felix Mederer
13: James O'Callaghan
14: Vincent Voignier
15: Frank Demaria
16: Barbara Neubert
17: Frank Habel
18: Rainer Blood
19: Peter Unger
20: Johannes M. Ostermann
21: Matthias Seyboth
22: Michael C. Riedl

Missing in the picture

23: Irene Ecker
24: Ihab Kardosh
25: Max Kicherer
26: Fernando Rinaldi
27: Sven-Silvius Schad
28: Pavel Ivanov
29: Matthias Golling
30: Heiko J. Unold
31: Safwat W.Z. Mahmoud
32: Thomas Knödl
33: Karl J. Ebeling
34: Hildegard Mack
35: Susanne Menzel
36: Sophie Pfetsch
37: Gerlinde Meixner
38: Josef Theisz

Optoelectronics Department University of Ulm

Albert-Einstein-Allee 45, D-89081 Ulm, Germany
Fax: +49–731/50–2 60 49
Phone: +49–731/50–

Intermediate Head of Department

Prof. Dr.	Peter Unger	–2 60 54	peter.unger@e-technik.uni-ulm.de

Assistant Head

Prof. Dr.	Ferdinand Scholz	–2 60 52	ferdinand.scholz@e-technik.uni-ulm.de

On leave at Infineon Technologies AG

Prof. Dr.	Karl Joachim Ebeling	–2 60 51	karl.ebeling@e-technik.uni-ulm.de

Senior Research Assistant

Dr.-Ing.	Rainer Michalzik	–2 60 48	rainer.michalzik@e-technik.uni-ulm.de

Cleanroom Management

Dr.-Ing.	Jürgen Mähnß	–2 60 53	juergen.maehnss@e-technik.uni-ulm.de

Secretaries

	Christine Bunk	–2 60 50	christine.bunk@e-technik.uni-ulm.de
	Hildegard Mack	–2 60 59	hildegard.mack@e-technik.uni-ulm.de

Research Staff

Dipl.-Ing.	Eckard Deichsel	–2 60 57	eckard.deichsel@e-technik.uni-ulm.de
Dipl.-Phys.	Frank Demaria	–2 60 46	frank.demaria@e-technik.uni-ulm.de
Dipl.-Ing.	Irene Ecker	–2 60 41	irene.ecker@e-technik.uni-ulm.de
Dipl.-Ing.	Christoph Eichler	–2 61 95	christoph.eichler@e-technik.uni-ulm.de
Dipl.-Ing.	Eckart Schiehlen	–2 60 57	eckart.schiehlen@e-technik.uni-ulm.de
Dipl.-Ing.	Matthias Golling*	–2 60 35	matthias.golling@e-technik.uni-ulm.de
Dipl.-Ing.	Frank Habel	–2 64 52	frank.habel@e-technik.uni-ulm.de
Dipl.-Ing.	Pavel Ivanov*	–2 60 38	pavel.ivanov@e-technik.uni-ulm.de
Dipl.-Phys.	Roland Jäger*	–2 60 40	roland.jaeger@e-technik.uni-ulm.de
Dipl.-Ing.	Jürgen Joos*	–2 60 35	juergen.joos@e-technik.uni-ulm.de
Dipl.-Ing.	Ihab Kardosh	–2 60 36	ihab.kardosh@e-technik.uni-ulm.de
Dipl.-Phys.	Max Kicherer*	–2 60 37	max.kicherer@e-technik.uni-ulm.de
Dipl.-Ing.	Roger King*	–2 60 40	roger.king@e-technik.uni-ulm.de
Dipl.-Ing.	Thomas Knödl*	–2 60 38	thomas.knoedl@e-technik.uni-ulm.de
Dipl.-Ing.	Steffen Lorch	–2 60 39	steffen.lorch@e-technik.uni-ulm.de
M.S.	Safwat W.Z. Mahmoud*	–2 60 44	safwat.mahmoud@e-technik.uni-ulm.de
Dipl.-Ing.	Felix Mederer*	–2 60 37	felix.mederer@e-technik.uni-ulm.de
Dipl.-Phys.	Michael Miller*	–2 60 36	michael.miller@e-technik.uni-ulm.de
Dipl.-Phys.	Manfred Mundbrod	–2 60 39	manfred.mundbrod@e-technik.uni-ulm.de
Dipl.-Ing.	Barbara Neubert	–2 64 54	barbara.neubert@e-technik.uni-ulm.de
M.Sc.	James O'Callaghan	–2 60 36	james.ocallaghan@e-technik.uni-ulm.de
Dipl.-Phys.	Johannes M. Ostermann	–2 60 38	johannes-michael.ostermann@ e-technik.uni-ulm.de
Dipl.-Ing.	Michael C. Riedl	–2 60 36	michael.riedl@e-technik.uni-ulm.de
Dipl.-Phys.	Fernando Rinaldi	–2 60 46	fernando.rinaldi@e-technik.uni-ulm.de

Dipl.-Ing.	Hendrik Roscher	–2 60 36	hendrik.roscher@e-technik.uni-ulm.de
Dipl.-Ing.	Sven-Silvius Schad	–2 61 95	sven-silvius.schad@e-technik.uni-ulm.de
Dipl.-Ing.	Marcus Scherer	–2 60 35	marcus.scherer@e-technik.uni-ulm.de
Dipl.-Phys.	Matthias Seyboth	–2 60 35	matthias.seyboth@e-technik.uni-ulm.de
Dipl.-Ing.	Martin Stach	–2 60 37	martin.stach@e-technik.uni-ulm.de
Dr.-Ing.	Georgi Stareev	–2 64 53	georgi.stareev@e-technik.uni-ulm.de
Dipl.-Ing.	Heiko J. Unold*	–2 60 36	heiko.unold@e-technik.uni-ulm.de
Dr.	Vincent Voignier*	–2 60 35	vincent.voignier@e-technik.uni-ulm.de

Technical Staff

	Rainer Blood	–2 60 44	rainer.blood@e-technik.uni-ulm.de
	Gerlinde Meixner	–2 60 41	gerlinde.meixner@e-technik.uni-ulm.de
	Susanne Menzel	–2 60 41	susanne.menzel@e-technik.uni-ulm.de
	Sophie Pfetsch*	–2 60 41	sophie.pfetsch@e-technik.uni-ulm.de
	Josef Theisz	–2 60 30	josef.theisz@e-technik.uni-ulm.de

* Member has left the department meanwhile

Preface

During 2002, the research activities of the Optoelectronics Department have been continuing in the areas of optical interconnect systems, vertical-cavity surface-emitting lasers (VCSELs), GaN-based electronic and optoelectronic devices, optically pumped semiconductor disk lasers, unstable-resonator edge-emitting lasers, and high-power laser amplifiers. The VCSEL and Optical Interconnects Group enjoys ongoing collaboration with the Department's spin-off company U-L-M photonics on various topics of VCSEL characterization and optimization. Research into optical sensing applications as well as an equipment upgrade toward 40 Gbit/s data rate are newcomers on the group's activity list. In the High-Power Semiconductor Laser Group, a continuous optical power of 5 W of a broad-area edge-emitting laser diode at an emission wavelength of 980 nm has been coupled into a 220-μm-core-diameter multi-mode fiber exhibiting a coupling efficiency of more than 80 % and an electrical-to-optical overall system efficiency of 49 %. In the GaN Electronics and Optoelectronics Group, significant improvement for the dislocation density of our GaN layers has been achieved using an optimized Epitaxial Lateral Over-Growth (ELOG) technique. More details on the various research activities can be found in the articles presented in the main part of this report.

In January 2002, Dr. Daniel Hofstetter, assistant professor at the Université de Neuchâtel, joined us for a three-year research fellowship financed by the prize money of the Sofja Kovalevskaja Award, which he received in 2001 from the Alexander von Humboldt Foundation for his pioneering work on optoelectronic devices based on inter-subband transitions. Four members of the department, namely Roland Jäger, Ulrich Martin, Safwat W.Z. Mahmoud, and Michael Miller received their Ph.D. degrees. Also Stefan Bader from Osram Opto Semiconductors and Gunter Steinle from Infineon Technologies successfully finalized their Ph.D. theses under the supervision of Karl Joachim Ebeling who is still heading Infineon's Corporate Research. Furthermore, 7 Diploma or Master Theses and 8 Semester Projects have been carried out in 2002.

The department further intensified the close cooperation with industrial partners. We also appreciate the financial support of national and European research organizations, which contribute the major part of our funding. Numerous publications at international conferences and a large number of articles in respected journals document the strong research activities of the department. A detailed list can be found at the end of this report.

Peter Unger Ulm, January 2003

Dislocation Reduction by GaN MOVPE Growth on Structured Substrates

Frank S. Habel

We reduced the dislocation density of our GaN layers using the Epitaxial Lateral Overgrowth (ELOG) technique. To this end we studied the influence of important growth parameters with respect to vertical and lateral growth rates and the resulting cross section of the grown structures. Using optimized parameters, completely coalesced GaN layers with a low dislocation density in the lateral grown regions can be achieved.

1. Introduction

Due to the rapid progress in the development of high-end GaN based devices such as laser diodes, UV-LEDs and FETs, the demand for low dislocation density substrates is strongly increasing. The dislocation density in common hetero-epitaxially grown GaN on sapphire or silicon carbide substrates is in the order of 10^8-$10^{10}\,\mathrm{cm}^{-2}$, mainly due to the huge lattice mismatch between these substrates and GaN together with the resulting columnar structure of the grown layers. Dislocations have several strong effects on devices [1]. Especially for laser diodes, a low dislocation density is a prerequisite for long device lifetimes. Moreover, dislocations act as non-radiative recombination centers, reducing the efficiency of optoelectronic devices. Carrier mobility is affected by scattering at charged dislocation lines. The formation of V-defects during growth of InGaN quantum wells is correlated with dislocations. Since bulk GaN substrates are still not available for industrial production, other methods to reduce the dislocation density of layers grown on mismatched substrates have to be used.

2. Epitaxial Lateral Overgrowth

Epitaxial Lateral Overgrowth (ELOG) is a well known technique to reduce dislocation density employing structured substrates [2]. A schematic cross section of an ELOG structure is plotted in figure 1. For preparation a mask material is deposited on a template. The mask material is structured using standard lithography and etching methods. Then additional semiconductor material is epitaxially grown on the structured substrate. Growth only occurs in the areas where the template is not covered by the mask. Starting from these areas the crystal grows vertically like on plane substrates but also laterally over the masked regions. The relation between the lateral and vertical growth rates as well as the cross-sectional shape can be controlled by process parameters. The lateral growth rate strongly depends on the crystal direction. When enough material is deposited, adjacent crystal domains coalesce and a plane surface is formed again.

As dislocations usually run vertically from the substrate interface to the surface of the semiconductor, they only occur in the vertically grown "posts" between the mask, whereas the laterally grown "wings" are expected dislocation free.

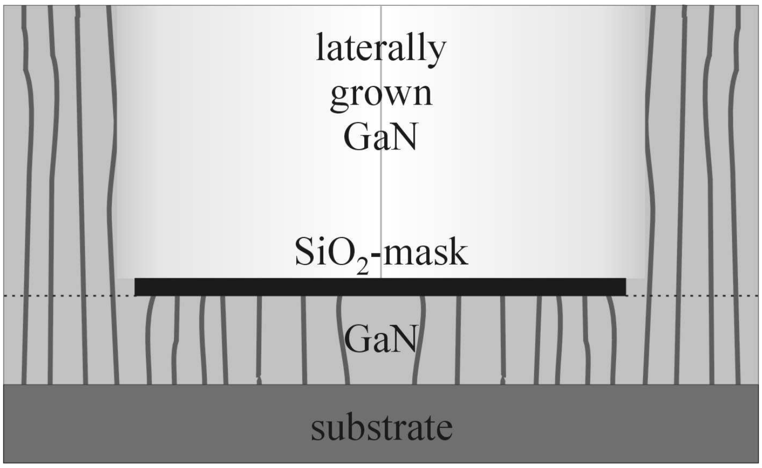

Fig. 1: ELOG schematic.

3. Experiments

3.1 Sample preparation

In our case 1 μm thick GaN layers on sapphire substrate were used as templates. As mask material 250 nm SiO_2 was deposited by PECVD. A pattern consisting of stripes with various widths and distances was chosen to study the influence of the mask geometry. The stripe arrays were orientated along the $\langle 1\bar{1}00\rangle$ or the $\langle 11\bar{2}0\rangle$ direction, respectively. Etching of the mask was performed in a CF_4 RIE system.

3.2 Growth on structured substrates

In first experiments the influence of basic growth parameters was studied. The reactor pressure as well as the process temperature was varied based on standard parameters known from plane substrates. In order to obtain a large lateral grown area, which provides low dislocation density material, a high lateral growth rate is necessary. On the other hand a low overall thickness is needed to avoid cracks. To match both requirements, a high lateral to vertical growth ratio (LTVGR) is required. This value equals the difference of the width of the grown material and the stripe distance divided by two times the grown height [3].

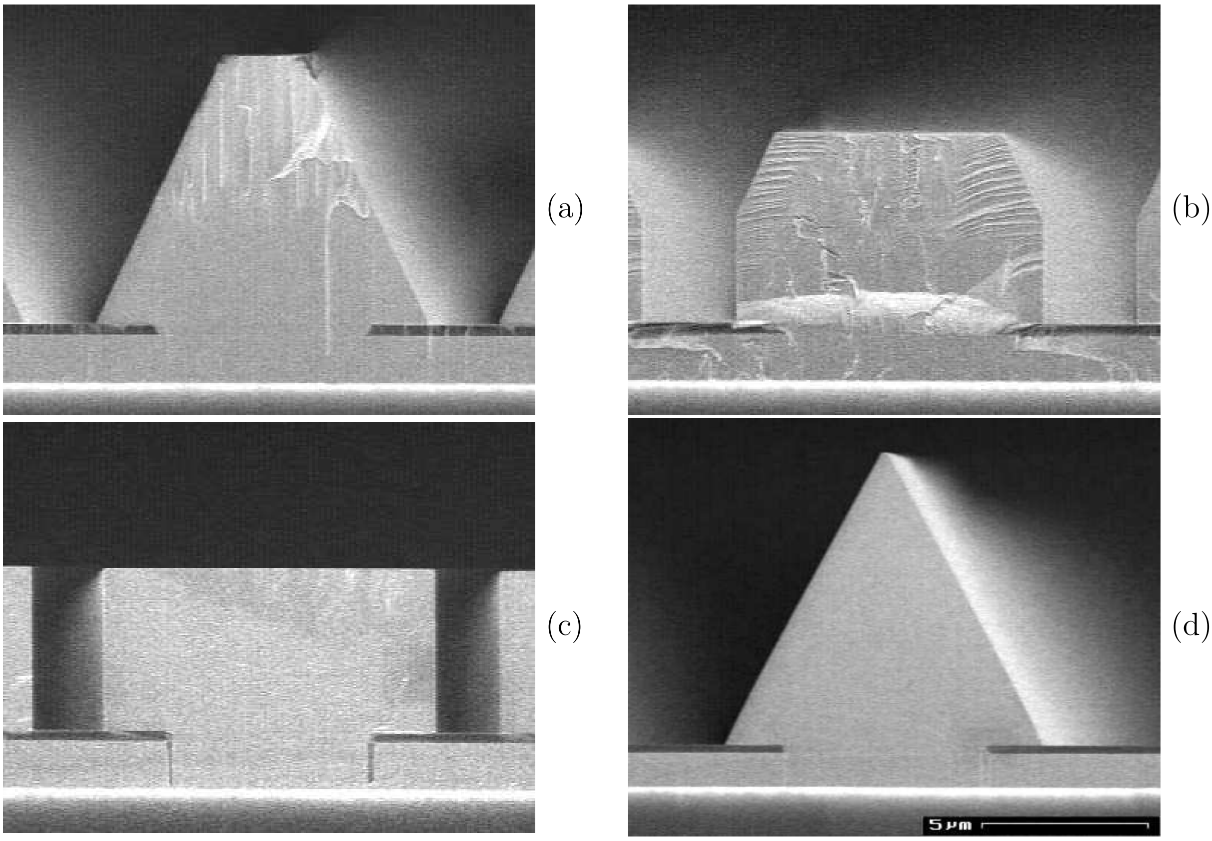

Fig. 2: Varying cross sections for stripes in $\langle 1\bar{1}00\rangle$ direction and growth temperature of 1020°C (a), 1070°C (b) and 1130°C (c); unchanged cross section for stripes in $\langle 11\bar{2}0\rangle$ direction (d).

4. Results

In figures 2a-c the influence of the process temperature on the lateral and vertical growth rates as well as the cross-sectional shape can be seen for ELOG stripes in $\langle 1\bar{1}00\rangle$ direction. For low temperatures a triangular shape with sidewalls formed by $\{11\bar{2}2\}$ facets predominates. With increasing process temperature the shape shifts via a combination of trapezoidal and rectangular to rectangular, confined by $\{11\bar{2}0\}$ facet sidewalls, due to an increasing lateral growth rate. A reduced reactor pressure also leads to an increase in lateral growth. On the other hand no effect of these parameters can be seen for ELOG stripes in $\langle 11\bar{2}0\rangle$ direction, where a triangular cross section was found for all studied sets of parameters because of a strong domination of $\{1\bar{1}01\}$ facets as sidewalls (figure 2d).

For the calculation of the corresponding LTVGR values the cross-sectional shape has to be taken into account. Then values of 0.01 for low process temperature and values of 1.02 for high process temperatures combined with low pressure were obtained.

Another important point is the dependence of the growth rate on the surrounding masked area, i.e. in the case of stripe masks on the width of the SiO_2 stripes. To study this effect, our ELOG mask has an array of SiO_2 stripes varying in width from 20 μm to

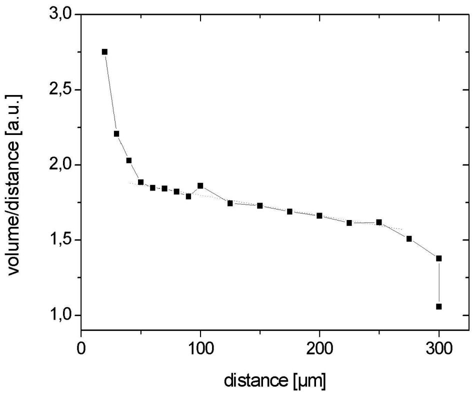

Fig. 3: Grown material per wafer area.

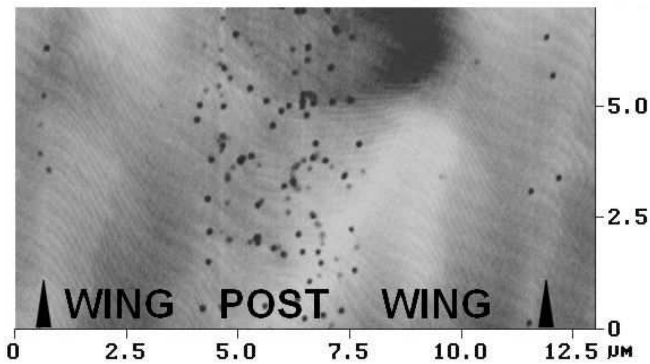

Fig. 4: Distribution of dislocations on a coalesced ELOG sample.

300 μm separated by 8 μm wide mask openings. Within this array the height of the grown structures changed from 5.2 μm for small distances of the mask openings to 22.2 μm for large distances. For better understanding of this effect, the deposited crystal volumes per wafer area are plotted versus the width of the stripes in figure 3. Except for the borders, where growth is possibly affected by the surrounding mask structure, this value shows only a slight change. So for mask design it has to be taken into consideration that in first approximation the deposited material per wafer area can be regarded as constant.

4.1 Coalesced low-dislocation ELOG wafer

Based on the results of the experiments described above, a new mask was designed with 8 μm wide SiO_2 stripes and 3 μm stripe distance. Optimized process parameters allowed the growth of completely coalesced 2 inch wafers. Dislocation analysis by etching with HCl showed dislocation densities of $3.5 \times 10^8 \mathrm{cm}^{-2}$ in the post region and $1.2 \times 10^7 \mathrm{cm}^{-2}$ in the wing region. The distribution of the dislocations over the different areas is shown in figure 4. The coalescence line is indicated by arrows.

References

[1] J. Speck and S. Rosner, "The role of threading dislocations in the physical properties of GaN and its alloys," *Physica B*, vol. 273–274, pp. 24–32, 1999.

[2] B. Beaumont, P. Vennegues, and P. Gibart, "Epitaxial Lateral Overgrowth of GaN," *phys. stat. sol. (b)*, vol. 227, no. 1, pp. 1–43, 2001.

[3] J. Park, P. Grudowski, C. Eiting, and R. Dupuis, "Selective-area and lateral epitaxial overgrowth of III-N materials by metal organic chamical vapor deposition," *Appl. Phys. Lett.*, vol. 73, no. 3, pp. 333–335, 1998.

Homogeneity in MOCVD-Processes

Matthias Seyboth

Various kinds of growth homogeneity in MOCVD systems are important for production and research. This paper comments on run-to-run-homogeneity and on on-wafer-homogeniety in an AIXTRON 200/4 RFS single wafer reactor for gallium nitride epitaxy. Typical single layer results as well as device properties and problems are discussed.

1. Introduction

Homogeneity of layers is an essential feature for deposition systems in semiconductor technology. In production lines devices have to fullfill narrow specifications. Thus the starting point – for light emitting diode manufacturing the epitaxial wafers – has also to comply with certain specifications. Especially for production systems a distinction is drawn between different kinds of homogeneity:

- On-wafer-homogeneity – variation of sheet or device parameters on one single wafer.
- Wafer-to-wafer-homogeneity – variations between several wafers in one run of a multi wafer system.
- Run-to-run-homogeneity or reproducibility – changes occuring in consecutive runs.

Whereas wafer-to-wafer variations hampering production yield are a serious problem for device manufacturing the other types also constitute a difficulty for research facilities.

1.1 Run-to-run-homogeneity

Contrary to production, in research a lot of intended changes to growth parameters and device structures are carried out. The typical aim is not the hundredfold reproduction of a device structure but to study effects of such changes. To make sure that variances in layers are results of these sometimes minor changes in the epitaxial process, a stable, reproducible process with only small variances has to be proven.

In addition to epitaxy optimization it is sometimes necessary to increase the provided wafer area beyond one wafer for processing tests – comparable to production. Only reproducible wafers allow for meaningful tests of contact metals, annealing procedures or device structuring.

There are several quite different reasons causing reproducibility problems in our AIXTRON 200/4 RFS single wafer MOCVD system. Drifts in mass flow and pressure controllers are rather small and are of no major concern. In our epitaxial system depositions and the gas foil rotation are major reasons for changes from growth run to growth run, especially in combination with the temperature measurement setup. The growth temperature in our system is measured at the bottom of the rotation disk by a pyrometer. The wafer surface temperature, decisive for growth, is determined by radiation transfer of the rotation disk and by direct induction heating of the satellite. Depositions on liner walls change the radiation distribution. These depositions increase from run to run. The gas foil rotation has to be adjusted to achieve a steady rotation of the satellite. The gas injected between rotation disk and satellite moves the satellite in the field of the rf-heater and has also inherent cooling effects. To counteract these effects the real surface temperature had to be used as control parameter [1].

There are also external reasons deteriorating reproducibility: e.g. changes to source materials as increasing impurities in ammonia with emptying of bottles and especially variations of sapphire quality. The "epiready" sapphire polishing sets the starting surface for the growth, here already slightly damaged surfaces can worsen the growth. Another problem can be bowing of the sapphire substrate, the heat transfer from susceptor to surface and thus the temperature gets irreproducible.

1.2 On-wafer-homogeneity

On-wafer-homogeneity concerns also both epitaxy and device research but with a stronger focus on the latter one. For epitaxy optimization it is favorable to have a sufficient big homogeneous wafer part for characterization purposes and as area to be improved. This can prevent the problem that e.g. the inner and the outer part of a wafer change in different directions from run to run.

Even more important is on-wafer-homogeneity for device research and development as well as for processing tests. As already mentioned, test series with different technological treatments require certain minimum amounts of wafer area. Characterization efforts like absorption measurements such as described in [2] need up to 1/4 2"-wafer for certain test structures. Devices like detectors and power field effect transistor structures can demand wafer areas in the cm^2 size.

The principal idea to receive homogneous epitaxial layers in a horizontal reactor MOCVD system is to rotate the wafer in the depleting gas phase. In conventional systems the hot satellite rotates in a hot susceptor. In our system only the satellite part is heated, thus reducing parasitic gas phase reactions. But by this design the depletion starts only in the proximity of the wafer causing a certain thickness profile. Beyond that there are effects caused by the abrupt temperature change at the satellite edge.

2. Experimental results

2.1 Run-to-run-homogeneity

After a first, light deposition on the liner, stable growth is possible for 10 to 20 growth runs. Figure 1 depicts reflectometer data of 11 consecutive growth runs, indicating a very reproducible growth. Both growth rate and reflection behavior show almost no changes over the series.
With increasing thickness the deposition especially on the liner ceiling changes the flow pattern within the liner tube. This leads to a reduction of the growth rate as shown in graph 2.

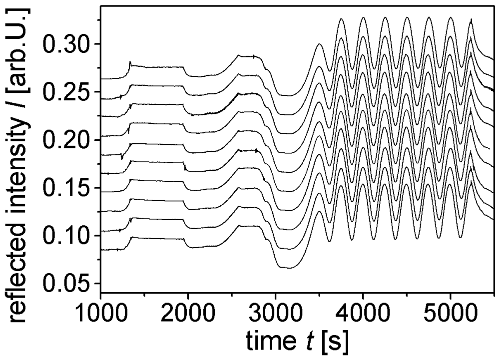

Fig. 1: Reflectometry data of 11 growth runs show reproducible growth. Constant oscillation periods reveal unaltered growth rate.

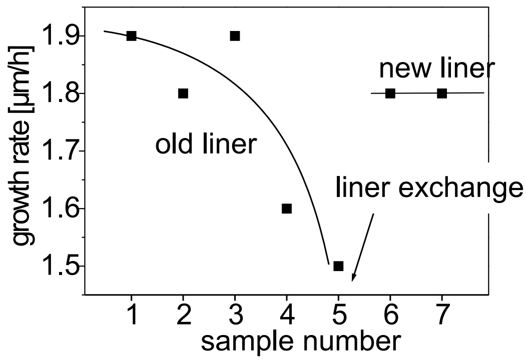

Fig. 2: Decreasing growth rate, determined from reflectometer oscillations, with increasing liner deposition after strong deposition makes liner change necessary.

Figure 3 demonstrates homogeneous n-doping over four growth runs. The standard deviation of 2 at a mean value of 139 $1/\Omega\text{cm}$ is within the range of the measurement uncertainty of the Hall setup.

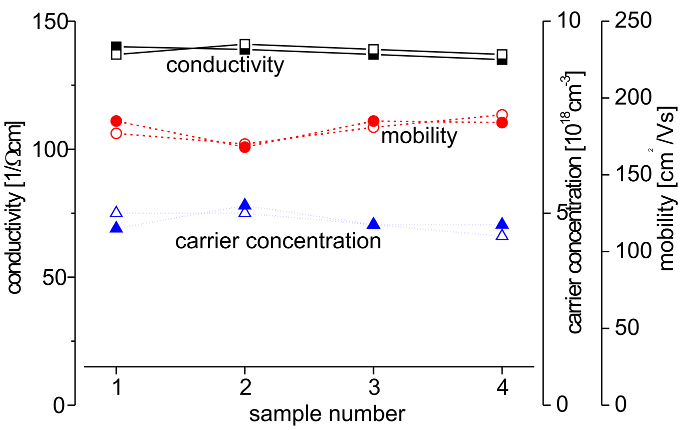

Fig. 3: Conductivity, carrier concentration and mobility of four n-doped, nominally equal samples. For the Hall measurements two pieces of each wafer are measured.

2.2 On-wafer-homogeneity

In device wafers different homogeneities of different layers can combine to a complex pattern. Epitaxially caused it shows due to the rotation a radial symmetry.

Optimized single layer structures, where different reasons for inhomogeneities could be coped with, enabled an improvement for complete device wafers. Figure 4 shows homogeneity analysis of a wafer before and after improvement. Device data for LEDs measured from wafer center to edge are depicted. Besides optimization of the doping profiles, particularly an optimum thickness of the quantum well region improved device homogeneity.

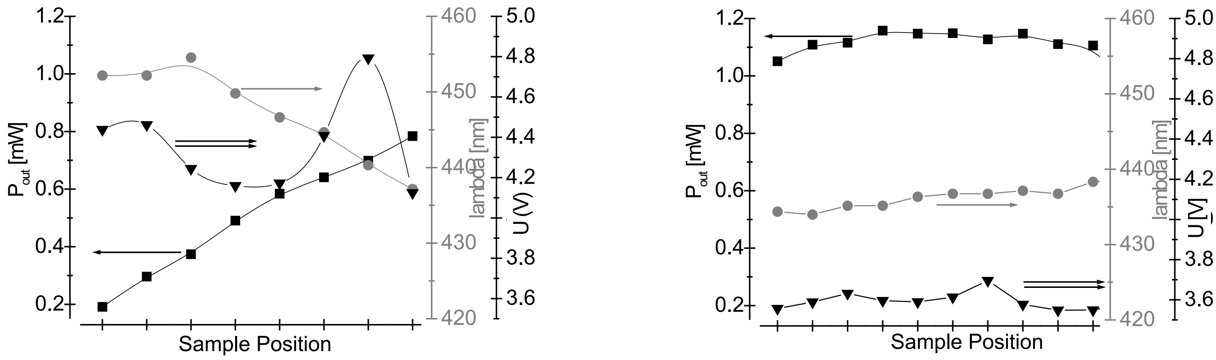

Fig. 4: Homogeneity data of two LED wafers. Displayed are emission wavelength, optical output power and voltage at a current of 20 mA. The results of the significantly more homogeneous wafer in the right picture were possible by optimization of the single layers.

3. Conclusion

Reasons for growth inhomogeneities have been allocated. Adapted process management has reduced and partly prevented them. Thereby sufficient homogeneous and reproducible growth has been established, thus allowing advanced characterization methods as well as efficient device and epitaxy optimization.

References

[1] R. Schmidt, H. Hartdegen, N. Nastase, R. Steins, and T. Zettler, "Über die Bestimmung der Wachstumstemperatur beim MOVPE-Wachstum von GaN auf Saphir," *17. Workshop Epitaxie von III/V-Halbleitern, DGKK 2002*, Magdeburg, Germany, Dec. 2002.

[2] S. Schad, B. Neubert, M. Seyboth, F. Habel, C. Eichler, M. Scherer, P. Unger, W. Schmid, C. Karnutsch, and K. Streubel, "Absorption of guided modes in light emitting diodes," in *Light-Emitting Diodes: Research, Manufacturing, and Applications,* F. Schubert, SPIE Proc. 4996 , San Jose, CA, USA, Jan 2003, accepted.

Low Resistance and Thermally Stable Contacts to n-type GaN using Ti/Al/Ni/Au

Marcus Scherer

The Ti/Al/Ni/Au metalization scheme is demonstrated as a suitable solution for low resistive and thermally stable contacts to n-type GaN. In this study the influence of the Ti-layer thickness as well as the impact of thermal treatment on the contact behavior is investigated. As an important number for ohmic contacts, the specific contact resistance is determined. To prove the thermal stability of this scheme, Auger electron spectroscopy has been performed before and after annealing.

1. Introduction

With increasing demand for high-power, high-efficiency GaN-based light-emitting diodes (LEDs) for lighting applications [1], also the requirements for contacts as one of the key components of optoelectronic devices became more and more stringent. Although Ti/Al-contacts have been proven as low resistive on n-type GaN [2], these contacts suffer from their insufficient thermal stability at annealing temperatures of more than 600°C due to the low melting point of aluminum [3]. During a complete processing sequence of a GaN-based LED, this temperature range is reached to obtain good contact and therefore device characteristics. In this paper we combine the Ti/Al-contact layers with a thermally more stable Ni/Au-cap to achieve low resistive and thermally stable contacts on n-GaN.

2. Experimental Setup

The III-V nitride films used in this study were grown in a horizontal MOVPE reactor on c-plane sapphire substrates. First, a 1.1 μm thick undoped GaN buffer was grown, followed by a 1.2 μm Si-doped GaN layer. A free carrier concentration of n = $4.7{\cdot}10^{18}\,\mathrm{cm}^{-3}$ (μ_n = $180\,\mathrm{cm}^2/\mathrm{Vs}$) was determined from Hall measurements. The contacts were characterized using a HP4145B Semiconductor Parameter Analyzer and the specific contact resistances (ρ_c) were determined by the transfer length method (TLM).

The mesa region for the TLM structures was fabricated by chemically-assisted ion-beam etching (CAIBE) using Cl_2. The metal contacts were deposited by electron beam evaporation and patterned by lift-off technique. The interspacings between the contact pads vary from 10 to 320 μm. The metalization scheme consists of Ti, 120 nm Al, 20 nm Ni and 80 nm Au. To investigate the influence of the initial titanium layer, its thickness was varied from 5 to 20 nm. The contacts are annealed in a rapid thermal process at temperatures between 300 and 800°C in a nitrogen atmosphere for 10 s to 5 min. Furthermore, the contacts are examined by Auger electron spectroscopy (AES).

3. Results and Discussion

3.1 Electrical properties

Ti/Al/Ni/Au-contacts (20/120/20/80 nm) which are used for high-temperature stable GaN/AlGaN field-effect transistors [4] show Schottky-behavior in the as-deposited state (Fig. 1 left). A temperature of at least 600°C is necessary to achieve ohmic behavior. The best results could be obtained after a thermal treatment at 800°C for 30 s with a determined ρ_c of $8.5 \cdot 10^{-5}\,\Omega\text{cm}^2$ (Fig. 1 right).

Previous investigations on Ti/Al contacts indicate improved contact characteristics with decreasing Ti-thickness, so a sample with 5 nm Ti and unchanged top layers has been prepared. Although the Schottky-barrier of the as-deposited contacts is slightly lower in comparison to the contacts with 20 nm Ti, again a thermal treatment at 600°C is mandatory to change the contact behavior from rectifying to ohmic (Fig. 2 left). The lowest specific contact resistance of $3.6 \cdot 10^{-5}\,\Omega\text{cm}^2$ is achieved after annealing at 600°C for 2 min (Fig. 2 right). This value is comparable to results previously published by Papanicolaou et. al. [5]. The reduced temperature for optimum contact results with thinner Ti-layer might be useful in processing GaN/InGaN-LEDs when combining the annealing steps for n- and p-contacts, where temperatures are normally below 650°C [2].

3.2 Structural properties

The above shown results can also be achieved by using the more simple Ti/Al-metalization, but these contacts suffer from severe balling-up effects when treated at 600°C and more

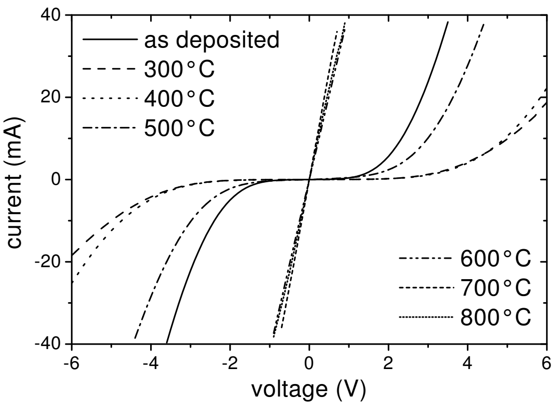

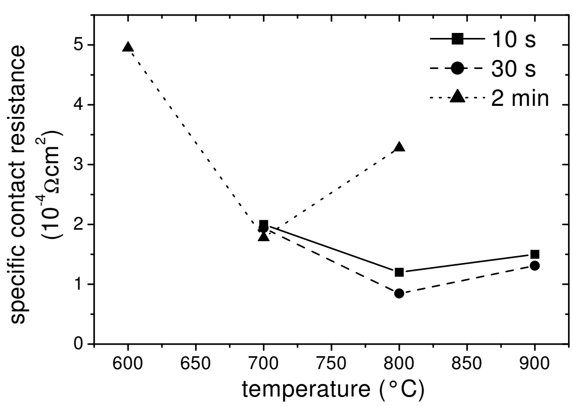

Fig. 1: IV-characteristics (left) and specific contact resistances (right) of Ti/Al/Ni/Au-contacts with 20 nm titanium.

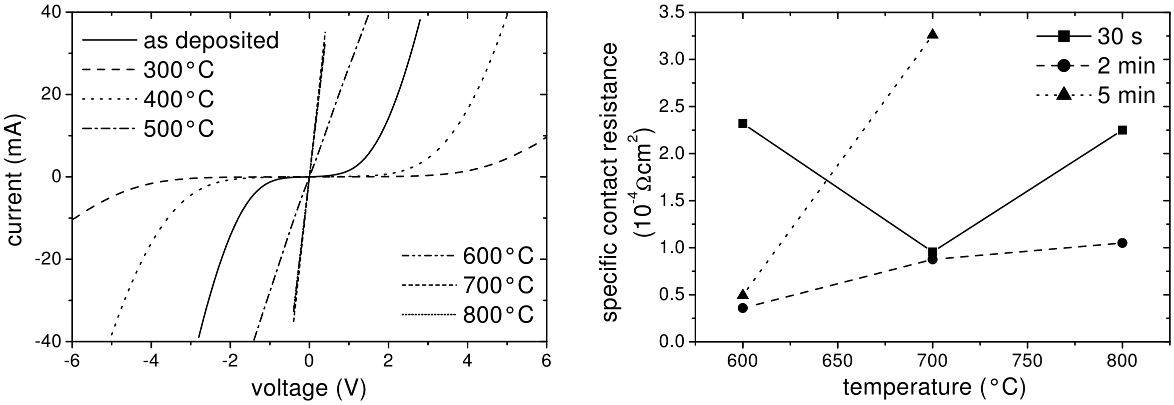

Fig. 2: IV-characteristics and specific contact resistances of Ti/Al/Ni/Au-contacts with a Ti-thickness of 5 nm.

due to the low melting point of aluminum (660°C [3]). The balling-up results in metal-islands which are not suitable for wire bonding. In contrary, the Ti/Al/Ni/Au contacts profit from the more stable Ni/Au cap and therefore the surface morphology is not tremendously changed when treated at temperatures up to 800°C (Fig. 3).

Figure 4 shows the AES depth profile of the contacts before and after thermal treatment. The metal layers are clearly separated after deposition, but after annealing at 600°C for 2 min complete intermixing can be observed. This result is in good agreement with previous microstructure investigations of this metal scheme [6, 7], where the same metal phases (e.g. NiAl, Al_2Au, Al_3Ti) have been found all through the contacts. Since an alloy is formed during annealing, the contacts should remain stable for longer periods than conventional metalization schemes, where intermixing of metals is still possible due to remaining separated layers.

4. Conclusion

In this study, we presented Ti/Al/Ni/Au as a suitable metalization scheme for low resistive and thermally stable contacts on n-type GaN. The best result of $\rho_c = 3.6 \cdot 10^{-5}\,\Omega\mathrm{cm}^2$ is obtained by using 5 nm Ti and annealing the sample at 600°C for 2 min. Since complete

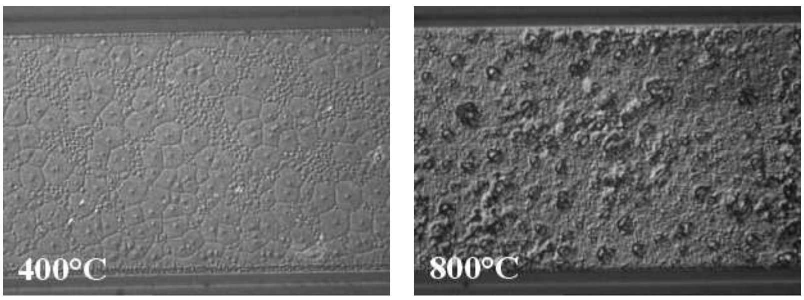

Fig. 3: Surface morphology of Ti/Al/Ni/Au-contacts (5/120/20/80 nm) after 2 min annealing.

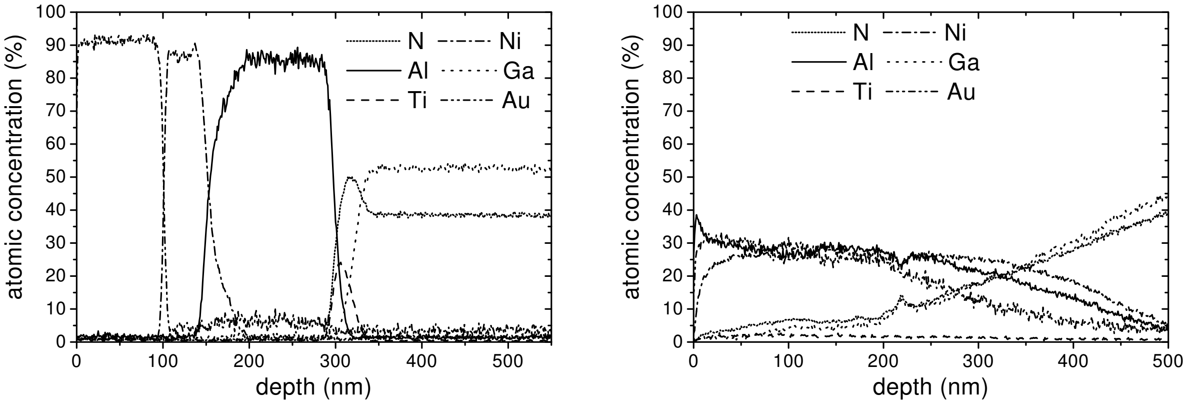

Fig. 4: AES depth profile of as deposited and annealed (600°C, 2 min) Ti/Al/Ni/Au-contacts (5/120/20/80 nm). Measured by D. Selvanathan, ECE Dept., University of Illinois at Urbana-Champaign, USA.

alloying is achieved after the thermal treatment, the scheme fulfills the demand of stable contacts.

References

[1] D.A. Steigerwald, J.C. Bhat, D. Collins, R.M. Fletcher, M.O. Holcomb, M.J. Ludowise, P.S. Martin, and S.L. Rudaz, "Illumination with solid state lighting technology," *IEEE J. Select. Topics Quantum Electron.*, vol. 8, no. 2, pp. 310–320, 2002.

[2] Q.Z. Liu and S.S. Lau, "A review of the metal-GaN contact technology," *Solid State Electron.*, vol. 42, no. 5, pp. 677–691, 1998.

[3] D.R. Lide, ed., *CRC Handbook of Chemistry and Physics*. 3rd electronic ed., 2000.

[4] I. Daumiller, *Herstellung und Charakterisierung von GaN-basierenden Heterostruktur-Feldeffekttransistoren*. PhD thesis, University of Ulm, 2002.

[5] N.A. Papanicolaou, M.V. Rao, J. Mittereder, and W.T. Anderson, "Reliable Ti/Al and Ti/Al/Ni/Au ohmic contacts to n-type GaN formed by vacuum annealing," *J. Vac. Sci. Technol. B*, vol. 19, no. 1, pp. 261–267, 2001.

[6] S. Ruvimov, Z. Lilienthal-Weber, J. Washburn, K.J. Duxstad, E.E. Haller, Z.-F. Fan, S.N. Mohammad, W. Kim, A.E. Botchkarev, and H. Morkoc, "Microstructure of Ti/Al and Ti/Al/Ni/Au ohmic contacts for n-GaN," *Appl. Phys. Lett.*, vol. 69, no. 11, pp. 1556–1558, 1996.

[7] A.N. Bright, P.J. Thomas, M. Weyland, D.M. Tricker, C.J. Humphreys, and R. Davies, "Correlation of contact resistance with microstructure for Au/Ni/Al/Ti/AlGaN/GaN ohmic contacts using transmission electron microscopy," *J. Appl. Phys.*, vol. 89, no. 6, pp. 3143–3150, 2001.

Time Resolved Study of GaN-Based Laser Diode Characteristics During Pulsed Operation

Christoph Eichler

Time dependent measurements of GaN-based laser diodes show a strong change in the emission wavelength and in the voltage drop during short pulses in the microsecond range. A temperature increase of approximately 50 K during a 3.7 μs pulse is obtained by different measurement methods and simulations.

1. Introduction

Especially for GaN-based lasers with high electrical power consumption due to high forward voltages and relatively high threshold currents, pulsed measurements are indispensable for characterization. These measurements give an estimation of the characteristics of the 'cold' laser diode without excess heating, and are frequently used for determination of the threshold current I_{th}, the characteristic temperature T_0 and the wavelength spectrum. However, for comparison of pulsed measurements with measurements in continuous wave (cw) operation, it is essential to understand the effects which take place during every single pulse of the measurement. Here, time resolved measurements of the electrical and optical laser characteristics are presented, which give a detailed insight in the dynamic behavior of laser diodes under pulsed operation.

2. Time Resolved Optical Spectrum

Using a common optical spectrum analyzer, all wavelengths occurring during the pulse are added up and appear as broad peaks in the spectrum. Wavelengths which are present in the spectrum for a short time yield small peaks, whereas wavelengths which are emitted for a longer period show up as larger peaks. Thus, the shape of the spectrum depends on the pulse width. To identify the real emission wavelengths together with their intensity, a setup for measuring the spectrum at each point in time during the pulse is used.

A typical time resolved spectrum measured with our setup is shown in figure 1. The laser diode was fabricated by OSRAM Opto Semiconductors and consists of SiC substrate, n/p-AlGaN cladding, n/p-GaN waveguide and three $In_{0.10}Ga_{0.9}N$/GaN multiple quantum wells with an $Al_{0.2}Ga_{0.8}N$ e-blocking layer. Contacts are deposited on a p-GaN contact layer on top of the 1.5 μm wide ridge and on the n-SiC backside [1]. The pulse width is 3.7 μs at a duty cycle of only 0.05 percent to avoid excess heating. The shown spectrum is

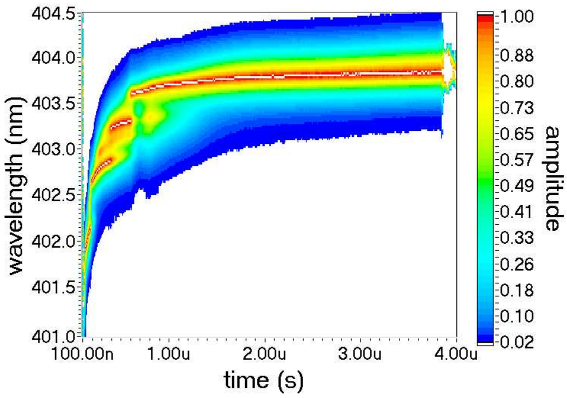

Fig. 1: Time resolved optical spectrum of a pulsed laser diode.

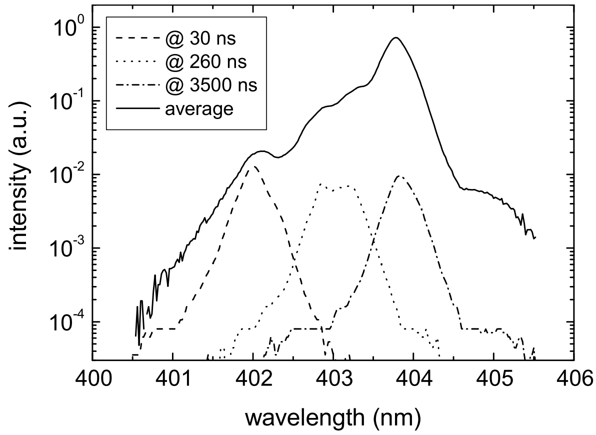

Fig. 2: Optical spectrum of a pulsed laser diode at different points in time during the pulse, compared with the average spectrum.

normalized to the maximum emission wavelength at each point in time in order to display the wavelength distribution irrespective of the slightly varying output power. Obviously, a strong change of the emission wavelength and the shape of the spectrum is observed during the pulse. As expected, the actual spectra during the pulse look completely different than the spectrum averaged over the complete pulse duration (figure 2).

A more detailed graph of the time dependent peak wavelength is shown in figure 3. Depending on the electrical pumping power, the spectrum shows a wavelength shift between 1.3 nm and 2.2 nm during the pulse. As time progresses, parts of the spectrum show a uniform slope, separated by sudden jumps. We attribute the parts with the uniform slope to a temperature induced shift of the longitudinal modes, which is superposed by

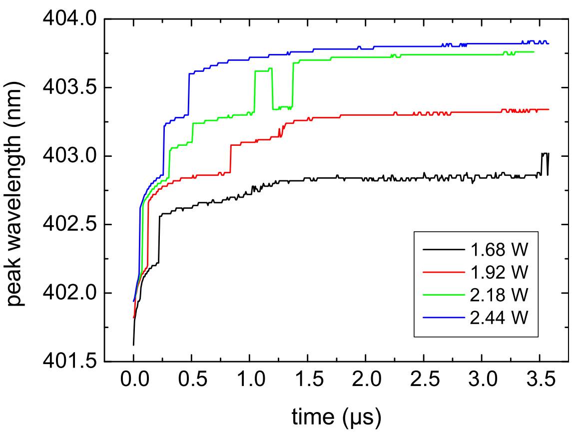

Fig. 3: Time dependent peak wavelength of a laser diode with 1.5 μm ridge width at various electrical input powers.

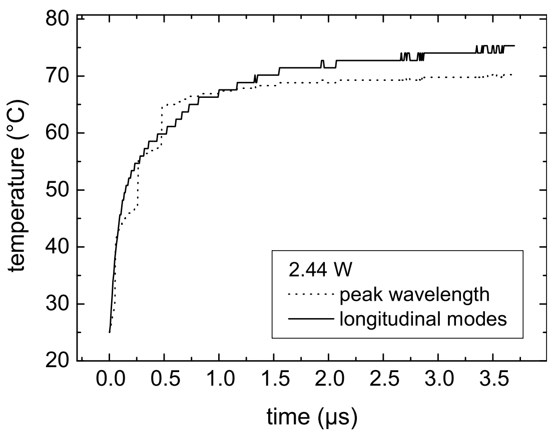

Fig. 4: Temperature increase calculated from shift of the gain spectrum and shift of the longitudinal modes.

the much stronger shift of the gain spectrum. At certain points this leads to a mode hop across several longitudinal mode spacings.

From temperature dependent measurements, a shift of the peak emission wavelength due to the shift of the gain spectrum of $d\lambda_g/dT = 0.042\,\text{nm/K}$ is obtained. Scaling the curve of the peak wavelength with this factor yields the temperature evolution, as shown by the dotted curve in figure 4.

Removing the discontinuities in the peak wavelength results in a smooth curve. This curve corresponds to the shift of the longitudinal modes, for which we calculated a factor of $d\lambda_{\text{FP}}/dT = 0.0155\,\text{nm/K}$ from the change in the effective refractive index [2, 3]. Scaling of the smooth curve with this factor leads to almost the same temperature increase, as can be seen in figure 4. Both methods show a temperature increase of approximately 50 K within 3.7 μs. Remarkably, most of the temperature change happens within only 1 μs.

3. Electrical Pulse

The increase in temperature was confirmed by measuring time dependent current-voltage characteristics. As time progresses, the laser heats up, which leads to a stronger activation of the Mg-dopant in the p-GaN layers [4]. Therefore the resistance of the device decreases during the pulse. This leads to a dynamic reduction of the voltage drop across the device, and a corresponding increase of current. Figure 5 shows the voltage drop across the laser

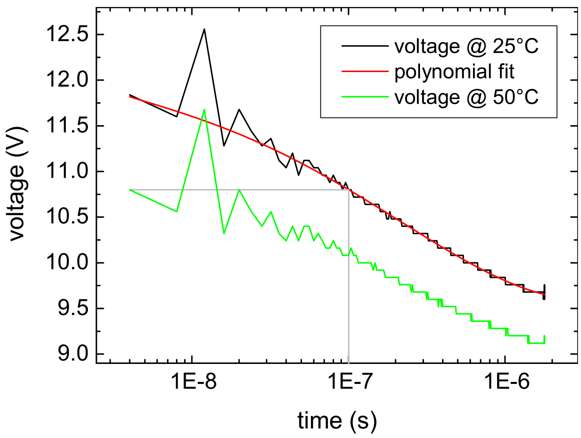

Fig. 5: Voltage drop across the laser diode versus time. By comparison of the voltage pulse at different temperatures, the temperature change can be obtained.

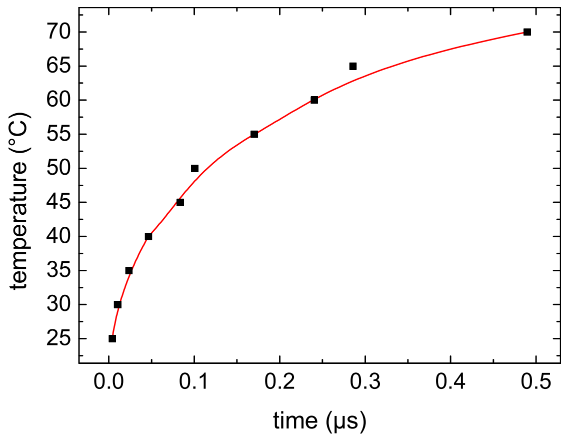

Fig. 6: Temperature increase during the pulse, extracted from voltage pulses at different temperatures.

diode during the pulse on a logarithmic time scale. For better accuracy, the curve is smoothed by a polynomial fit. Comparing the voltage at the beginning of the pulse at a certain temperature with the smoothed curve (25°C), as indicated by the horizontal line, one gets the time after which this temperature is reached. This is done for a set of temperatures in the range of 20°C to 70°C, and the result is shown in figure 6. In this case a temperature increase of 45 K within 0.5 μs is obtained, demonstrating that the fairly large series resistance of the p-region and the p-contact leads to a higher temperature in this part of the laser structure than in and near the active zone.

4. Simulation

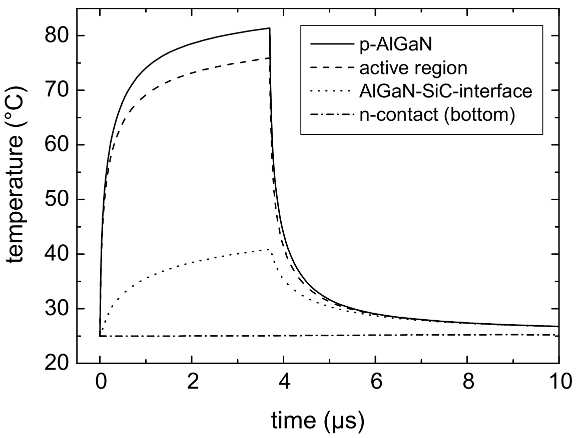

Fig. 7: Simulation of the temperature evolution at different points inside the laser diode, during and after a 3.7 μs pulse.

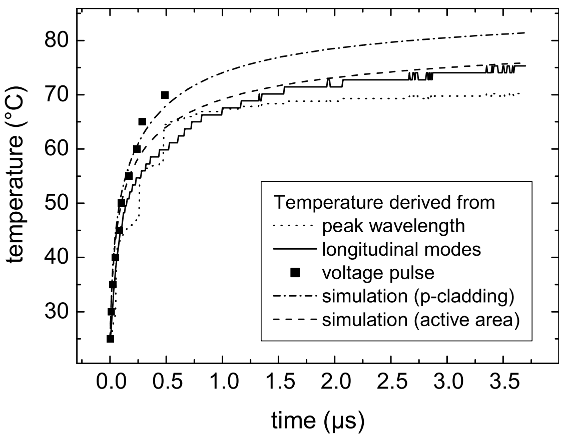

Fig. 8: Comparison of the different measured and simulated temperature evolutions.

Solving the time dependent heat equation by means of finite elements simulations (Flex-PDE) yields information about the temperature evolution during the pulse at different points inside the laser (figure 7). Excellent agreement to the experimental data could be achieved (figure 8): The simulated temperature increase in the p-AlGaN layer corresponds to the results measured with the voltage pulse method (section 3.), whereas the data calculated for the active region confirm the results evaluated from the wavelength shift (section 2.). Obviously, the temperature increase is confined to a small area below the ridge, as shown by the much smaller temperature change at the n-AlGaN-SiC interface. As expected for such short current pulses, almost no temperature change is noticeable at the n-contact at the backside of the substrate.

5. Conclusion

In summary, these experiments reveal a strong dynamic behavior of our GaN-based laser diodes in short current pulses resulting from the drastic ohmic heating due to the still poor electrical properties of these devices. Thus, the presented methods represent an important tool for the optimization of the devices towards an improved power budget.

References

[1] V. Kümmler, G. Brüderl, S. Bader, S. Miller, A. Weimar, A. Lell, V. Härle, U. Schwarz, N. Gmeinwieser, and W. Wegscheider, "Degradation Analysis of InGaN Laser Diodes," *phys. stat. sol. (a)*, vol. 194, no. 2, pp. 419–422, 2002.

[2] G. Laws, E. Larkins, I. Harrison, C. Molloy, and D. Somerford, "Improved refractive index formulas for the AlGaN and InGaN alloys," *J. Appl. Phys.*, vol. 89, no. 2, pp. 1108–1115, 2001.

[3] I. Vurgaftman and J. Meyer, "Band parameters for III-V compound semiconductors and their alloys," *J. Appl. Phys.*, vol. 89, no. 11, pp. 5815–5875, 2001.

[4] W. Goetz, N. Johnson, C. Chen, H. Liu, C. Kuo, and W. Imler, "Activation energies of Si donors in GaN," *Appl. Phys. Lett.*, vol. 68, no. 22, pp. 3144–3146, 1996.

Absorption of Guided Modes in Light-Emitting Diodes

Sven-Silvius Schad and Barbara Neubert

The absorption of lateral guided modes in light-emitting diodes is determined by the photocurrent measurement method. A theory for waveguide dispersion is presented and extended by ray-tracing simulations. Absorption coefficients of InGaN-on-sapphire and AlGaInP-based structures is evaluated by comparison with simulation curves. For nitride-based samples with emission wavelengths of 415 nm and 441 nm, an absorption of 7 cm^{-1} is obtained. It is found that scattering is present in the buffer layer and influences the lateral intensity distribution. The investigated AlGaInP-based sample exhibits an absorption of $\alpha = 30$ cm^{-1} at 650 nm emission wavelength.

1. Introduction

The development of high brightness light-emitting diodes (LEDs) has opened a variety of high power applications over the past years which were predominated by conventional lighting technologies such as traffic signals, automotive rear and front lights. Among epitaxy and device processing, light extraction approaches are investigated nowadays. The existence of total internal reflection and absorption of light are limiting both, output power and external quantum efficiency. Different extraction strategies were proposed and implemented.

Resonant Cavity (RC) LEDs change the internal radiation pattern by coupling to a resonator. This enhances the fraction of light which propagates perpendicular to the surface interface. Further improvements have been achieved by applying photonic crystals to extract the remaining guided modes [1]. Another successful approach is the surface-textured thin-film LED [2] . The enhancement of extraction is explained by scattering of the internally reflected light at the textured surface and by the change of the propagation angle of non-escaping photons. Together with a highly reflective mirror bottom surface, multiple scattering events are possible and significantly improve the extraction probability. Both, the Truncated Inverted Pyramid (TIP)[3, 4] and the tapered LED redirect the light by using geometrically shaped chips. The TIP-LED uses a structured thick window layer which serves as reflector. Most of the light is extracted through the top surface, the reflected part escapes through the sidewalls. The tapered LED extracts guided modes by redirection of extraction cones. The light is generated in the center of a circular symmetric device and guided to a tapered region. The angle of incidence is then reduced by the taper at each reflection and extraction of guided modes occur.

In several structures of such kind, a fraction of light is coupled into laterally leaky or guided modes. The propagation through an unpumped quantum well region causes absorption losses thus reducing the external quantum efficiency. For the optimization of light emitting devices it is important to identify and quantify the loss mechanisms. The external quantum efficiency η_{ext} can be written as a product of internal (η_{int}), injection (η_{inj}) and extraction (η_{extr}) efficiencies. The latter one is determined by geometry, absorption and redirection effects, whereas the internal efficiency accounts for the fraction of radiative and total recombination rate. η_{inj} describes the efficiency of carrier injection into the wells. The extraction efficiency can be rated by the value of external quantum efficiency when both, internal and injection efficiency can be assumed to unity. Another common method is the use of ray tracing to determine the influence of chip geometry which can improve the estimation accuracy. However, results strongly depend on absorption [5] and its uncertainties. Thus, a better knowledge about absorption coefficients is desirable.

Different approaches have been investigated to determine the absorption in LED structures. Absorption of GaN-based samples around the fundamental band edge have been investigated [6, 7, 8] by transmission measurement. However, when absorption is low, the layer thickness has to be increased to get a sufficiently large intensity decay. The different thermal expansion coefficients of sapphire and gallium nitride limit layer thickness which hinders a determination of low absorption. More sensitive measurements can be carried out using the photothermal deflection spectroscopy [9] (PDS), but using PDS alone, an absolute quantitative determination cannot be performed. Absorption of InGaN/GaN single quantum wells were presented [10] by adjusting the absorption coefficient to the values evaluated by transmission method. However, the comparably large number of layers in LED structures makes a direct evaluation of layer absorption with fair accuracy impossible. On the other hand, it is elaborate to prepare samples with which quantum well, free carrier absorption and Urbach tails can be determined. Regarding the estimation of extraction efficiency, a simplification of the layer structure may be done and thus, the knowledge of an average absorption of layer structure can satisfy simulation needs and thus avail an improved estimation accuracy of extraction efficiency.

2. Determination of Absorption

2.1 Photocurrent measurement method

In contrast to established measurement methods, the sample itself is used for excitation and detection. The emitter, waveguide, and detector is integrated on a standard light-emitting diode wafer. Using lithography and mesa etching, a waveguide ($100\,\mu$m width) and two rectangular LED structures ($20 \times 100\,\mu\mathrm{m}^2$) are fabricated. One LED serves as emitter, whereas the other as detector, driven at reverse bias. A set of waveguides with different lengths identically in arrangement (length 200-3000$\,\mu$m) is used to determine the photocurrent as a function of distance. Provided that the sample is sufficiently homogeneous regarding the emission wavelength and the output power of the emitters, the

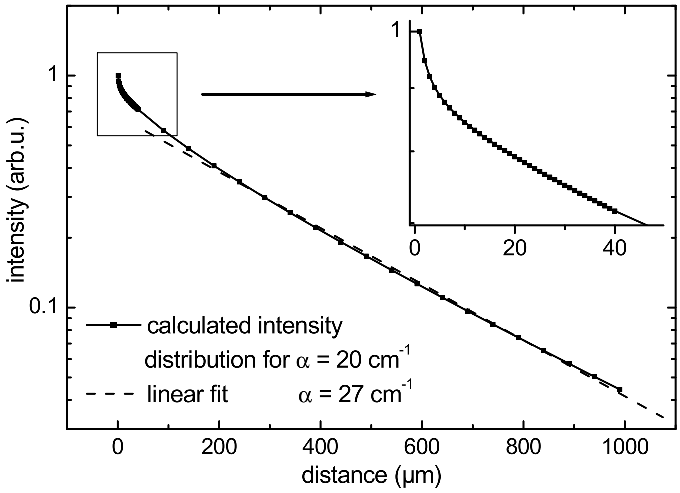

Fig. 1: Calculated intensity decay in a single layer film on a substrate layer without scattering. Curve for $\alpha = 20\,\text{cm}^{-1}$, refractive index of film $n_\text{f} = 2.5$ and substrate $n_\text{s} = 1.75$. The width of the film a is $100\,\mu$m, the height h is $2.5\,\mu$m. The waveguide dispersion increases the observed absorption, thus, a linear fit yields to $\alpha = 27\,\text{cm}^{-1}$.

intensity decay within the waveguide can be obtained. Thus, the method does not allow a spectrally resolved behavior. Also, a spectral weighting due to the sensitivity of the LED detector has to be accepted. Another etching step is employed to isolate the emitter, waveguide, and detector by a $4\,\mu$m wide groove and to uncover the buried side of the p–n-junction. The comparably large groove will introduce coupling losses between the emitter and the waveguide, however, because of the large lateral dimension, enough light remains to obtain a sufficient photocurrent. In turn, the waveguide is multi-mode and dispersion has to be considered. However, coupling light of a LED into a single mode waveguide is inefficient, so a multimode waveguide has to be used for this kind of experiment anyway. Lateral guiding is guaranteed by the index change of the semiconductor-air interface. In perpendicular direction the semiconductor-air and the GaN-sapphire interfaces cause sufficient reflections within GaN-based samples. To obtain a waveguide in AlGaInP-structures, a thick AlAs layer between AlGaInP and GaAs-substrate is used.

2.2 Theoretical considerations

In order to explain the observed intensity distribution, an analytical model is desirable. However, the complex layer structure of light emitting diodes impedes a practical description. Therefore, the basic effects are studied at a two layer model consisting of a waveguide on the top of a substrate, whereas for the evaluation of the absorption coefficient, a ray tracer is used.

Without scattering, the intensity distribution can be calculated by an analytically ray-based transfer function $f(\theta, \phi)$ between emitter and detector. An isotropic emission of a point source and also an isotropic absorption behavior of the detector LED is assumed. The calculation of subsequent incidence angles succeeds since only interfaces exist which are perpendicular to each other. Thus, it is possible to describe the whole propagation process in terms of the initial ray direction θ and ϕ. Choosing the x-axis as lateral direction and the y-axis as propagation direction the transfer function is [11]

$$\begin{aligned} f(\theta,\phi) &= (r_{z,1} r_{z,2})^{\mu_z} (r_x)^{2\mu_x} \exp\left(-\frac{\alpha y}{\sin\theta \sin\phi}\right) \quad , \qquad (1)\\ \mu_z &= \frac{y}{h \sin\phi \tan\theta} \quad , \\ \mu_x &= \frac{y}{a |\tan\phi|} \quad . \end{aligned}$$

$r_{z,1}(\theta)$ and $r_{z,2}(\theta)$ are the reflection coefficients at the waveguide-air and waveguide-substrate interface, respectively. $r_x(\theta, \phi)$ denotes the waveguide-air reflection coefficient in the lateral direction. It differs only in its incident angle from $r_{z,1}$. The width of the waveguide is a and the height is h. μ_z and μ_x are the numbers of reflections in z- and x-direction. α denotes the material absorption. Due to tilted propagation, the exponential decay is stronger than the pure material absorption α. Initially, no polarization is assumed, thus, 50% of the power is TE and TM, respectively. The TE polarized light with respect to the upper and lower interface is TM like on the sidewalls and vice versa. Therefore, no polarization mixing occurs allowing a separate calculation for the whole propagation. The photocurrent of the detector LED is obtained by integration of $f(\theta, \phi)$ and a sum of both, initially TE and TM-like.

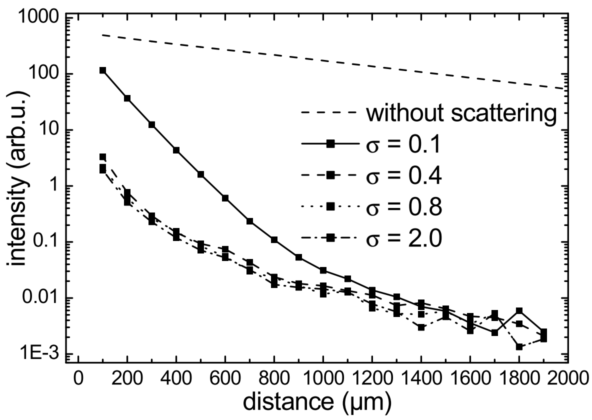

Fig. 2: Simulated intensity behavior with scattering using a Gaussian scattering distribution function. The varied width parameter σ has merely an influence ($\alpha = 7\,\text{cm}^{-1}$).

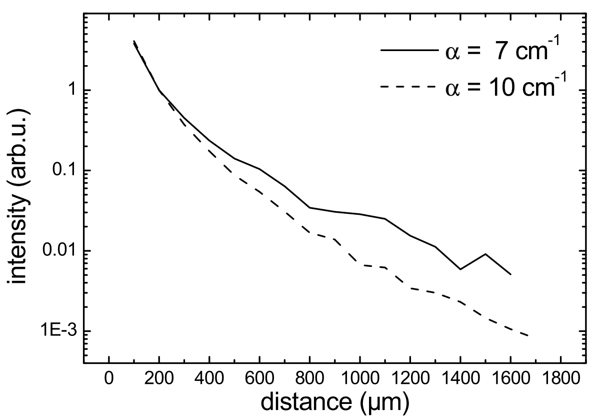

Fig. 3: Simulated intensity distribution for different absorption coefficients ($\sigma = 0.8$).

Exemplarily, we calculated the intensity distribution function for a nitride-based sample which is depicted in Fig. 1. Within the first 40 μm losses from leaky modes dominate the intensity decay. Then, the behavior is almost exponential. As expected, the observed intensity decay is larger than the material absorption caused by waveguide dispersion which is accounted by $\sin\theta \sin\phi$ in the exponential term in Eqn. 1. Between zero and 40 μm emission from leaky modes dominates the intensity decay. Summarizing the model, the presence of waveguide dispersion increases the intensity decay but the behavior is still exponential and the emission from leaky modes is on a comparable small scale.

Next, scattering is considered. In our model, the direction of reflected light is modified according to a scattering distribution function. Since this statistical approach requires a complete calculation of the propagation trajectory for each ray, a ray tracer has been employed. For the simulation, the same geometry is taken. Regarding the nitride samples grown on sapphire, two possible scattering regions exist, the buffer layer and, if unpolished, the substrate-side sapphire-air interface. However, we investigate in this work only the influence of the buffer layer (see below). Therefore, back reflections from the substrate-air interface are avoided in the simulation model by a strong absorbing layer. A Gaussian distribution function with width σ is applied at all surfaces of the waveguide. Although bulk scattering would represent the physical occurrence better, the exponentially increasing simulation effort caused by an additional layer forces a trade off. However, the expected differences are small.

Fig. 2 depicts the obtained intensity distribution. The presence of scattering causes a bowing of the intensity distribution curve with increasing σ. If σ is chosen between 0.4 and 2.0, the intensity behavior gets more and more independent of the absolute value of σ as can be seen from the simulation curves. In contrast, a strong dependence on the absorption coefficient remains as shown in Fig. 3.

3. Experimental

3.1 InGaN-sapphire based LED samples

The measurements are done using a HP4145 semiconductor parameter analyzer. I–V curves of the detector LED structures are shown in Fig. 4 with and without photocurrent. For large backward voltages, the devices exhibit a parallel resistance which is attributed to etching induced surface defects. However, between 1.7 V and -5 V, the current is dominated by the noise limit of voltage source. Switching on the light emitter by applying a current of 10 mA causes a significant increase in current of the detector LED. To get rid of the parasitic leakage current and the noise current, a subtraction of both curves is carried out. The result is illustrated in Fig. 5. However, for low currents and large reverse biases, an influence of leakage current remains. Furthermore, the photocurrent is a function of voltage, since a band alignment due to the quantum confined Stark effect occurs. Thus, the photocurrent as function of distance is evaluated by a cross section at $V = 0$.

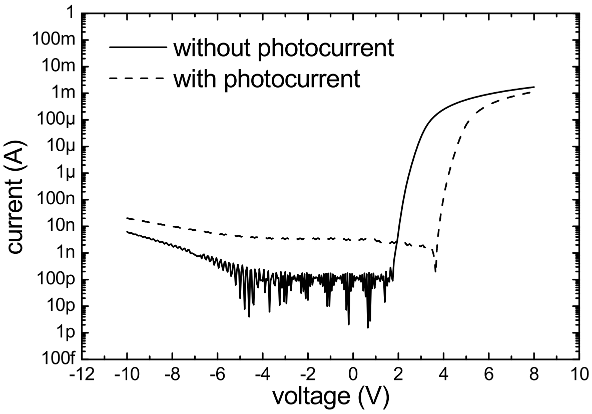

Fig. 4: I–V-curve of a detector LED with and without photocurrent.

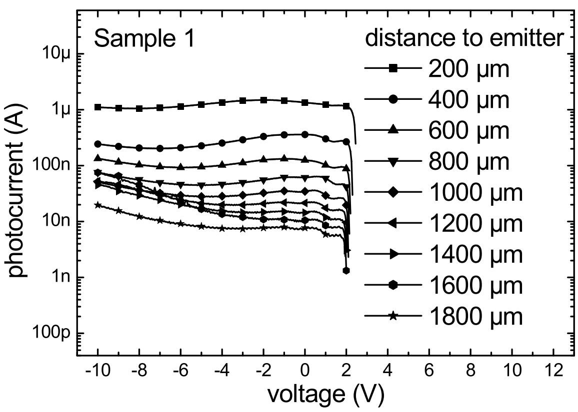

Fig. 5: Sample 1: Measured photocurrent in dependance of distance.

Two samples are investigated which have been grown using the same growth parameters. The simplified layer structure is as follows. On a 330 μm thick sapphire substrate a nucleation is performed and a buffer layer is grown. After that, a 1.5 μm thick silicon doped layer follows. The next layers build a fivefold multi-quantum well (MQW) structure followed by an AlGaN barrier consisting of approximately 10% aluminum. The top layer is magnesium doped gallium nitride. The emission wavelength was adjusted by the growth time, thus a shifting of the ground level of the wells is chosen instead of varying the indium content. The thickness of the complete epitaxial stack is 2.4 μm. Sample 1 exhibits an emission wavelength of 441 nm and FWHM of 20 nm, whereas the emission wavelength of Sample 2 is 415 nm with FWHM of 15.4 nm. Both devices show on wafer output powers larger than 1 mW at a current of 20 mA. The intensity behavior is depicted in Fig. 6. Best agreement with simulation is achieved by an absorption coefficient of $\alpha = 7\,\mathrm{cm}^{-1}$ and $\sigma = 0.8$ for both samples.

In Section 2.2 we did not preclude an influence of the rough substrate-air interface, this is taken up by means of a further experiment. If significant back reflection was present, an increase of substrate thickness would decrease the parasitic effect on the intensity distribution. Therefore, a 50 mm thick sapphire cylinder, 50 mm in diameter was put under the sample and to overcome the problem of interface roughness, diiodmethane was used as index matching fluid to achieve good optical coupling. The obtained intensity distribution is shown in Fig. 7 which only differs slightly from the measurement before. Thus, it is concluded that the substrate back reflection is not dominating the intensity curves.

3.2 AlGaInP based LED samples

The evaluation of photocurrent is accomplished in the same manner as for nitride samples. Fig. 8 depicts the photocurrent in dependance of voltage. The emitting LED structure was

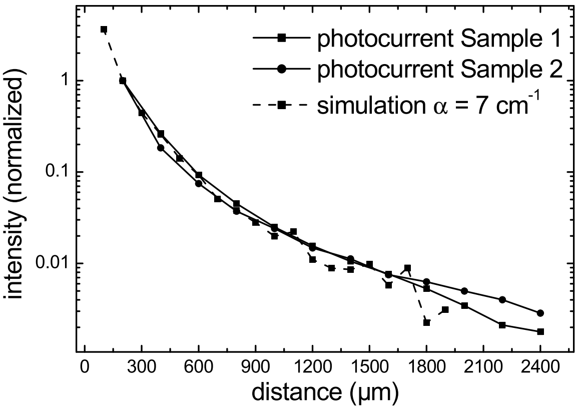

Fig. 6: Photocurrent as function of distance. Sample 1: InGaN-LED with emission wavelength of $\lambda = 441\,\mathrm{nm}$ and FWHM of 20 nm. Sample 2: InGaN-LED with emission wavelength of $\lambda = 415\,\mathrm{nm}$ and FWHM of 15.4 nm. Both samples show on wafer output powers exceeding 1 mW at $I = 20\,\mathrm{mA}$. The intensity distributions agree well with the simulation curve for $\alpha = 7\,\mathrm{cm}^{-1}$.

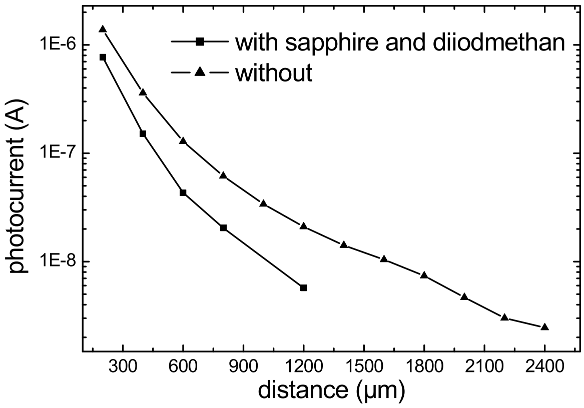

Fig. 7: Sample 2: If a significant fraction of detected light is caused by substrate back-reflection, it will be reduced by a larger propagation distance due to a decrease in solid angle (r^{-2}-law of propagation). However, the measurement carried out on a large sapphire cylinder ($I = 5\,\mathrm{mA}$) and without are alike ($I = 10\mathrm{mA}$). Thus, the intensity distribution is not affected by back reflection from the rough sapphire-air interface.

driven at a current of 5 mA. Compared with the nitride samples, no voltage dependance is observed. Fig. 9 shows the photocurrent as function of distance. In contrast to nitride samples, no significant scattering is present, therefore, the evaluation of absorption coefficient is done by an exponential fit which leads to $\alpha = 30\,\mathrm{cm}^{-1}$ disregarding waveguide dispersion. Still unclear is the influence of the spectral response of the detecting LED structure on the results. Therefore, the detector LED is replaced by a spectrometer. To maintain same coupling efficiency during the measurement, another waveguide was designed providing contacts on top with a distance of 250 μm. The waveguide was cleaved and the spectra of the emitted light through the facet have been measured. Regarding again Fig. 9, it is obvious that an evaluation of the absorption coefficient should be carried out for distances larger than 1000 μm, however, a measurement of spectra for LED structures in that region was not possible due to the small amount of emitted power.

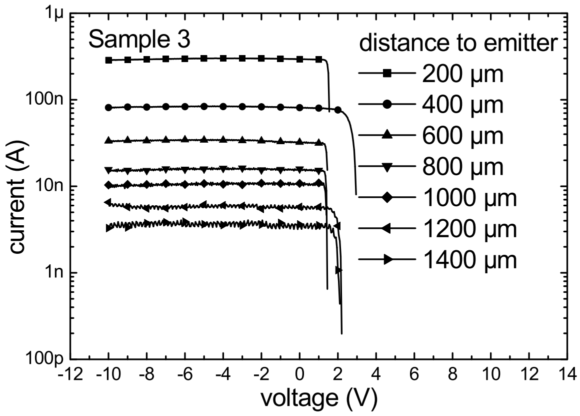

Fig. 8: Sample 3: Measured photocurrent in dependance of distance for the AlGaInP-based LED.

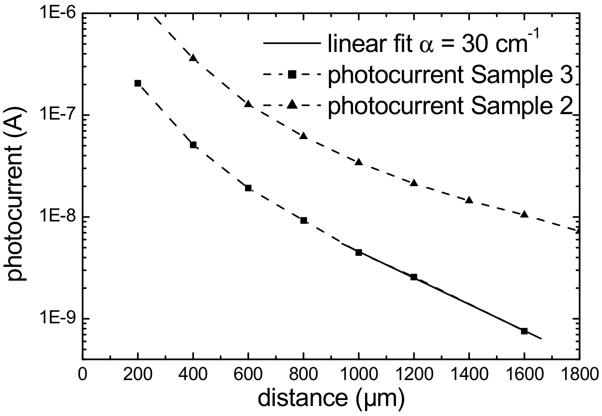

Fig. 9: Sample 3: AlGaInP-LED with emission wavelength of $\lambda = 650\,\mathrm{nm}$. Data is fit by an exponential law, $\alpha = 30\,\mathrm{cm}^{-1}$. It is found that absorption is much larger in the AlGaInP-based LED structure than in the nitride-based one (Sample 2, $\lambda = 415\,\mathrm{nm}$).

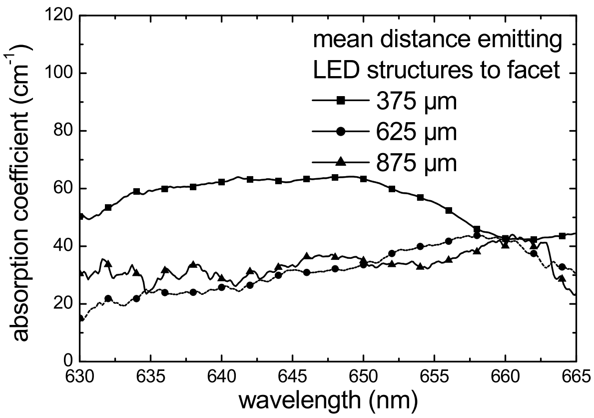

Fig. 10: Sample 3: Spectrally resolved absorption determined by subtraction of spectra of two adjacent LED structures as function of their mean distance to the facet.

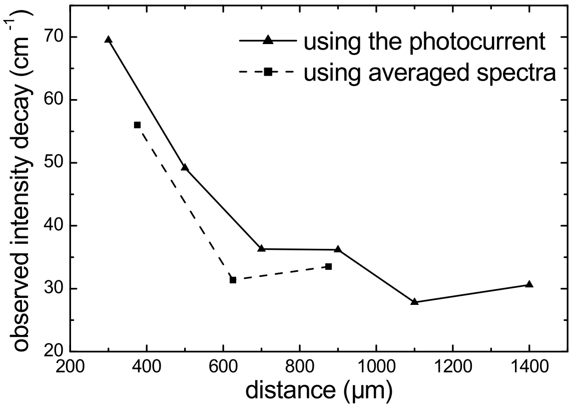

Fig. 11: Sample 3: Comparison of intensity decay using both, the photocurrent and averaged spectra.

The spectral absorption curves depicted in Fig. 10 are calculated by subtraction of two subsequent spectra at each case. Determined values are larger than the material absorption because of influence of waveguide dispersion. When employing a spectral averaging, a comparison with the photocurrent measurement is possible which is depicted in Fig. 11. Both measurement methods agree well with each other indicating that the spectral sensitivity of the detector LED structure plays a minor role.

4. Conclusion

We present a technique to determine the absorption of lateral guided modes in light emitting diodes. Absorption of InGaN-on-sapphire-based and AlGaInP-based structures is determined by comparison with ray tracing simulation curves. For the nitride samples, it is found that the lateral intensity distribution is governed by buffer scattering. A good agreement of measured photocurrent is found which enables a reliable determination of absorption. For both nitride samples with emission wavelengths of 415 nm and 441 nm, an absorption coefficient of 7 cm independent of the emission wavelength is determined. The investigated AlGaInP-based sample exhibits an absorption of $\alpha = 30\,\mathrm{cm}^{-1}$ at 650 nm emission wavelength which is significantly larger than the absorption in both nitride-based samples.

References

[1] M. Rattier, H. Benisty, R.P. Stanely, J.F. Carlin, R. Houdre, U. Oesterle, C.J.M. Smith, C. Weisbuch, and T.F. Krauss, "Towards Ultrahigh-Efficiency Aluminium Oxide Microcavity Light-Emitting Diodes: Guided Mode Extraction by Photonic Crystals," *IEEE J. Select. Topics Quantum Electron.*, vol. 8, no. 2, pp. 238–247, 2002.

[2] R. Windisch, C. Rooman, B. Dutta, A. Knoblauch, G. Borghs, G.H. Döhler, and P. Heremans, "Light-Extraction Mechanisms in High-Efficiency Surface-Textured Light-Emitting Diodes," *IEEE J. Select. Topics Quantum Electron.*, vol. 8, no. 2, pp. 248–254, 2002.

[3] M.O. Holcomb, M.R. Krames, G.E. Hofler, C. Carter-Coman, E. Chen, P. Grillot, K. Park, N.F. Gardner, J.-W. Huang, J. Posselt, D. Collins, S.A. Stockman, G.M. Craford, F.A. Kish, I-H. Tan, T.S. Tan, C.P. Kocot, and M. Hueschen, "High power Truncated-Inverted Pyramid $(\mathrm{Al_xGa_{1-x}})_{0.5}\mathrm{In_{0.5}P}$ Light-Emitting Diodes," *Proc. SPIE*, vol. 3938, pp. 77–81, 2000.

[4] F.A. Kish, F.M. Steranka, D.C. DeFevere, D.A. Vanderwater, K.G. Park, C.P. Kuo, T.D. Osentowski, M.J. Peanasky, J.G. Yu, R.M. Fletcher, D.A. Steigerwald, M.G. Craford, and V.M. Robbins, "Very high-efficiency semiconductor wafer-bonded

transparent-substrate $(Al_xGa_{1-x})_{0.5}In_{0.5}P/GaP$ light-emitting diodes," *Appl. Phys. Lett.*, vol. 64, no. 21, pp. 2839–2841, 1994.

[5] S.S. Schad, M. Scherer, M. Seyboth, and V. Schwegler, "Extraction efficiency of GaN based LEDs," *phys. stat. sol. (a)*, vol. 188, pp. 127–130, 2001.

[6] J.F. Muth, J.H. Lee, I.K. Shmagin, R.M. Kolbas, H.C. Casey, B.P. Keller, U.K. Mishra, and S.P. DenBaars, "Absorption coefficient, energy gap, exciton binding energy, and recombination lifetime of GaN obtained from transmission measurements," *Appl. Phys. Lett.*, vol. 71, no. 18, pp. 2572–2574, 1997.

[7] G. Yu, G. Wang, H. Ishikawa, M. Umeno, T. Soga, T. Egawa, J. Watanabe, and T. Jimbo, "Optical properties of wurzite structure GaN on sapphire around the fundamental absorption edge (0.78-4.77) eV by spectroscopic ellipsometry and the optical transmission method," *Appl. Phys. Lett.*, vol. 70, no. 24, pp. 3209–3211, 1997.

[8] G.Y. Zaho, H. Ishikawa, T. Egawa, T. Jimbo, and M. Umeno, "Optical Absorption and Photoluminescence Studies of n-type GaN," *Jap. J. Appl. Phys.*, vol. 38, no. 2, pp. 993–995, 1999.

[9] D. Brunner, H. Angerer, E. Bustarret, F. Freudenberg, R. Höpler, R. Dimitrov, O. Ambacher, and M. Stutzmann, "Optical constants of epitaxial AlGaN films and their Photoluminescence Studies of n-type GaN ," *Appl. Phys. Lett.*, vol. 82, no. 10, pp. 5090–5096, 1997.

[10] O. Ambacher, D. Brunner, R. Dimitrov, M. Stutzmann, A. Sohmer, and F. Scholz, "Absorption of InGaN Single Quantum Wells Determined by Photothermal Deflection Spectroscopy," *Jap. J. Appl. Phys.*, vol. 37, no. 1, pp. 745–752, 1998.

[11] S.S. Schad, B. Neubert, M. Seyboth, F. Habel, C. Eichler, M. Scherer, P. Unger, W. Schmid, C. Karnutsch, and K.P. Streubel, "Absorption of guided modes in light emitting diodes," in *Light-Emitting Diodes: Research, Manufacturing, and Applications,* F. Schubert, SPIE Proc. 4996 , Jan 2003.

Basics of Molecular Beam Epitaxy (MBE)

Fernando Rinaldi

A brief introduction to the MBE technique is presented with main attention to the elemental source MBE. A discussion on the effusion cell as beam source is shortly given starting from ideal cases to real cells homogeneity problems. A short review regarding the thermodynamic approach to the MBE is pointed out. Focusing on the possibility that, despite the fact that MBE processes occur under strong nonequilibrium conditions, for the III/V elements, a thermodynamic approach can be used on the basis of equations for mass action in combination with the equations describing the conservation of the mass of the interacting elements.

1. Introduction

Molecular beam epitaxy is a technique for epitaxial growth via the interaction of one or several molecular or atomic beams that occurs on a surface of a heated crystalline substrate. In Fig. 1 a scheme of a typical MBE system is shown. The solid sources materials are placed in evaporation cells to provide an angular distribution of atoms or molecules in a beam. The substrate is heated to the necessary temperature and, when needed, continuously rotated to improve the growth homogeneity.
According to Fig. 2, the molecular beam condition that the mean free path λ of the particles should be larger than the geometrical size of the chamber is easily fulfilled if the total pressure does not exceed 10^{-5} Torr. Also, the condition for growing a sufficiently clean epilayer must be satisfied, e.g. requiring for the monolayer deposition times of the beams t_b and the background residual vapor t_res the relation $t_\mathrm{res} < 10^{-5}\, t_\mathrm{b}$. For a typical gallium flux Γ of 10^{19} atoms $\mathrm{m^{-2}s^{-1}}$ and for a growth rate in the order of $1\,\mu$m/h, the conclusion is that $p_\mathrm{res} \leq 10^{-11}$ Torr. Considering that the sticking coefficient of gallium on GaAs atoms in normal operating conditions is approximately unity and that the sticking coefficient of most of the typical residual gas species is much less than 1, the condition above results to be not so strict, nevertheless ultra high vacuum (UHV) is required. Thus, UHV is the essential environment for MBE. Therefore, the rate of gas evolution from the materials in the chamber has to be as low as possible. So pyrolytic boron nitride (PBN) is chosen for the crucibles which gives low rate of gas evolution and chemical stability up to 1400° C, molybdenum and tantalum are widely used for the shutters, the heaters and other components, and only ultrapure materials are used as source. To reach UHV, a bakeout of the whole chamber at approximately 200° C for 24 h is required any

time after having vented the system for maintenance. A cryogenic screening around the substrate minimizes spurious fluxes of atoms and molecules from the walls of the chamber. Despite this big technological problems, MBE systems permit the control of composition

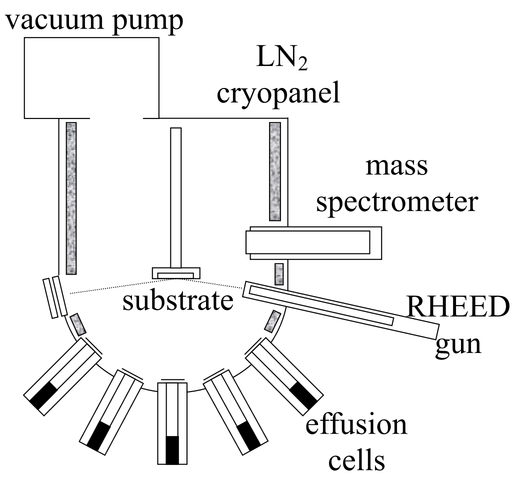

Fig. 1: A typical MBE system.

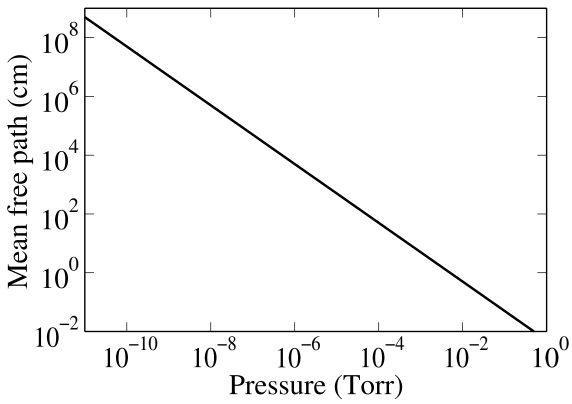

Fig. 2: Mean free path for nitrogen molecules at 300K.

and doping of the growing structure at monolayer level by changing the nature of the incoming beam just by opening and closing mechanical shutters. The operation time of a shutter of approximately 0.1 s is normally much shorter than the time needed to grow one monolayer (typically 1–5 s). Careful variation of the temperatures of the cells via PID controllers permits the control of the intensity of the flux of every component or dopant of better than 1 %. The UHV environment of the system is also ideal for many in-situ characterization tools, like the RHEED (reflection high energy electron diffraction). The oscillation of the RHEED signal exactly corresponds to the time needed to grow a monolayer and the diffraction pattern on the RHEED window gives direct indication over the state of the surface as can be seen in Fig. 3.

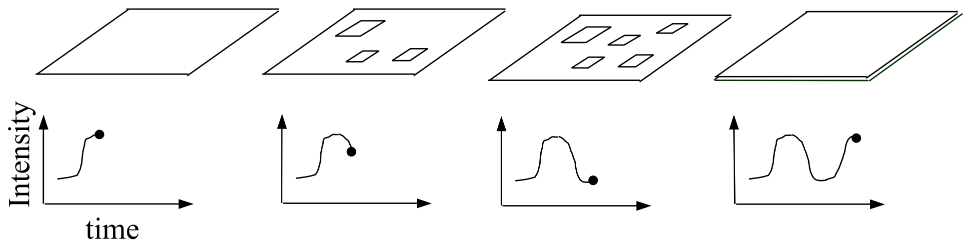

Fig. 3: RHEED oscillations.

2. Effusion Cells

The effusion cells used in MBE systems exploit the evaporation process of condensed materials as molecular flux source in vacuum. The understanding of the properties of real effusion cells is complicated and not straightforward, so easier models are needed and just the main complications are subsequently added.
In a closed enclosure, for pure substances, an equilibrium is estabilished between the gas and the condensed phase. Such systems have only one degree of freedom f, that means that the pressure p_{eq} is a function of the temperature T and can be approximately expressed by the Clapeyron equation [1]

$$p_{\mathrm{eq}}(T) = A \exp\left(-\frac{\Delta H}{k_{\mathrm{B}}T}\right). \tag{1}$$

Where in (1) ΔH is the evaporation enthalpy and k_{B} the Boltzmann constant. Under this equilibrium condition, we observe that when the p_{eq} is very low, it is possible to treat the incoming and the outcoming flux independently. A close look to the fluxes of particles having a mass m on the condensed phase surface shows that the maximum value for the evaporated flux Γ_{m} is

$$\Gamma_{\mathrm{m}} = \frac{p_{\mathrm{eq}}}{\sqrt{2\,\pi m\, k_{\mathrm{B}}T}}. \tag{2}$$

This assumes that each molecule from the gas phase is always trapped by the surface and an equal opposite flux of material must leave the condensed phase to maintain the equilibrium pressure. Considering now that the impinging beam is partially reflected and only a fraction a is accommodate on the surface, the complete expression for the flux leaving the surface can be easily found as

$$\Gamma = a\,\Gamma_{\mathrm{m}}. \tag{3}$$

The factor a is dependent on the microscopic status of the surface and is strongly unpredictable and because of (3) the flux of material. The Knudsen evaporating method overcome this problem providing a molecular beam that is independent of a. An ideal Knudsen cell is composed of a large enclosure were the condensed material is in thermodynamic equilibrium with the gas phase and of an orifice so small that the equilibrium pressure p_{eq} is not perturbed. The orifice geometry has to fulfill two additional conditions, one for the diameter d, that fullfils $d \ll \lambda$ at p_{eq} and one for its wall thickness L, assumed to be vanishingly thin. Under these conditions, the orifice is a surface with an evaporant pressure p_{eq} and has not the ability to reflect any of the incoming molecules resulting in $a = 1$ and the number of molecules per time unit of the created beam is $A\,\Gamma_{\mathrm{m}}$, where A is the orifice area.
The ideal Knudsen cell exhibits an angular distribution of the evaporated particles that follows a cosine law, where the angle θ is referred to the normal to A.

$$\frac{d\Gamma_\theta}{d\Omega} = \frac{\Gamma_{\mathrm{m}}}{\pi}\cos\theta, \tag{4}$$

so that the flux at distances much bigger than the orifice dimensions is proportional to $\cos\theta$. Using Clausing's model [2] for the conductance of a molecular flow in a cylindrical tube, Dayton has studied the deviation from ideality given when L/d is not longer 0. In this calculations a model is necessary to describe the interaction of the molecules with the orifice walls. Random reflection is the simplest approach, but also more complicated ones are possible involving also temporary adsorption and surface diffusion [3]. However, an estimation of a for the surface of the condensed material is not required. When L/d increases, the beam is more focused on the normal direction and for $L/d = 1$ the deviation from the cosine law is relevant. These models are important tools to measure p_{eq} and so thermodynamic quantities related with (1). When it is not possible to consider the enclosure as infinitely large and when it is therefore important to consider the influences of the main body of the cell, the value of the a coefficient is needed [4]. This is also the case of cylindrical and conical cells, that are widely used in MBE systems, there is no thermodynamic equilibrium between condensed and gas phase and therefore the value of a is necessary to calculate the emerging flux. Nevertheless, assuming for a a homogeneous distribution on the condensed phase material surface, it is possible to estimate the shape of the outcoming vapour beam using all the modelling discussed before. Many variables

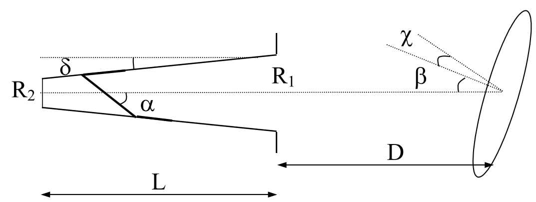

Fig. 4: Example of the geometrical configuration for a conical effusion cell.

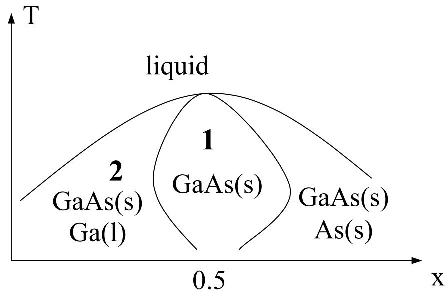

Fig. 5: Simplified phase diagram (T–x section) for GaAs. (s) is the solid and (l) is liquid phase. A gas phase is always present.

are involved in this problem, like shown in Fig. 4. For example, very often the source material is in liquid form (Ga, Al, In) and so an additional angle α is required to set up the geometry of the system. Some materials wet the crucible surface (e.g. aluminum in PBN crucibles), so other variables are needed to specify the position of the evaporating surface. A complex work of optimization is therefore necessary in relation to the fact that in a MBE system many cells must operate and for each one a suitable geometrical configuration cell substrate must be properly chosen. Control and homogeneity of the cells temperature are crucial, because of the strong dependence of the flux on temperature. W-Re thermocouples are used for the chemical stability at high temperatures and for the very low outgassing rate. Tantalum heater elements and radiative shields are chosen for the excellent refractory properties. These elements are often self-supporting preventing the use of material that does not have such low rate of gas evolution. Great care is also needed to decrease the temperature difference between heater and crucible. This is necessary to avoid very high temperature outgassing from tantalum, and to reduce the dissipated heat which causes possible uncontrolled outgassing from other parts of the vacuum chamber.

3. Thermodynamic Approach

In the past there was a lot of controversy concerning the possibility of applying thermodynamics to the growth processes in MBE. In the 1980s, MBE was developing experimentally very successfully, and most of the problems particularly regarding AlGaAs and InGaAlAs materials were solved empirically. In recent years, the need for MBE grow with newer materials revealed the importance of a closer theoretical modeling of the growth processes. In the case of MBE, it seems that the system cannot be described by a thermodynamic representation, because the different parts like sources, substrate, and walls are at different temperatures. However, it is possible to assume that the temperature of the system is the temperature of the substrate if the thermalization time is much shorter than the time required to grow a monolayer. So we consider an equilibrium state in which the partial pressures are the ones relative to fluxes of atoms or molecules leaving the substrates surface at its temperature.
The validity of this assumption is confirmed by two facts. First that the fluxes of atoms or molecules leaving the substrate have its temperature irrespective of the temperature of fluxes arriving at the surface. Second, the nature of the arsenic molecules, e.g. in the GaAs system, leaving the substrate is independent of the nature of the arsenic molecules reaching the surface. In this case, we have to consider the following reaction with the associated mass action equation [5]

$$2\mathrm{As_2(g)} \rightleftharpoons \mathrm{As_4(g)} \quad \text{and} \quad p^2_{\mathrm{As_2}}\, p^{-1}_{\mathrm{As_4}} = 3.98 \cdot 10^8 \exp\left(-\frac{2.35}{k_\mathrm{B}T}\right), \tag{5}$$

where the pressures are measured in atmospheres and $k_\mathrm{B}T$ in eV. The dimeric fraction of arsenic molecules leaving the substrate exactly follows the temperature behaviour predicted by (5) [6]. Starting by these assumptions it is possible to model the basic behavior of the III/V binary compounds in MBE conditions. For a binary compound, a phase diagram like the one sketched in Fig. 5 must be considered. In the region labeled with 1 GaAs(s) is present in equilibrium with Ga(g) and $\mathrm{As_2}$(g) and $\mathrm{As_4}$(g)(with just a small deviation, exaggerated in the figure, from the $\mathrm{Ga_{0.5}As_{0.5}}$ stoichiometry possible via point defect, but always much smaller than 10^{-4} even at high temperatures). Using the Gibbs' Phase Rule $f = c - p + 2$ [7] that relates the number of components c and the number of different phases p to the number of degrees of freedom f, it is easy to recognize that in the region 1 of the phase diagram $f = 2$. So temperature and pressure are independent. In the region 2, liquid gallium is present and therefore $f = 1$ as 3 phases are present. Hence a function $p = p(T)$ exists. In the region 1, the reactions between the components are

$$\mathrm{GaAs(s)} \rightleftharpoons \mathrm{Ga(g)} + \frac{1}{2}\mathrm{As_2(g)} \quad \text{and} \quad 2\mathrm{As_2(g)} \rightleftharpoons \mathrm{As_4(g)}. \tag{6}$$

The mass action equation is

$$p_{\mathrm{Ga}}\, p_{\mathrm{As_2}}^{\frac{1}{2}} = K_{\mathrm{GaAs}} = 2.73 \cdot 10^{11} \exp\left(-\frac{4.72}{k_{\mathrm{B}}T}\right). \tag{7}$$

Under normal MBE growth conditions, when $T > 450^\circ$ C, it is possible to neglect the $p_{\mathrm{As_4}}$ contribution to the total pressure. Therefore the total pressure is given by

$$p_{\mathrm{T}} = p_{\mathrm{Ga}} + p_{\mathrm{As_2}} = \frac{K_{\mathrm{GaAs}}}{p_{\mathrm{As_2}}^{\frac{1}{2}}} + p_{\mathrm{As_2}}. \tag{8}$$

The gallium pressure is maximum on the left side of the diagram, where it approximately corresponds to the gallium pressure on pure liquid gallium, moving to the right, because of (7), this partial pressure will decrease while the arsenic pressure is increasing. For some range in temperature, the pressure shows a minimum for a suitable stoichiometry of the solid phase. This is the condition that has to be applied to find the flux in free sublimation, i.e. sublimation in vacuum. The reason for the minimum condition is very general [8]. In a compound A_xB_{1-x}, the pressure is the sum of the pressures of its components. If the partial pressure of the component B is bigger than the one of the component A, the composition of the condensed phase will be enriched with A, moving the system to a lower partial pressure. If a minimum for a certain x exists, this will be asymptotically reached. In this point the sublimation is congruent. In our case the equation for a minimum of the pressure is

$$\frac{dp_{\mathrm{T}}}{dp_{\mathrm{As_2}}} = \frac{dp_{\mathrm{T}}}{dp_{\mathrm{Ga}}} = 0. \tag{9}$$

Solving this with the (8) will bring the result

$$p_{\mathrm{Ga}} = 2\, p_{\mathrm{As_2}} = (2\, K_{\mathrm{GaAs}}^2)^{\frac{1}{3}}. \tag{10}$$

This corresponds to congruent sublimation of GaAs. When the temperature increases over a certain temperature T_{max}, the pressure of the more volatile component, in this case arsenic, increases faster and there will be no minimum in the region 1. Under this condition, a liquid gallium phase is created. The temperature T_{max} is called "temperature of maximum sublimation". T_{max} is calculated imposing p_{Ga} from (10) equal to the value of the gallium pressure over the liquid gallium

$$p_{\mathrm{Ga}}^{\mathrm{L}} = 2.88 \cdot 10^5 \exp\left(-\frac{2.74}{k_{\mathrm{B}}T}\right). \tag{11}$$

The value of T_{max} is approximately 630° C. The free sublimation rate is so given by

$$v = -V\, \frac{p_{\mathrm{Ga}}}{\sqrt{2\,\pi m_{\mathrm{Ga}}\, k_{\mathrm{B}}T}}, \tag{12}$$

where p_{Ga} is defined by (9) and V is the volume occupied by a pair of gallium and arsenic atoms in GaAs. When an external As_2 flux is supplied, so that $p_{\mathrm{As_2}}^{\mathrm{ext}} \gg p_{\mathrm{As_2}}$, for the (7) we will obtain a reduced Ga evaporated flux

$$p_{\mathrm{Ga}}^{\mathrm{red}} = \frac{K_{\mathrm{GaAs}}}{(p_{\mathrm{As_2}}^{\mathrm{ext}})^{\frac{1}{2}}}. \tag{13}$$

Thereby a suppression of the sublimation occurs. The rate of evaporation inversely proportional to the square root of the arsenic flux to the substrate is experimentally observed in MBE systems. For an external As_4 flux in (13), $p_{As_2}^{ext}$ must be exchanged with $2\,p_{As_2}^{ext}$. It is important to emphasize that in the previous calculations we have used the fact that the sticking coefficient of gallium on GaAs is ≈ 1, because the outcoming flux, and so the related pressure, is always given by (3).
When an external gallium flux is added the growth rate can be expressed by

$$v = -V\,\frac{p_{\mathrm{Ga}} - p_{\mathrm{Ga}}^{\mathrm{ext}}}{\sqrt{2\,\pi m_{\mathrm{Ga}}\,k_{\mathrm{B}}T}}. \tag{14}$$

Just considering that the arsenic flux is always much bigger than the one of gallium, neglecting the fraction of arsenic that will take part in the growth process, and considering always the condition $p_{\mathrm{As}_2} \gg p_{\mathrm{As}_4}$, for the growth rate we get

$$v = C\left[p_{\mathrm{Ga}}^{\mathrm{ext}} - \frac{K_{\mathrm{GaAs}}}{(p_{\mathrm{As}_2}^{\mathrm{ext}})^{\frac{1}{2}}}\right]. \tag{15}$$

Also the temperature dependence implicit in (15) was experimentally found [9]. So for the typical $p_{\mathrm{As}_2}^{\mathrm{ext}}$ with a value of $10^{-6} - 10^{-4}$ Torr which is used, the growth rate is mainly controlled by the gallium flux. A solid arsenic phase is never formed in MBE system because the typical arsenic pressure would be for this temperature, $\mathrm{T} > 500^\circ\,\mathrm{C}$, in Torr range. The excess arsenic flux fixes a point in the phase diagram and so determines the type and concentration of point defects. This considerations are valid for many III/V compounds [10].

Compounds	$K_{\mathrm{III/V}}$	$T_{\max}(^\circ\,\mathrm{C})$
AlAs	$1.63 \cdot 10^{10} \exp\left(-\frac{5.39}{k_{\mathrm{B}}T}\right)$	902
GaAs	$2.73 \cdot 10^{11} \exp\left(-\frac{4.72}{k_{\mathrm{B}}T}\right)$	630
GaP	$2.26 \cdot 10^{11} \exp\left(-\frac{4.71}{k_{\mathrm{B}}T}\right)$	571
InAs	$7.76 \cdot 10^{11} \exp\left(-\frac{4.34}{k_{\mathrm{B}}T}\right)$	508
InP	$8.34 \cdot 10^{11} \exp\left(-\frac{4.02}{k_{\mathrm{B}}T}\right)$	268

For each compound equations like (11) can be used to calculate the $T_{\max}$. Extremely interesting is an overview on the ternary compounds. $\mathrm{Al}_x\mathrm{Ga}_{1-x}\mathrm{As}$, $\mathrm{Ga}_x\mathrm{In}_{1-x}\mathrm{As}$, $\mathrm{Al}_x\mathrm{In}_{1-x}\mathrm{As}$ were successfully analyzed. The problem in a ternal compound is the estimation of the activities coefficient γ that take the nonideal nature of the alloy into account. $\mathrm{Al}_x\mathrm{Ga}_{1-x}\mathrm{As}$ is a special case having $\gamma_{\mathrm{GaAs}} = \gamma_{\mathrm{AlAs}} = 1$. In other cases, e.g. $\mathrm{GaAs}_x\mathrm{P}_{1-x}$ we can write the following equations

$$p_{\mathrm{Ga}}\,p_{\mathrm{As}_2}^{\frac{1}{2}} = \gamma_{\mathrm{GaAs}}K_{\mathrm{GaAs}}x \quad \text{and} \quad p_{\mathrm{Ga}}\,p_{\mathrm{P}_2}^{\frac{1}{2}} = \gamma_{\mathrm{GaP}}K_{\mathrm{GaP}}(1-x) \tag{16}$$

together with the (5) and another mass action equation for the reaction $2P_{2(g)} \rightleftharpoons P_{4(g)}$. Considering that again the dimers are the dominating species, for T$>$ 500° C, and neglecting the amount of group-V elements that take part in the growth process we can find for the resulting final composition of $GaAs_xP_{1-x}$

$$x = \frac{1}{\left(\frac{\gamma_{\mathrm{GaP}} K_{\mathrm{GaP}}}{\gamma_{\mathrm{GaAs}} K_{\mathrm{GaAs}}}\right)\left(\frac{p^{\mathrm{ext}}_{\mathrm{P}_2}}{p^{\mathrm{ext}}_{\mathrm{As}_2}}\right)^{\frac{1}{2}} + 1} \tag{17}$$

Even neglecting the influence of the activity coefficients in (17), a good qualitative agreement can be found with the experimental data [11].

References

[1] R.A. Swalin, *Thermodynamics of solids.* New York: John Wiley & Sons, 1972.

[2] J.F. O'Hanlon, *A User's Guide to Vacuum Technology.* New York: John Wiley & Sons, 1989.

[3] W.L. Winterbottom and J.P. Hirth, "Diffusional contribution to the total flow from a Knudsen cell," *J. Chem. Phys.*, vol. 37, no. 4, pp. 784–793, 1962.

[4] K. Motzfeldt, "The thermal decomposition of sodium carbonate by the effusion method," *J. Phys. Chem.*, vol. 59, pp. 139–147, 1955.

[5] D.T.J. Hurle, "Revised calculation of point defect equilibria and non-stoichiometry in gallium arsenide," *J. Phys. Chem. Solids*, vol. 40, pp. 613–626, 1979.

[6] C.T. Foxon, J.A. Harvey, and B.A. Joyce, "The evaporation of GaAs under equilibrium and non-equilibrium condition using a modulated beam technique," *J. Phys. Chem. Solids*, vol. 34, no. 10, pp. 1693–1701, 1973.

[7] H.A.J. Oonk, *Phase Theory*, vol. 3. Amsterdam, Netherlands: Elsevier Scientific Publishing Company, 1981.

[8] F.A. Kröger, *The Chemistry of Imperfect Crystals*, vol. 1. Amsterdam, Netherlands: North Holland Publishing Company, 1973.

[9] J.M. van Hove and P.I. Cohen, "Mass action control of AlGaAs and GaAs growth in molecular beam epitaxy," *Appl. Phys. Lett.*, vol. 47, no. 7, pp. 726–728, 1985.

[10] P.S. Kop'ev and N.N. Ledentsov, "Molecular beam epitaxy of heterostructures made of III/V compounds," *Sov. Phys. Semicond.*, vol. 22, no. 10, pp. 1093–1101, 1988.

[11] S. Gonda and Y. Matsushima, "Molecular beam epitaxy of GaP and GaAsP," *Jap. J. Appl. Phys.*, vol. 15, no. 11, pp. 2093–2101, 1976.

Optical Coatings for Laser Facets Fabricated by Reactive Ion-Beam Sputter Deposition

Steffen Lorch

Reactive ion-beam sputter deposition is the preferred method to fabricate stoichiometric and dense layers for optical coatings with very low optical absorption. The refractive indices and thicknesses of such single- or multilayers can be optimized to get the required reflectivities for antireflection/high-reflection coatings on laser facets or antireflection coatings lower than 10^{-4} for laser amplifiers. Lasers can be coated after cleaving or on-wafer coating can be done on dry-etched laser facets. These AR/HR coatings can be characterized by using the threshold shift method or from the ratio of the emitted light of both facets.

1. Introduction

Optical coatings are used for adjustment of facet reflectivity R and for passivation of semiconductor lasers. For conventional semiconductor lasers, an antireflection/high-reflection coating (AR/HR with e. g. $R = 10\,\%/90\,\%$) is used. However, for laser amplifiers, antireflection (AR) coatings with very low reflectivity ($R \leq 10^{-4}$) are required. Due to the high intensity on the output facet, the coating becomes hot and can be destroyed by catastrophic optical mirror damage (COMD) processes. The power at which this occurs can be increased by using coatings with a low optical absorption. This can be realized with very dense and stoichiometric oxide layers. The best method to fabricate such optical coatings is reactive ion-beam sputter (RIBS) deposition with an assisted ion beam. [1, 2] describes why such a deposition method is the preferred method for optical coatings.

2. Ion-Beam Sputter Deposition System

Laser facets have been coated with an ion-beam sputter (IBS) deposition system. Cleaved lasers can be loaded in a laser-bar holder and using two deposition steps, the AR and the HR coating are deposited. Also on-wafer coating is possible if the facets are dry etched with for example a CAIBE system.

2.1 Design of the coatings

Firstly, the refractive index of the deposited material must be known. For that a thick layer (about 1 μm) of the material is coated on a microscope slide. The reflection and transmission is measured over the wavelength. With a simulation program (Essential Macleod [3]) both the refractive index and extinction coefficient can be calculated from these values. The principle for this calculation is described in [4, 5]. With this simulation program the required thicknesses of the layers with the given refractive indices of the usable materials can be simulated for the desired reflectivities. Additionally, the deposition rates for the different materials must be known. For that a test layer is deposited onto a silicon substrate and the thickness can be measured with an ellipsometer. With the deposition rates and required layer thicknesses now known the coatings can be deposited.

2.2 The IBS deposition system

Fig. 1: The ion-beam sputter deposition system.

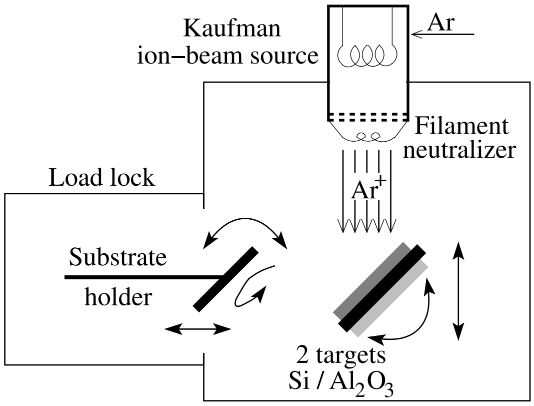

Fig. 2: Schematic diagram of the ion-beam sputter deposition system.

The ion-beam sputter deposition system used is shown in Fig. 1. The system has a load lock for a large throughput. The ion-beam is generated with a Kaufman ion-beam source (the functionality of such a source is described in [6]). The ion-beam current is an important parameter for the deposition and is constant during the deposition process. Two different targets can be used, Al_2O_3 and Si. The geometry in the process chamber can be changed; the distance between ion-beam source and target, the target angle, the distance between target and substrate, and the substrate angle. Additionally the substrate manipulator can rotate for an improved homogeneity. A schematic of the system is shown in Fig. 2.

2.3 AR/HR coating on cleaved lasers

The facets of a laser should have two different reflectivities [7]. The output facet should have an antireflection coating with a reflectivity of 5 % to 10 % and the rear facet a high-reflection coating with a reflectivity of 80 % to 95 %. In order to apply the coatings on the facets, the lasers are first cleaved and loaded in a laser bar holder. After mounting the holder on the substrate manipulator one side can be coated. After that, the holder must be turned and remounted to deposite the other facet.

In the case for such a AR/HR coating, the power of the outgoing light on the AR-coating side is much higher than the light going out at the HR-coating side. The ratio of these two output powers can be calculated using [8]

$$\frac{P_{\mathrm{AR}}}{P_{\mathrm{HR}}} = \frac{\sqrt{R_{\mathrm{HR}}}(1 - R_{\mathrm{AR}})}{\sqrt{R_{\mathrm{AR}}}(1 - R_{\mathrm{HR}})} \, . \tag{1}$$

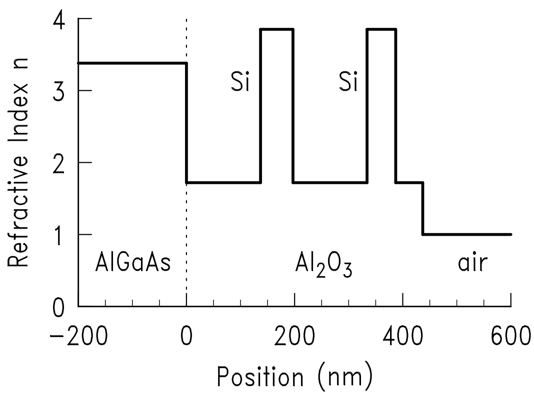

Fig. 3: Refractive index layout of a 5-layer high-reflection coating.

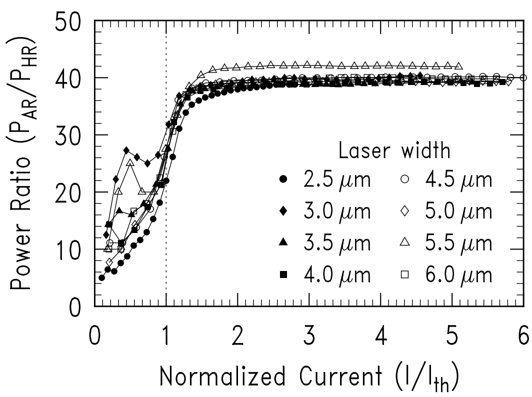

Fig. 4: Ratio of the output power of both facets over normalized current.

For an AR coating, a single layer of Al_2O_3 can be used. For the HR coating, five layers must be used. The refractive index layout for such a 5-layer coating is shown in Fig. 3. The characterization of the coating can be done by dividing the *L–I* curve of the AR-coating side by the *L–I* curve of the HR-coating side. In Fig. 4, this ratio is shown normalized to the threshold current for a laser with an AR/HR coating with 5 %/94 %. It can be seen, that above the threshold current the AR/HR ratio is constant at about 40. But according to Eqn. (1) for the given reflectivities the ratio should be higher at 72. The reason for that deviation is not yet known.

2.4 On-wafer coating

An other possibility for laser coating is the on-wafer deposition. If the facets are dry etched (e. g. with a CAIBE system), the facets can be coated directly on the wafer. In Fig. 5, the process for such an on-wafer coating is shown. In two steps the coatings are deposited on the facets. The advantage of the on-wafer coating is to eliminate the difficult loading of the lasers into a laser-bar holder. Additionally, the lasers need only be

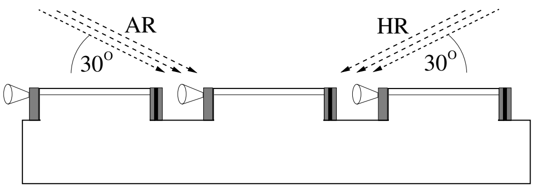

Fig. 5: AR/HR on-wafer coating of dry-etched laser facets.

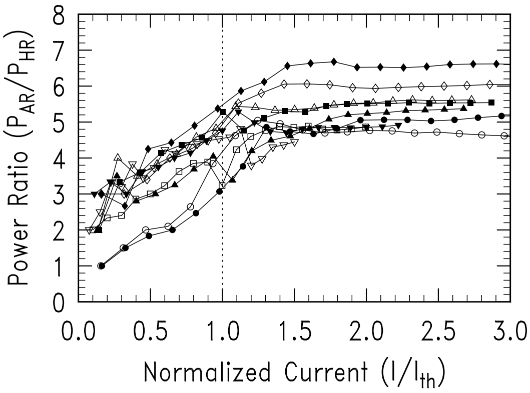

Fig. 6: Ratio of the output power of both facets over normalized current.

transferred into the chamber only once as the holder can be turned inside the chamber to achieve the correct placement for the second deposition. The disadvantage to such an approach is that in order to prevent deposition on the other facet the substrate holder cannot rotate during the deposition. After the deposition, the lasers can be separated by cleaving the substrate. Figure 6 shows the resulting characterization. AR/HR power ratios of 4.5–6.5 have been measured but the calculated ratio according to Eqn. (1) is 10.

3. Reactive Ion-Beam Sputter Deposition System

Presently, a new reactive ion-beam sputter deposition system is constructed and the first experiments have been completed.

3.1 The RIBS deposition system

Fig. 7: The chamber interior of the reactive ion-beam sputter deposition system.

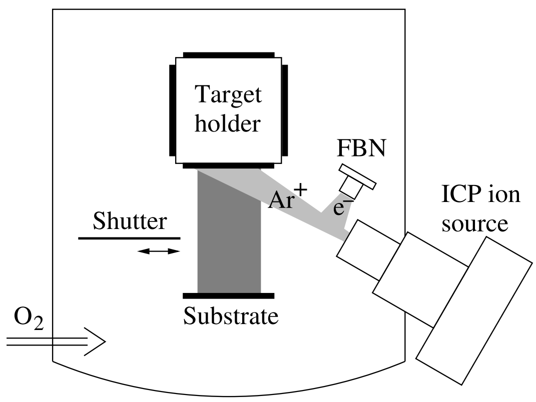

Fig. 8: Schematic diagram of the reactive ion-beam sputter deposition system.

Figure 7 shows the chamber interior of this new RIBS system. The system has an inductively coupled plasma (ICP) ion-beam source and a filamentless bridge neutralizer (FBN). Using a cubic water-cooled target holder, four different targets can be employed. Figure 8 shows a schematic of the RIBS system. The ion-beam strikes the target under an incident angle of 60°. The target and the substrate are parallel. Additionally oxygen can be introduced into the chamber in order to obtain stoichiometric layers with very low absorption.

3.2 Homogeneity distribution

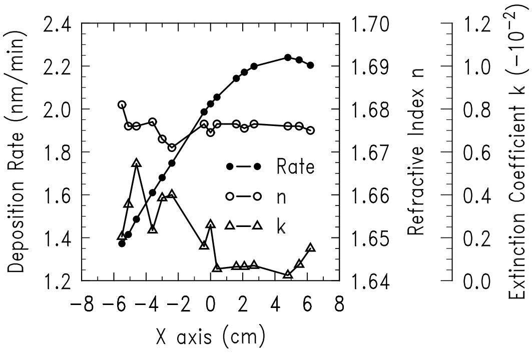

Fig. 9: Distribution of the deposition rate, the refractive index n, and the extinction coefficient k in x direction.

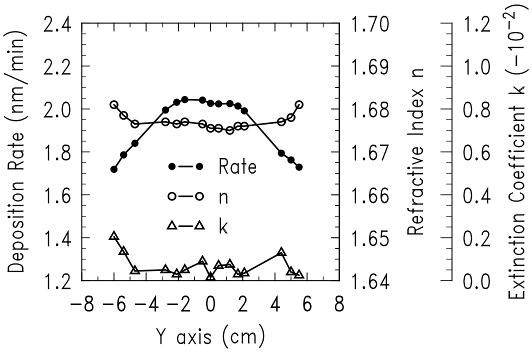

Fig. 10: Distribution of the deposition rate, the refractive index n, and the extinction coefficient k in y direction.

In Fig. 9 and Fig. 10, the distribution of the deposition rate, the refractive index n, and the extinction coefficient k in the x and y direction are shown. The measurement is performed with an ellipsometer at a wavelength λ of 632.8 nm. The x direction is in the plane of the ion-beam (see Fig. 8). In this direction the deposition rate increases due to the fact that more sputtered material is emitted from the target in the direction away from the ion-beam source. This can be simulated and is described in more detail in [1]. The deviation of the refractive index n is very low at a value of $n = 1.675$. The extinction coefficient k decreases and shows a minimum between the values 0 and 4 cm on the x axis, then it increases again. The y direction is the direction perpendicular to the plane of the ion beam. The deposition rate shows a decrease at the edges of the substrate holder, but is rather homogeneous in the center. This is due to the Gaussian intensity distribution of the ion beam resulting in a similar distribution for the flow of the sputtered material. The distribution of the refractive index n is very low and increases only marginally to the sides. The extinction coefficient k is constant.

3.3 Further steps

The next step for this deposition system is the installation of a load-lock system to avoid the vent of the main chamber. Also a substrate manipulator must be added for the movement of the samples to ensure a good homogeneity of the deposited materials. In the future, a second ion-beam source should be installed to assist the deposition to achieve layers with very low absorption.

4. Conclusion

AR/HR coatings on lasers have been deposited. The characterization of the coatings can be done by the ratio of the outgoing light at the AR side and the HR side. However, the ratio is lower than the calculated value. Additionally, it has been shown that on-wafer coating of dry-etched lasers is possible.

The construction of a new reactive ion-beam sputter deposition system is completed and first experiments have been performed successfully. This raises hopes for high quality coatings after the installation of a load lock and a substrate manipulator.

References

[1] M. Tilsch, *Eigenschaften ionenstrahlgesputterter optischer* SiO_2*- und* TiO_2*-Schichten bei unterschiedlichen Wachstumsbedingungen und Veraenderungen bei thermischer Nachbehandlung*, PhD thesis, University of Darmstadt, Darmstadt, Germany, 1997.

[2] S. Lorch, "Optical coatings for laser facets fabricated by reactive ion-beam sputter deposition," *Annual Report 2001,* University of Ulm, Optoelectronics Department, ch. 6, pp. 67–72, 2002.

[3] A. Macleod, *Thin Film Optical Filters*, Bristol, Philadelphia, London: Institute of Physics Publishing (IoP), 3. ed., 2001.

[4] D. Sowada, *Material- und Prozesstechnologien fuer langwellige Laserdioden mit Vertikalresonator*, PhD thesis, University of Ulm, Ulm, Germany, August 1999.

[5] R. Atkinson, "Development of a wavelength scanning laser calorimeter," *Appl. Optics*, vol. 24, no. 4, pp. 464–471, 1985.

[6] H.R. Kaufman and R.S. Robinson, *Operation of broad-beam sources*, Alexandria, Virginia: Commonwealth Scientific Corporation, 1987.

[7] K.J. Ebeling, *Integrated Optoelectronics*, Berlin: Springer-Verlag, 1993.

[8] R. Michalzik, *Modellierung und Design von Laserdioden mit Vertikalresonator*, PhD thesis, University of Ulm, Ulm, Germany, July 1996.

High-Power 980 nm InGaAs/AlGaAs Semiconductor Laser Amplifier with Surface-Emitting Master Oscillator

Frank Demaria, Eckart Schiehlen and Heiko Unold

We report on a hybrid setup using vertically emitting master lasers and a tapered high-power laser-amplifier. The first order mode from a vertical cavity surface emitting laser with a power of 2.1 mW has been boosted up to 1.5 W collimated optical output power. By coupling the light emission of an optically pumped external-cavity semiconductor-disk laser into the laser amplifier over a single-mode fiber, we achieved a continuous wave optical output power of 2.7 W in the collimated output beam. The sensitivity of the coupling efficiency with respect to the vertical lens position has been measured and compared to the results which have been achieved using an edge-emitting ridge-waveguide laser.

1. Introduction

Usually, in a master-oscillator power-amplifier (MOPA) setup, edge-emitting single-mode lasers are used for generating the laser signal. The diffraction limited beam of several milliwatts is optically amplified to an output power of some watts by nearly preserving the beam quality. However the master laser must not necessarily be an edge emitter. Also surface-emitting lasers are interesting signal beam sources. Vertical cavity surface emitting lasers (VCSELs) are well established devices in optical data transmission, like for example in short distance high-speed optical data link applications. However, for some other applications they suffer from their low optical output power. Especially if operation in the fundamental mode is required, the optical power that can be provided is in the range of a few mW. One possibility to overcome that problem is the use of an edge-emitting power amplifier. For applications which require an even higher optical power in the fundamental mode, the VCSEL can be substituted by a diode-pumped semiconductor disk laser which can provide that [1]. Both types of semiconductor lasers have in common that the wavelength can be adjusted to an arbitrary value over a wide range. The proper choice of the different system parts leads to a tailor-made solution for many applications.

2. Experimental Results

2.1 Vertical-cavity surface-emitting master oscillator

For the first time we demonstrate the amplification of the laser emission of a VCSEL up to values significantly over 1 W. In Fig. 1, the according curve shows the measurement

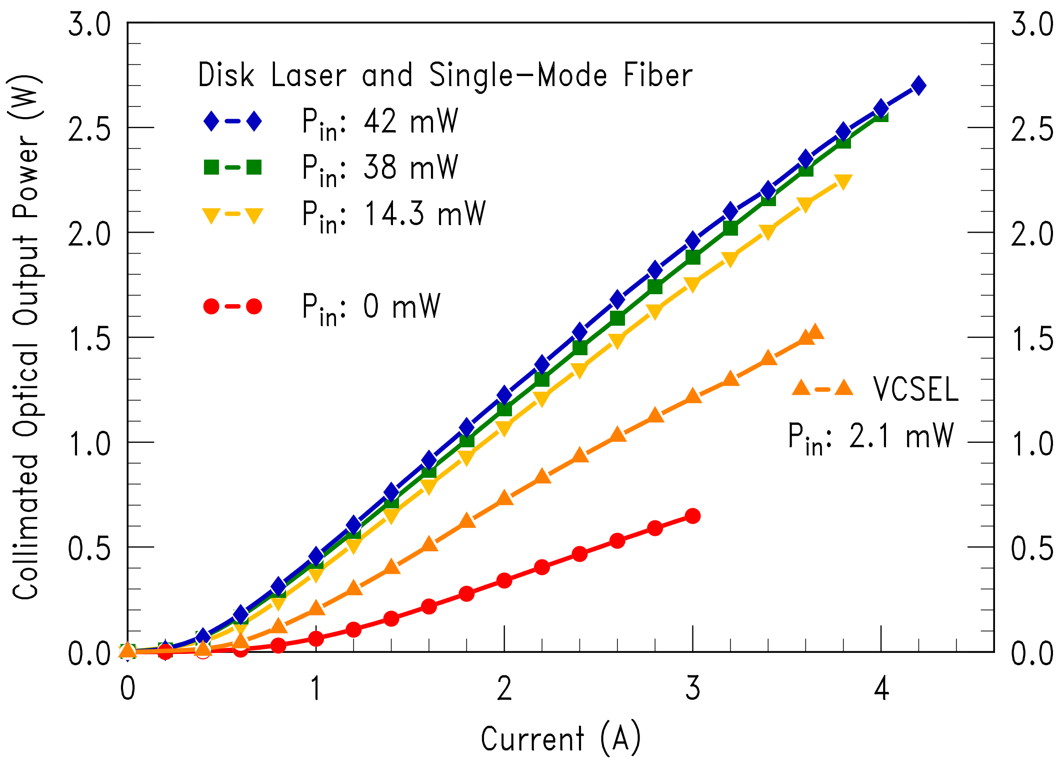

Fig. 1: Output characteristics of a laser amplifier with 6° full taper angle and a length of 2.5 mm. The optical input power is provided by an optically pumped external-cavity semiconductor disk laser and coupled over a single-mode fiber with 5.9 μm core diameter and a Faraday isolator. The curve with 2.1 mW optical input power shows the measurement with a single-mode VCSEL. Here, the optical power is coupled into the amplifier by two 6.5 mm focal-length-collimator lens systems and a Faraday isolator.

where the 2.1 mW optical power in the collimated beam is boosted up to a value of 1.52 W at an amplifier current of 3.65 A. The coupling has been performed by two 6.5 mm focal length collimator lens systems and a Faraday isolator for optical feedback suppression. By turning the VCSEL around his optical axis, the polarization direction has been optimized. The 2.5 mm-long tapered laser amplifier was mounted on a temperature stabilized heat sink at 18° C with a copper-tungsten heat spreader.

2.2 External-cavity disk-laser master oscillator

The emission of an optically diode-pumped semiconductor disk laser with a fairly high output power of up to 42 mW in a 5.9 μm core diameter single-mode fiber is suitable to achieve good saturation of the tapered amplifier. This leads to an even better suppression of the amplified spontaneous emission. According to Fig. 1, at a current of 4.2 A the optical output power in the collimated beam was measured to be 2.7 W. Together with the comparatively broad focal beam width in the vertical direction, the high optical input

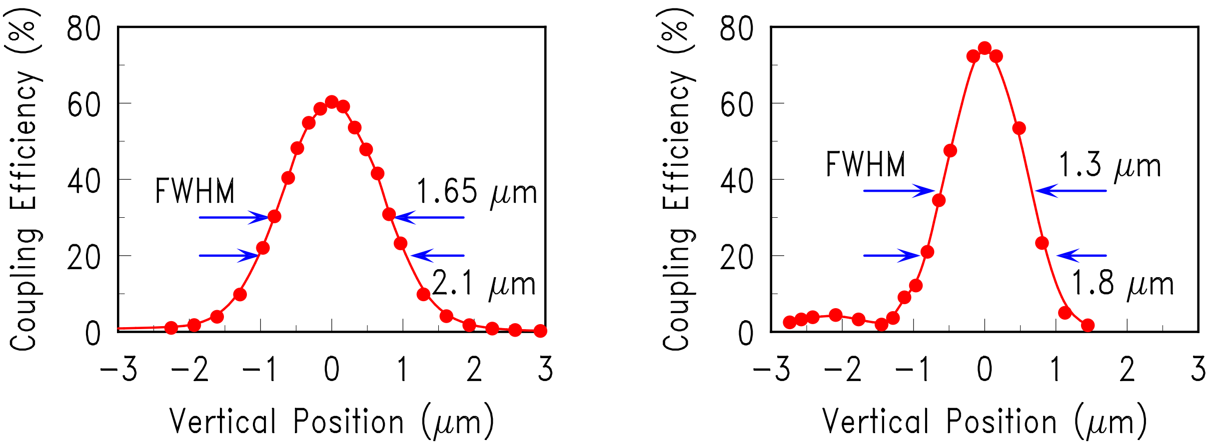

Fig. 2: Comparison of the sensitivity of coupling in the vertical direction for a circular beam (left) emitted from a single-mode fiber with 5.9 μm core diameter and an edge-emitting single-mode laser (right). The accuracy of positioning to achieve 50% of the maximum value is shown, as well as the tolerance for achieving 20% absolute coupling efficiency.

power lowers the required accuracy in positioning for the optical coupling. Figure 2 illustrates the coupling issue in the most sensitive vertical direction. Depicted is the difference in coupling sensitivity between a circular beam (left) created by a single mode fiber and an elliptical beam emerging from an edge-emitting single mode laser (right). For a single mode fiber with an aspect ratio of 1 : 1, the focal diameter in the vertical direction is bigger than the one which is created by the edge emitter. As a result, the range where a moderate coupling efficiency of about 20% can be achieved is bigger for the fiber, whereas the maximum value of the efficiency that can be reached is bigger for the edge emitter. The method of measuring the coupling efficiency is described in detail in [2]. The amount

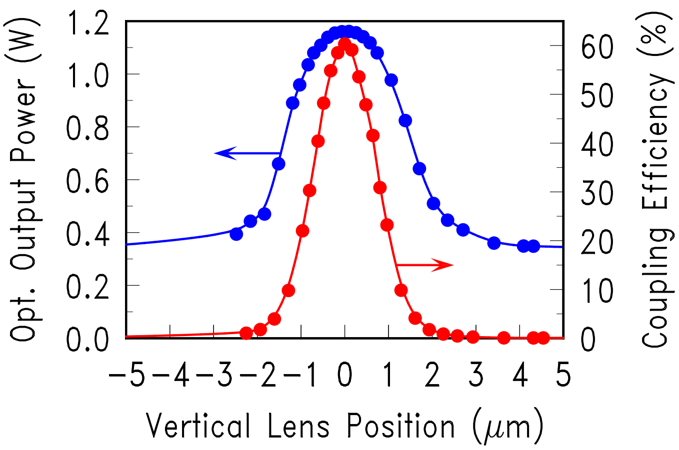

Fig. 3: Dependency of the coupling efficiency and the useful optical output power on the coupling lens position in vertical direction. The 22.1 mW optical emission from a 5.9 μm core-diameter single-mode fiber was coupled into the same amplifier as in Fig. 1. Please note the different scaling of the x-coordinate compared to Fig. 2.

of optical power that actually is coupled into the amplifier is the optical input power which can be measured multiplied the coupling efficiency. As a result, with a sufficiently high input power the coupling efficiency which is necessary for good saturation can be lowered. Figure 3 shows that with an input power of 22.1 mW emitted from the single-mode fiber, even with an absolute coupling efficiency of 20%, the optical output power can be stabilized at a high level. This is due to the good saturation of the amplifier. It has already been demonstrated that with a disk laser 170 mW optical power in a single-mode fiber is possible. In that case, the described effect gets more distinct.

3. Conclusion

It has been shown, that a MOPA combined with a VCSEL master oscillator can provide a relatively high optical power of 1.52 W. The promising properties of this system are its capabilities for free-space data transmission [3], the low feedback sensitivity of the master laser, and its low fabrication costs. The results with the disk laser exhibit the capacity of our laser amplifiers as multi-watt near diffraction-limited light sources. We also demonstrated that the circular laser beam, which is emitted from the single-mode fiber, leads to smaller requirements in positioning accuracy for the coupling optics also because the optical power emitted from the disk laser is sufficiently high.

References

[1] E. Schiehlen, M. Golling, and P. Unger, "Diode-pumped semiconductor disk laser with intra-cavity frequency doubling using lithium triborate (LBO)," *IEEE Photon. Technol. Lett.*, vol. 14, no. 6, pp. 777–779, 2002.

[2] F. Demaria and M. Mundbrod, "Properties and design features of tapered gain region semiconductor laser amplifiers," *Annual Report 2001, Dept. of Optoelectronics, University of Ulm*, pp. 51–61.

[3] G. Jost, "High-power semiconductor laser amplifier for free-space communication systems," *Annual Report 1998, Dept. of Optoelectronics, University of Ulm*, pp. 64–68.

Properties of Ridge-Waveguide Lasers

Manfred Mundbrod

Ridge-waveguide lasers are known to exhibit laser emission with a very good beam quality. In this article, a fabrication process for these devices with a self-aligned p-contact is described which accounts for several advantages as e.g. a symmetric current injection. For lasers with varying ridge width, the beam quality was analyzed using the M^2-method. Additionally, the optical near and far fields were measured. The best results were obtained for a laser with a 4 µm wide ridge with M^2=1.15. These lasers show almost ideal Gaussian-shaped optical near and far fields.

1. Introduction

Presently, conventional edge-emitting semiconductor lasers occupy a strategic position in many industrial products. However, for applications such as nonlinear frequency doubling, more stringent specifications in terms of output power, beam quality, and some other spectral and electrical properties are required [1].
One promising approach to fulfill these requirements is the MOPA concept (master-oscillator power-amplifier) [2]. The master laser is characterized by good spectral properties and by a nearly diffraction-limited beam quality. However, these lasers are limited in output power. This problem can be overcome by coupling the laser beam into a tapered power amplifier which amplifies the master beam in a single pass and maintains the beam quality.

For this approach it is important to suppress spontaneous recombination of the carriers. This can be achieved by saturating the gain of the amplifier. Therefore, the intensity of the master laser, excluding coupling losses, must be higher than the saturation intensity

$$J_s = \frac{\hbar\omega j_{\mathrm{tr}}}{q g_0}$$

of the amplifier [3]. Since the output power of the master laser is limited, this can be achieved by implementing a single-mode waveguide-structure which acts as a preamplifier. Apart from power amplification, this preamplifier can also work as a mode filter which is a beneficial side effect.

2. Fabrication of the Devices

The epitaxial material for the lasers was provided by Ferdinand-Braun-Institut für Höchstfrequenztechnik, Berlin. The epitaxial design is described in principle in [4].

The first process step is to evaporate Ti, Pt, and Au layers onto the wafer as a p-contact to the diode. The ridge is then defined by etching two 30 μm wide trenches into the p-contact and the semiconductor. The Au-layer is wet-chemically etched in a J/KJ/H_2O solution and the Pt is then removed by Ar ion-beam sputtering. The Ti is etched in a HF-solution. The trenches are extruded into the semiconductor using chemically assisted ion-beam etching (CAIBE). Since the step in refractive index between ridge and trench region is determined by the etching depth, it is very important to meet the desired etching depth in order to obtain good beam quality and single lateral mode operation.

Etching the p-contact layers and the semiconductor trenches using the same lithography step provides several advantages. First, the p-contact covers the maximum possible area which leads to low p-contact resistance. However, the main advantage is that a symmetric current injection into the ridge is guaranteed as the p-contact is automatically self-aligned to the ridge. This eliminates also the need for complex alignment of the subsequent passivation step.

The passivation is formed by a Si_3N_4 layer which is opened on top of the ridge and in the scribing area. The whole structure is then covered by a second metalization which serves as a base for a thick electroplated Au layer. The laser process is finished by thinning the wafer to about 100 μm and applying a n-contact on the backside by evaporating Ge/Au/Ni/Au layers followed by an annealing process.
Finally, the wafer is cleaved into bars and an anti- and high-reflective coating is applied to the facets to passivate them and to support light emission in only one direction. Figure 1 shows an SEM micrograph of a completely processed laser and a cross section of the ridge region. The self-aligned p-contact can clearly be seen on top of the semiconductor ridge.

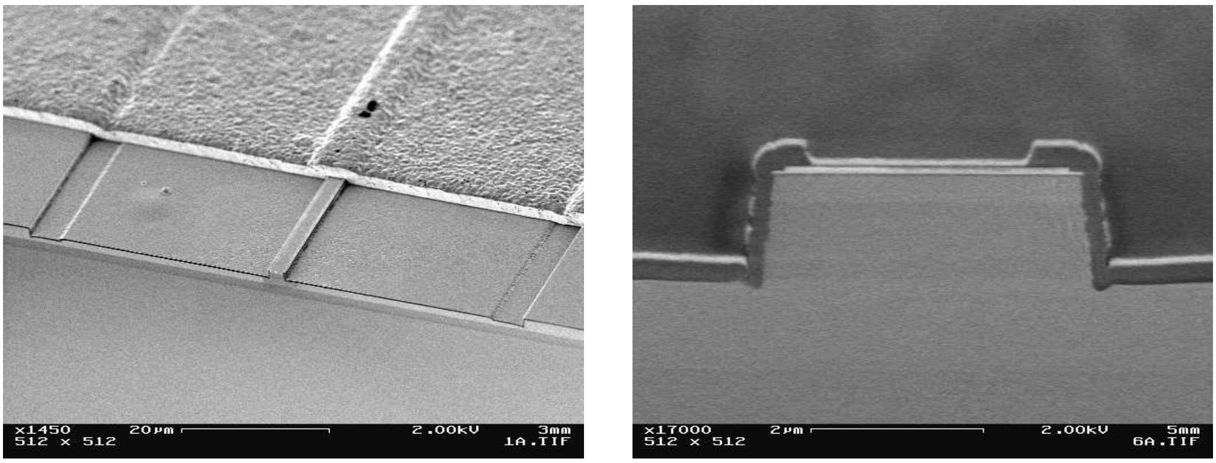

Fig. 1: SEM micrograph (left) and cross section (right) of a completely processed ridge. In the right picture, the self-aligned p-contact can be clearly seen.

3. Characteristics of the Lasers

3.1 V–I and L–I characteristics

The processed laser bars are then fixed with conductive glue to a copper plate. This facilitates the handling of the lasers for characterization purposes. In Fig. 2, the electrical and optical characteristics of a 6 μm wide ridge-waveguide laser are shown. The lasers have kink voltages which are slightly higher than the value which corresponds to the emission wavelength of 924 nm. The serial resistances are in the range of 6–7 Ω depending on the ridge width. The differential efficiency η_{d} ranges between 60 % and 71 %. The threshold currents for coated lasers do not strongly depend on the ridge width and vary from 16 mA to 18 mA. Wall-plug efficiencies of up to 40 % are possible.

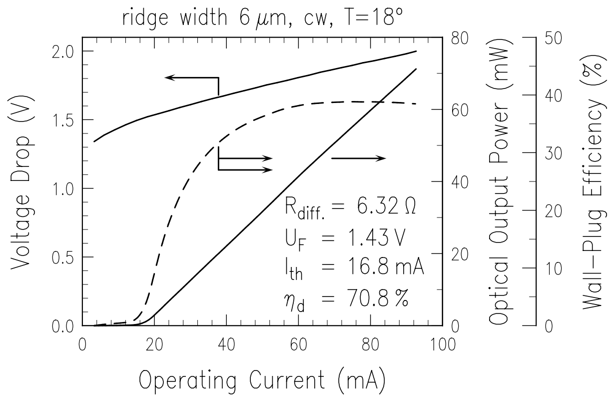

Fig. 2: L–I and V–I characteristics of laser with a 6 μm wide ridge.

3.2 Beam quality

For a good beam quality, much importance must be attached to the waveguide. In order to force a ridge-waveguide laser to operate only in the fundamental mode in a current range as wide as possible, the step in refractive index must not exceed a certain value for a given ridge width.

On the other hand, if the etch depth chosen is too small, the current can spread too widely or the mode is not guided at all. Additionally, the lateral profile of the guided mode must be Gaussian-shaped for a good beam quality. So the choice of the right etching depth and epitaxial design of the laser is critical.

As can be seen in Fig. 3, using the process described above a beam quality factor $M^2 < 1.2$ could be attained for a current range of 80 mA to 160 mA in both the fast and slow axis. The ridge width was 4 μm in this case. The beam quality factors were recorded with a ModeMasterPC from Coherent.

In Fig. 4, the M^2-values for lasers with different ridge widths are depicted. The etch depth was kept constant for all lasers. Again, the laser with a ridge width of 4 μm shows the

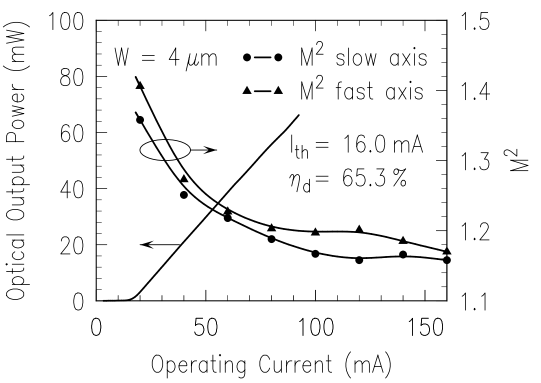

Fig. 3: *L–I* characteristics and beam quality factor M^2 in slow and fast axis for a ridge-waveguide laser with $4\,\mu$m wide ridge.

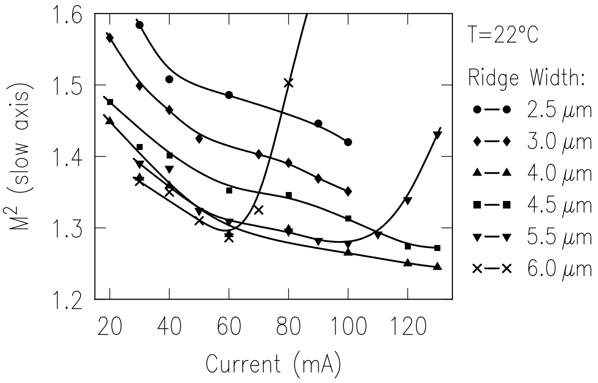

Fig. 4: Beam quality factor M^2 for ridge-waveguide lasers with varying ridge width.

lowest M^2-values over the measured current range. The broader lasers are initially better, but at higher currents, the lasers become multi mode and the beam quality degrades rapidly. For smaller ridges with $2.5\,\mu$m and $3\,\mu$m width, the etched trenches are not deep enough; this leads to a deviation from an ideal Gaussian-shaped mode profile and an increased M^2-value.

This can also be seen from Fig. 5, where the optical near fields of lasers for ridge widths of $2.5\,\mu$m, $3\,\mu$m, $4\,\mu$m, and $6\,\mu$m are compared with a Gaussian fit. The near field of the laser with a $4\,\mu$m wide ridge has the best fit to a Gaussian distribution. The other lasers that show higher M^2-values deviate significantly from the Gaussian distribution. The larger this deviation is, the higher the beam quality factor becomes.
As can be seen in Fig. 3, the $4\,\mu$m wide laser operates in the fundamental transverse mode over the whole measured current range; in fact, the beam quality factor actually decreases with increasing current. Also, as can be seen in Fig. 5, the optical near fields remain nearly Gaussian-shaped at high currents. When plotting all curves on a normalized scale it can be seen that there is almost no change in shape with increasing current.

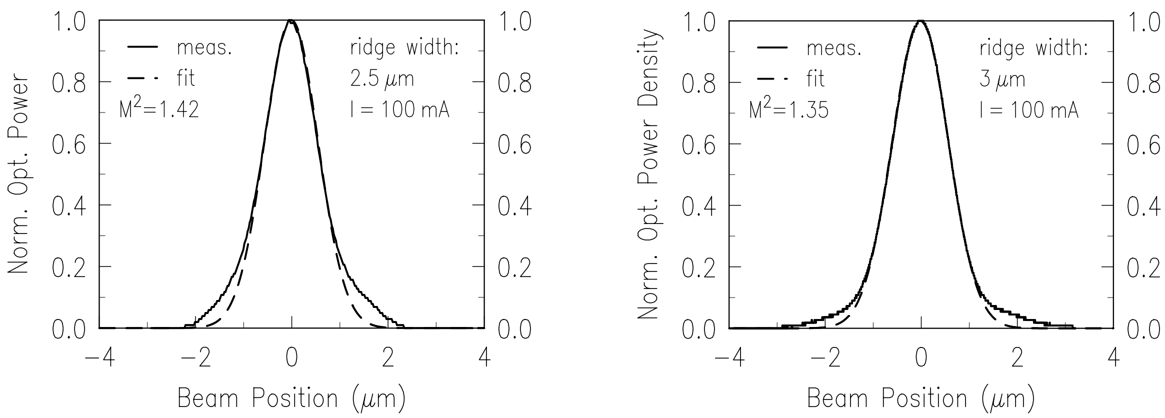

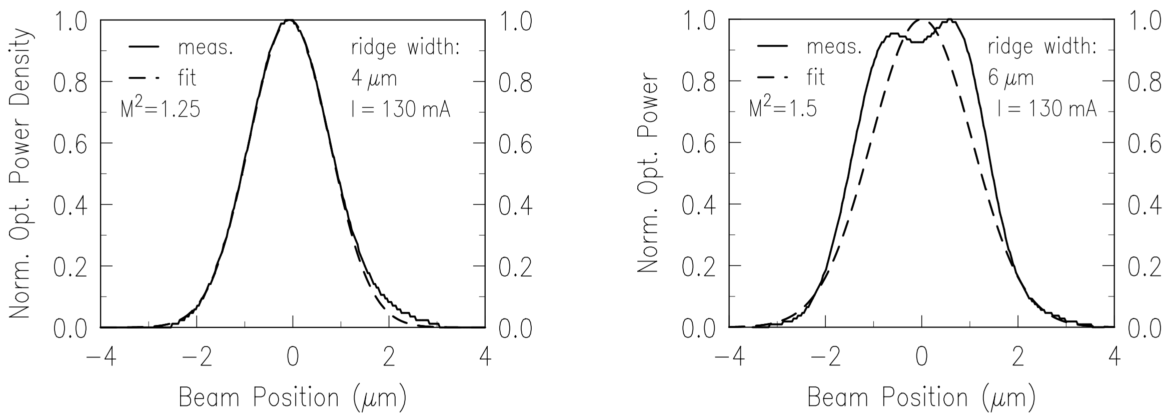

Fig. 5: Images of the optical near fields (solid lines) of lasers with with varying ridge widths and Gaussian fits (dashed lines). The near field of the $4\,\mu$m wide laser has the best fit to a Gaussian distribution.

The broader lasers, however, increasingly deviate from the ideal Gaussian shape when the drive current is raised. This can be seen in the right panel of Fig. 6. At higher currents, two maxima can clearly be resolved in the near field. This is responsible for the steep increase in the M^2-value for broad waveguides as described above (see Fig. 4).

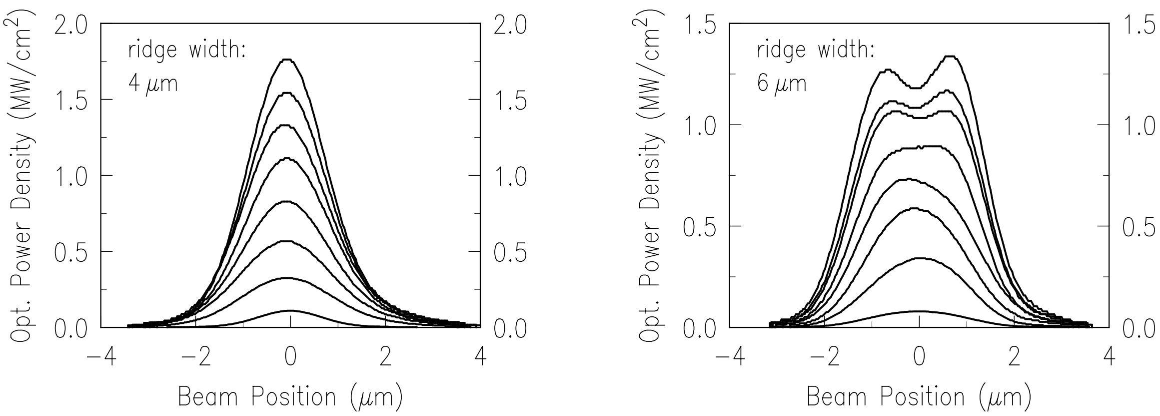

Fig. 6: Images of the optical near fields for different currents of a $4\,\mu$m and a $6\,\mu$m wide ridge-waveguide laser. The laser with the smaller ridge stays in the fundamental lateral mode with increasing current while the broader one does not.

Since the optical far field is connected to the near field by a fourier transform, the dependencies of the beam quality on the ridge width and the current reproduce themselves. A nearly ideal Gaussian far field is achieved only for lasers with a $4\,\mu$m wide ridge. This is depicted in Fig. 7. In Fig. 8, the far-field angles of lasers with varying ridge width are plotted versus the applied current. As one would expect, the far-field angles initially increase with decreasing ridge width. Additionally, the broader waveguides show increasing far-field angles with increasing current which again can be attributed to the decaying beam quality. For smaller ridges the far-field angles remain constant.

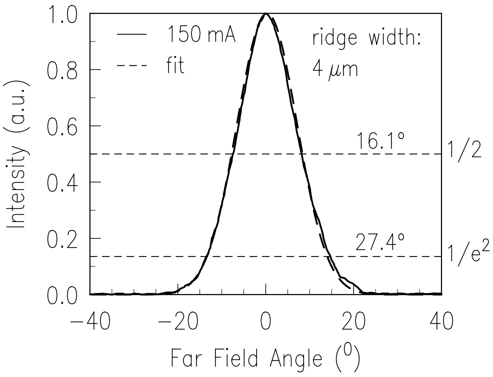

Fig. 7: Optical far field of a 4 μm wide laser at 150 mA. Due to the good beam quality also the far field shows a Gaussian shape.

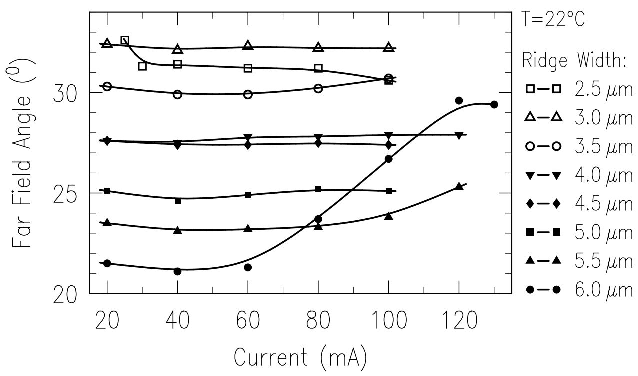

Fig. 8: Far-field angles versus the applied current for lasers with varying ridge widths. The increase in the far-field angle for broader lasers is due to the deteriorated beam quality at higher currents.

4. Conclusion

A fabrication process for ridge waveguide lasers with a self-aligned p-contact was described. These lasers feature a very good beam quality ($M^2 = 1.15$). However, the beam quality depends to a high degree on the design of the waveguide and its operating conditions. For a given etch depth, a variation of the ridge width of more than half a micron leads to a significant degradation of the beam quality.
If high output power and good beam quality are required at the same time, a ridge waveguide section can be combined with a gain-guided flared region. The flared region must be adjusted to the beam propagation of the optical output from the ridge section, in order to avoid any perturbation of the beam which would immediately degrade the beam quality.

References

[1] D. Woll, B. Beier, K. Boller, and R. Wallenstein, "1 W blue 465 nm radiation generated by frequency doubling of a high-power diode laser in critically phase-matched LiB_3O_5," *Opt. Lett.*, vol. 24, no. 10, pp. 691–693, 1999.

[2] S. O'Brien, A. Schoenfelder, and R. Lang, "5 W CW diffraction-limited InGaAs broad-area flared amplifiers at 970 nm," *IEEE Photon. Technol. Lett.*, vol. 9, no. 9, pp. 1217–1219, 1997.

[3] J. Walpole, "Semiconductor amplifiers and lasers with tapered gain regions," *Opt. Quantum Electron.*, vol. 28, pp. 623–645, 1996.

[4] J. Sebastian, G. Beister, F. Bugge, F. Buhrandt, G. Erbert, H.G. Hänsel, R. Hülsewede, A. Knauer, W. Pittroff, R. Staske, M. Schröder, H. Wenzel, M. Weyers, and G. Tränkle, "High-power 810 nm GaAsP-AlGaAs diode lasers with narrow beam divergence," *IEEE J. Select. Topics Quantum Electron.*, vol. 7, pp. 334–339, 2001.

5 W in a Multi-Mode Fiber from a Single 980-nm-Emitting Laser Diode

Eckard Deichsel

The epitaxy and fabrication of 980-nm-emitting broad-area laser diodes is presented. These devices are suitable for multi-mode fiber (MMF) coupling. We achieved 5.1 W in a 220-μm-core MMF at 18° C in cw operation. The threshold current was 240 mA and a maximum overall system efficiency of 49 % was achieved. The fiber coupling efficiency was between 80 and 85 %.

1. Introduction

High-power laser diodes offer a variety of advantages compared to gas or solid-state lasers, e.g. small dimensions, low prices, and high efficiencies. Many applications like material treatment, spectroscopy, and pumping of solid-state lasers and fiber amplifiers are possible using these high-power broad-area laser diodes [1, 2]. The implementation of diode lasers in medicine and dental treatments is becoming more and more popular. However, medical applications require high powers in fibers with wavelengths from the visible to the near infrared spectrum. Examples for medical applications of lasers are described in [3, 4]. Furthermore, high-power broad-area laser diodes can easily be fabricated in large quantities, offer high powers, and are available for a large spectral range.

2. Epitaxy

The epitaxial layer sequence of these edge-emitting laser diodes is a molecular-beam epitaxy (MBE)-grown graded-index separate-confinement heterostructure (GRINSCH). The active region consists of an 8-nm-thick compressively strained $In_{0.20}Ga_{0.80}As$ single quantum well which is surrounded by 10-nm-thick GaAs spacing layers followed by doped AlGaAs grading and cladding layers. The p- and n-dopants are C and Si, respectively. The emission wavelength is in the range of 980 nm and the internal efficiency of the epitaxial material is 78 % with an intrinsic absorption of 2.1 cm^{-1}. The vertical far-field angle was measured to be 34° and 69° at full-width half maximum (FWHM) and $1/e^2$, respectively. Details of the epitaxial growth process are described in [5].

3. Fabrication

The fabrication sequence consists of several process steps beginning with the definition of 200-μm-wide p-contact stripes by removing the highly p-doped layer outside of the stripe area using wet chemical etching. The etched surface is passivated with SiN using plasma-enhanced chemical-vapour deposition (PECVD). The contact windows in the passivation layer are opened by CF_4 reactive ion etching (RIE). The e-beam-evaporated Ti/Pt/Au p-contact metalization is patterned using lift-off technique. After substrate thinning, a Ge/Au/Ni/Au n-contact is applied on the backside of the wafer which is strengthened by a Ti/Ni/Au top metalization after anealing. Laser bars with 900 μm resonator length are cleaved and the facets are covered with anti- and high-reflection (AR/HR) coatings. After separation, the devices were soldered junction-side down on diamond heat spreaders mounted on copper submounts. Figure 1 shows such a high-power laser diode.

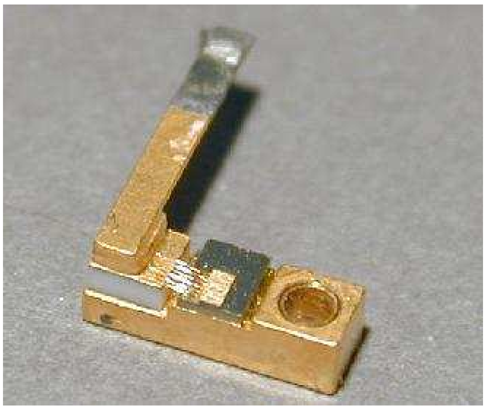

Fig. 1: High-power laser diode mounted junction-side down on a diamond heat spreader.

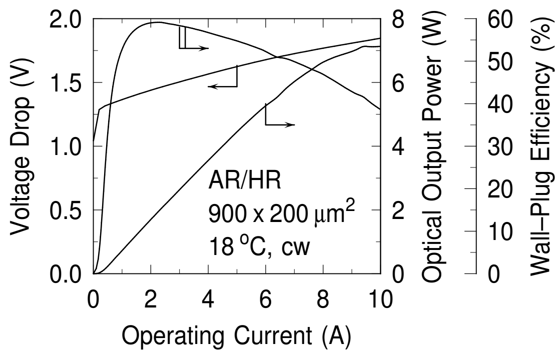

Fig. 2: Characteristics of a high-power broad-area laser diode showing output power, voltage, and conversion efficiency.

The broad-area laser diode exhibits output powers of up to 7.1 W at a pump current of 10 A at 18 °C in cw operation, which is shown in Fig. 2. The differential quantum efficiency is 77 % and the threshold current is 250 mA. Operating currents between 1 and 5 A exhibit conversion efficiencies above 50 % with a maximum conversion efficiency of 59 % at 2 A pump current.

4. Fiber Coupling

The active coupling into the 220 μm multi-mode fiber was performed by Ceramoptec, Bonn, Germany. Figures 3 and 4 show the detailed view of the fiber coupled high-power laser diode and the setup with laser modul, water cooling and electrical control.

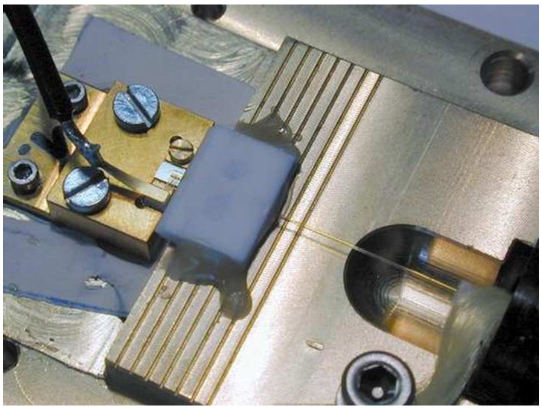

Fig. 3: Detailed view of the fiber-coupled laser diode with electrical connections and the multi-mode fiber.

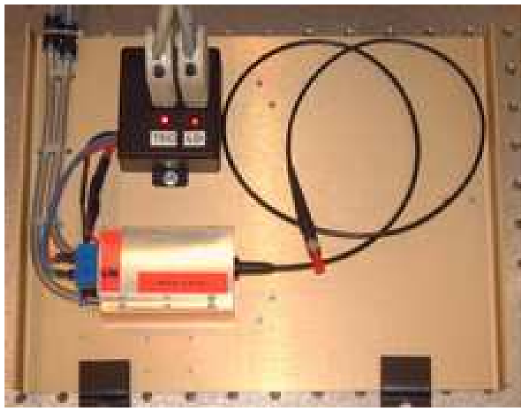

Fig. 4: Setup with laser modul, electrical control, and water cooling.

5. Characterization

Figure 5 shows the *L–I* characteristics of such a device at 18 °C in cw operation. Additionally, the overall-system and the coupling efficiencies are shown in the same diagram. For comparison, the output power of the laser diode before fiber coupling is also shown as dashed line. The power was measured using a calibrated integrating sphere. A maximum power of 5.1 W in the 220 μm multi-mode fiber at 7.5 A pump current is achieved [6]. The threshold current is 240 mA and a maximum overall-system efficiency of 49 % is obtained. For currents larger than 1 A, this efficiency is over 40 %. The fiber coupling efficiency is between 80 and 85 % for all pump currents.

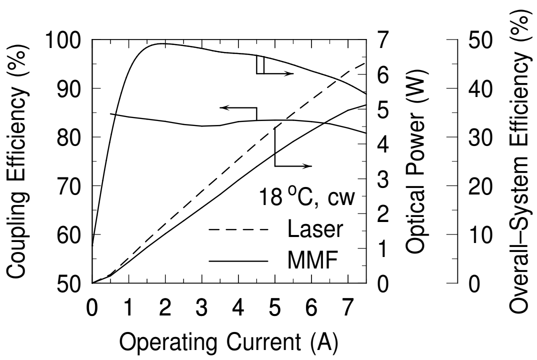

Fig. 5: Characteristics of a coupled laser diode showing the optical power in the multi-mode fiber, the coupling efficiency, and the overall-system efficiency.

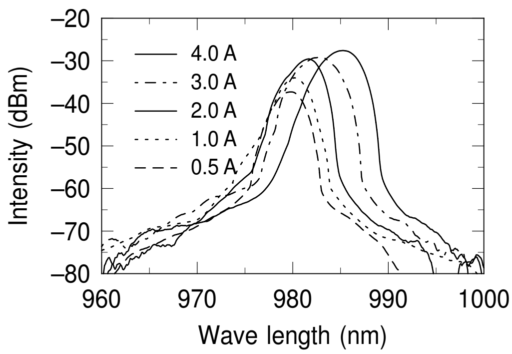

Fig. 6: Spectra of a coupled laser diode at 18 °C in cw operation for different pump currents.

A center wavelength of 980 nm was measured with a spectral width of 5 nm at a pump current of 500 mA. With increasing current, the spectrum shifts toward longer wavelengths and reaches at 4 A a wavelength of 985 nm and a spectral width of 10 nm.

6. Conclusion

We presented the epitaxy, the fabrication process, and the characteristics of a 980 nm high-power broad-area laser diode. The uncoupled device reaches an output power of up to 7.1 W with a maximum conversion efficiency of 59 %. The power in a 220 μm multi-mode fiber is 5.1 W with a maximum overall-system efficiency of 49 %.

References

[1] P. Bousselet, C. Simonneau, C. Moreau, L. Provost, P. Lambelet, X. Rejeaunier, F. Leplingard, L. Gasca, and D. Bayart, "+33 dBm output power from a full C-band cladding diode-pumped EDFA," in *ECOC 2002*, Copenhagen, 2002.

[2] C. Codemard, K. Yla-Jarkko, J. Singleton, P. W. Turner, I. Godfrey, S.-U. Alam, J. Nilsson, J. Sahu, and A. B. Grudinin, "Low noise, intelligent cladding pumped l-band EDFA," in *ECOC 2002*, Copenhagen, 2002.

[3] J. L. Hargrove, "Soft Tissue Laser-Assisted Class V Composite Restorations," *Contemporary Esthetics and Restorative Practice*, vol. 1, 2000.

[4] W. Ceccetti, "980 nm high-power diode laser in surgical applications," *Biomedical Optics Instrumentation and Laser Assisted Biotechnology*, pp. 227–230, 1996.

[5] R. Jäger, J. Heerlein, E. Deichsel, P. Unger, "63 % wallplug efficiency MBE grown InGaAs/AlGaAs broad-area laser diodes and arrays with carbon p-type doping using CBr_4," *JCG*, vol. 201/202, pp. 882–885, 1999.

[6] E. Deichsel, R. Jäger, and P. Unger, "5 W in a multi-mode fiber from a single 980-nm-emitting laser diode," in *ECOC 2002*, Copenhagen, 2002.

Growth of GaAsSb/GaAs Double Quantum Well Lasers Emitting Near 1.3 μm

Irene Ecker and Susanne Menzel

We report on the growth and characterization of GaAsSb-based laser diodes for the long wavelength range around 1300 nm suited for telecom applications.

1. Introduction

In fiber-optic communication systems, light emitting devices at 1.3 μm are widely used. As cost-effective sources for, e.g., metro access networks, manufacturable vertical-cavity surface-emitting laser diodes (VCSELs) with a corresponding emission wavelength are highly desirable [1]. GaAs based devices might prove superior to their InGaAsP counterparts in aspects like thermal stability, single epitaxial growth capability, and use of large diameter high-quality inexpensive GaAs substrates [2]. Until now various approaches to VCSEL structures have been investigated. These concentrate mainly on InAs/InGaAs quantum dots, GaInNAs and GaAsSb quantum films [3, 4, 5]. As an intermediate step towards 1.3 μm VCSELs, in this report we present results on the growth of GaAsSb/GaAs edge-emitting laser diodes.

2. Growth of Edge-Emitting Laser Diodes

The epitaxial layers were grown with both, the group V precursor arsine and solid arsenic. For antimony a solid source is used. The laser active region of the investigated edge emitting laser diodes consists of two 7 nm thick compressively strained GaAsSb quantum wells and a 30 nm thick GaAs barrier. The double quantum well structure is surrounded by GaAs with a thickness of 40 nm. The active region is embedded in carbon and silicon doped AlGaAs cladding layers.

3. Device Characteristics

We report on the characterization of GaAsSb/GaAs broad area laser diodes with as-cleaved facets under continuous wave (cw) and pulsed operation without heat sinking at room temperature. The cw output characteristics and optical spectrum of a device with 800 μm length and 20 μm width are shown in Fig. 1. The threshold current density is as low as 357 A/cm^2 for a center wavelength exceeding 1160 nm. The temperature dependence of the threshold current density is measured within a range of 283 to 296 K, yielding a characteristic temperature $T_0 = 68\,\mathrm{K}$. This value is comparable to published GaAsSb and InGaAsP laser data and is attributed to the weak electron confinement in the GaAsSb quantum wells [6, 7, 8].

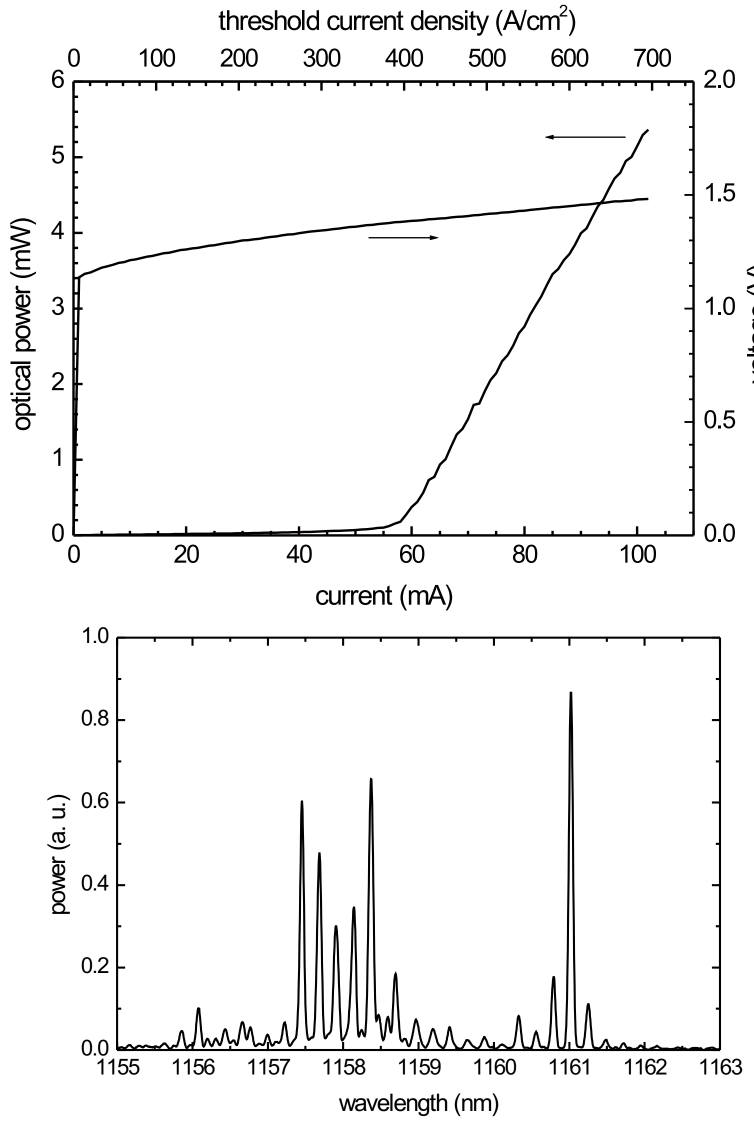

Fig. 1: CW operation characteristics of a GaAsSb/GaAs double quantum well (DQW) laser diode (top) and optical spectrum on a linear power scale (bottom).

The light-current characteristic of a $800 \times 20\,\mu\mathrm{m}^2$ device with emission near $1.3\,\mu\mathrm{m}$ is depicted in Fig. 2. The diode is operated with pulse lengths of 50 ns and 1 kHz repetition rate. The threshold current density is $2.2\,\mathrm{kA/cm}^2$. Laser oscillation is observed at about 1294 nm wavelength.

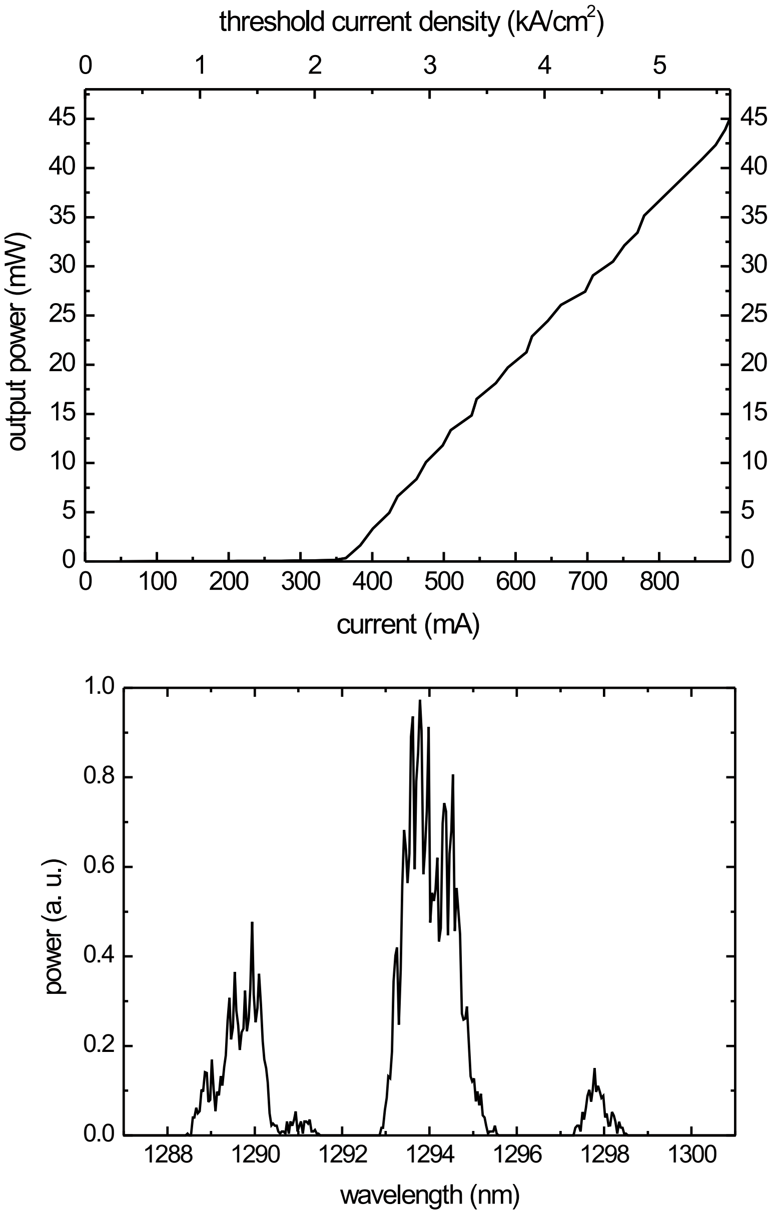

Fig. 2: Light-current characteristic of a GaAsSb/GaAs DQW laser diode under pulsed operation (top) and corresponding spectrum showing emission at 1294 nm (bottom).

4. Conclusion

The results attained so far for the active material are currently being transferred to surface-emitting devices. Presently, edge-emitting laser diodes processed from wafers with VCSEL-type layer structures show laser operation at about 1260 nm with threshold current densities of 1.1 kA/cm^2. Optimized distributed Bragg reflector doping profiles and increased round-trip gain through multiple quantum wells have been identified as key improvements necessary to achieve VCSEL operation in the future.

References

[1] K.D. Choquette, "The race toward long wavelength VCSELs," in *IEEE Lasers and Electro-Opt. Soc. Ann. Meet., LEOS*, San Diego, CA, USA, pp. 594–595, November 2001.

[2] V.M. Ustinov and A.E. Zhukov, "GaAs-based long-wavelength lasers," *Semicond. Sci. Technol.*, vol. 15, pp. R41–R54, 2000.

[3] J.A. Lott, N.N. Ledentsov, V.M. Ustinov, N.A. Maleev, A.E. Zhukov, A.R. Kovsh, M.V. Maximov, B. V. Volovik, Zh. I. Alferow, and D. Bimberg, "InAs-InGaAs quantum dot VCSELs on GaAs substrates emitting at 1.3 μm," *Electron. Lett.*, vol. 36, pp. 1384–1386, 2000.

[4] K.D. Choquette, J.F. Klem, A.J. Fischer, O. Blum, A.A. Allerman, I.J. Fritz, S.R. Kurtz, W.G. Breiland, R. Sieg, K.M. Geib, J.W. Scott, and R.L. Naone, "Room temperature continuous wave InGaAsN quantum well vertical-cavity lasers emitting at 1.3 μm," *Electron. Lett.*, vol. 36, pp. 1388–1390, 2000.

[5] M. Yamada, T. Anan, K. Kurihara, K. Nishi, K. Tokutome, A. Kamei, and S. Sugou, "High-performance 1.3 μm VCSELs with GaAsSb/GaAs quantum wells," in *IEEE Lasers and Electro-Opt. Soc. Ann. Meet., LEOS*, San Diego, CA, USA, pp. 598–599, November 2001.

[6] S.W. Ryu and P.D. Dapkus, "Low threshold current density GaAsSb quantum well (QW) lasers grown by metal organic vapor deposition on GaAs substrates," *Electron. Lett.*, vol. 36, pp. 1387–1388, 2000.

[7] O. Blum and J.F. Klem, "Characteristics of GaAsSb single-quantum-well-lasers emitting near 1.3 μm," *IEEE Photon. Technol. Lett.*, vol. 12, pp. 771–773, 2000.

[8] M. Yamada, T. Anan, K. Tokutome, A. Kamei, K. Nishi, and S. Sugou, "Low-threshold operation of 1.3 μm GaAsSb quantum-well-lasers directly grown on GaAs substrates," *IEEE Photon. Technol. Lett.*, vol. 12, pp. 774–776, 2000.

Diode-pumped Intra-cavity Frequency Doubled Semiconductor Disk Laser with Improved Output Beam Properties

Eckart Schiehlen and Michael Riedl

Diode-pumped semiconductor disk lasers are based on the principle of diode-pumped solid-state disk lasers. This laser type is also referred to as VECSEL (Vertical External Cavity Surface Emitting Laser). Semiconductor disk lasers show excellent beam characteristics in combination with high output power. With this novel approach, the current injection problems of VCSELs and the facet degradation effects of edge-emitting lasers due to the high optical intensities at the laser mirrors can be overcome. Furthermore, the external cavity of the disk laser can be equipped with additional elements such as nonlinear crystals for frequency doubling. In this article we present an InAlGaAs-based semiconductor disk laser with intra-cavity frequency doubling having an output power of 23 mW at 491 nm.

1. Introduction

Based on the principle of diode-pumped solid-state disk lasers, diode-pumped semiconductor disk lasers have been reported recently [1]. This relatively new type of laser is also referred to as VECSEL (Vertical External Cavity Surface Emitting Laser). Any conventional direct semiconductor material can be used for this type of laser. In this article, we present an InAlGaAs-based semiconductor disk laser without any additional phosphorus containing layers for strain compensation. Semiconductor disk lasers show very good beam characteristics in combination with high output powers. Because of the disk geometry, a nearly one-dimensional heat flow can be assumed. This allows power scaling by a simple enlargement of the active area.

As for all semiconductor lasers, the emission wavelength can be chosen by the epitaxial design. There is no limitation to discrete emission lines like for commonly used solid-state laser gain materials (i.e. Nd:YAG thin-disk lasers). In addition to this, the semiconductor material's absorption spectrum is broad and the absorption coefficient for the pump light is much higher. Therefore, no sophisticated multi-pass pump optic is required as for solid-state disk lasers [2].

Electrically pumped single-mode VCSELs (Vertical Cavity Surface Emitting Lasers) show an almost perfect beam profile, but the maximum single-mode output power is limited to approximately 6 mW at present time [3],[4]. When exceeding the power range of a VCSEL by increasing the active area, higher order transverse modes are observed [5], which can be explained by inhomogeneous current injection and the lack of transverse mode discrimination.

Edge-emitting lasers do not emit in the fundamental axial and transverse mode at high optical output power [6] because of inhomogeneous electrical pumping, spatial hole burning, short axial mode distance, and thermal effects inside the active region. Inevitable intensity variations inside the laser diode (filamentations) are primary responsible for Catastrophic Optical Mirror Damage (COMD). COMD occurs suddenly and destroys the laser diode facet. Moreover, the beam profile of edge-emitting lasers is highly asymmetric and tends to higher order modes at high output powers. In contrast to other semiconductor lasers, semiconductor disk lasers have an external cavity which can be equipped with various intra-cavity elements e.g. for frequency selection or frequency conversion. Additionally, the high intra-cavity power is advantageous for frequency conversion processes using nonlinear optical crystals.

Based on the InAlGaAs material system, we presented a disk laser oscillating in the TEM_{00} mode with a maximum output power of 0.28 W in continuous wave (CW) operation. Our semiconductor disk laser is pumped by a commercial 1.5 W 808 nm high-power broad-area laser diode. The output beam shows a circular symmetric Gaussian intensity distribution, depending on the mirror adjustment. The high single-mode fiber coupling efficiency of more than 70 % also indicates the very good focusability of the beam [7].

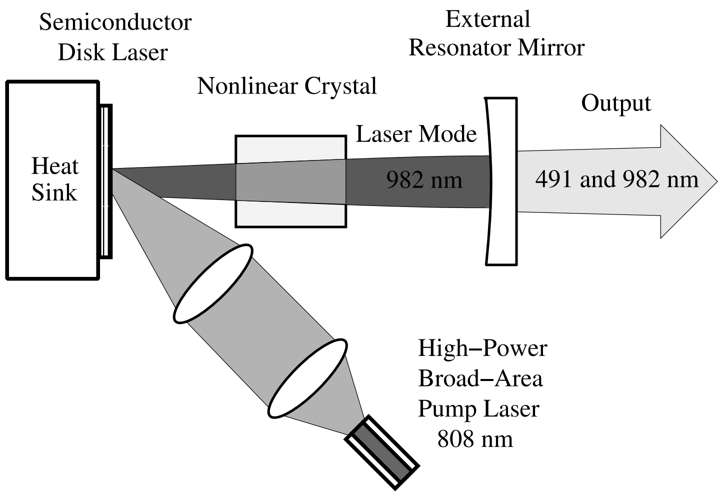

Fig. 1: Schematic setup of a diode-pumped semiconductor disk laser. The laser cavity is formed by a Bragg mirror and an external concave dielectric mirror. Pumping of the gain medium (InGaAs quantum wells) is done optically by a laser beam. A nonlinear crystal is placed inside the external cavity for frequency doubling.

As shown in Fig. 1, the semiconductor chip is mounted on a heat sink and forms a resonator together with an external concave mirror. The laser pump beam is focused onto the chip at an angle of about 45°, and should ideally result in a round spot. A nonlinear optical crystal can be placed inside the external cavity for frequency doubling. The laser cavity is formed by an AlAs/GaAs Bragg mirror (distributed Bragg reflector, DBR) which is grown directly on the GaAs substrate and an external concave dielectric mirror. Because of the short gain medium length, the external mirror reflectivity has to be $\sim 99\,\%$. The Bragg mirror should exceed $99.9\,\%$ to avoid additional losses. A stable concentric (hemispheric) resonator configuration is used here. The length of the laser cavity is variable and is mainly given by the mirror radius. The epitaxial structure is a classical Resonant Periodic Gain (RPG) structure [8],[9].

2. Epitaxial Design

The gain is provided by 12 8 nm-thick compressively strained $In_{0.2}Ga_{0.8}As$ quantum wells in the antinodes of the standing wave pattern, separated by (Al)GaAs pump light absorbing layers. Electron-hole pairs are generated by absorption of the pump light in the (Al)GaAs absorbing layers and relax into the InGaAs quantum wells where they undergo stimulated emission. The very strong absorption coefficient of the semiconductor material yields to short absorption lengths for the pump light of only a few microns. The absorbing layers are realized as GRaded-INdex (GRIN) areas to support carrier movement into the quantum wells. A standing wave builds up within the resonator with the intensity maxima located in the quantum-well regions. A surface barrier made of AlGaAs with an Al content of $30\,\%$ prevents excited carriers from recombining at the wafer surface. This surface barrier layer is transparent for the pump wavelength. Optical free-carrier absorption (of photons at the emission wavelength) is kept to a minimum since the epitaxial layers are not intentionally doped. The monolithically grown Bragg mirror consists of 30 pairs of alternating AlAs/GaAs layers with a thickness of $\lambda_0/4n$.

3. Processing and Mounting

For semiconductor disk lasers, no lateral (lithographic) patterning is necessary. Grown by molecular beam epitaxy (MBE), the wafer surface is coated by a dielectric antireflection coating. The substrate is thinned to $\sim 60\,\mu$m, metallized with Ti/Pt/Au layers and chips with the desired size are cleaved. Using Indium solder, these chips directly are bonded to a copper heat sink. No electric contacts are necessary, so no additional heat originating from the ohmic contacts is generated which would raise the device temperature and reduce the conversion efficiency.

4. Experimental Results

In continuous wave (CW) operation, we achieve 0.28 W in the fundamental transverse mode using an external mirror with a reflectivity of $R = 99\,\%$ and a radius of curvature of $R_C = 50\,$mm. The diameter of the laser-active area is estimated to be $100\,\mu$m. The peak wavelength is around $\lambda = 982\,$nm. A spectrum is shown in Figure 2. The beam-quality is very good, we measured M^2-values of < 1.7 for the complete power range.

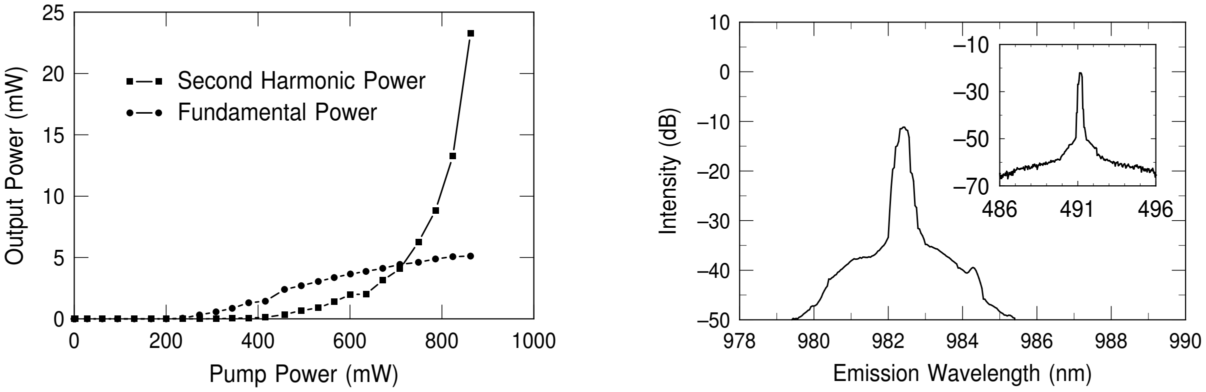

Fig. 2: Power characteristics and spectra of the second harmonic power and the transmitted fundamental power. As nonlinear optical crystal, LBO is used.

For 490 nm blue-green light generation, a 5 mm-long Type-I critically phase matched nonlinear Lithium Triborate crystal (LBO) and a mirror with a very high reflective dielectric coating for the fundamental wave is used. For the doubling process it is necessary to achieve and maintain laser operation in linear polarization. We have observed that the polarization of semiconductor disk lasers may change but can be affected by the external mirror adjustment. The optical power of the second harmonic generated (SHG) light has been measured to be 23 mW with an excellent beam quality factor M^2 of < 1.2.

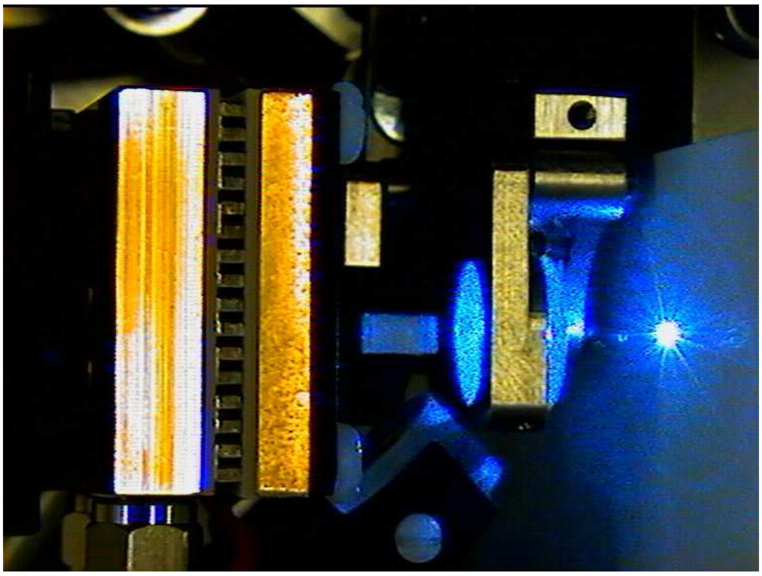

Fig. 3: Photograph of the frequency doubled semiconductor disk laser system in operation.

Figure 3 shows a photograph of the frequency doubled disk laser in operation. Thus, the optical-to-optical conversion efficiency can be calculated to be 2.7 %. The transmitted fundamental power of 5 mW indicates a fundamental intra-cavity power of about 3.3 W. Figure 2 shows the power characteristics of the second harmonic power and the transmitted fundamental power. The fundamental output power depends linearly on the pump power whereas the second harmonic power shows a quadratic dependency. The fundamental and second harmonic spectrum is shown on the right-hand side of Fig. 2 for the maximum output power. For this paper, a linear resonator configuration has been used. In this case, no focus is located in the external resonator. A location of a focus inside the crystal using a different resonator configuration would increase the optical power density and thus the doubling efficiency significantly. Moreover, the crystal length is not yet optimized.

5. Conclusion

An InAlGaAs semiconductor disk laser has been grown, processed, and characterized which shows a high beam quality ($M^2 < 1.7$) and high power ($P = 280\,\mathrm{mW}$) near-infrared ($\lambda \sim 982\,\mathrm{nm}$) laser output. Additionally, the 982 nm semiconductor disk laser radiation has been frequency doubled to produce 23 mW of coherent blue-green light (491 nm) with an exellent beam quality factor of $M^2 < 1.2$ by intra-cavity second harmonic generation (SHG) using critically phase matched Lithium Triborate (LBO).

References

[1] M. Kuznetsov, F. Hakimi, R. Sprague, and A. Mooradian, "Design and Characteristics of High-Power (> 0.5-W CW) Diode-Pumped Vertical-External-Cavity Surface-Emitting Semiconductor Lasers with Circular TEM_{00} Beams," *IEEE J. Select. Topics Quantum Electron.*, vol. 5, no. 3, pp. 561–573, 1999.

[2] C. Stewen, C. Contag, M. Larionov, A. Giesen, and H. Hügel, "A 1-kW CW thin disc laser," *IEEE J. Select. Topics Quantum Electron.*, vol. 6, no. 4, pp. 650–657, 2000.

[3] H. Unold, S. Mahmoud, R. Jäger, M. Kicherer, M. Riedl, and K. Ebeling, "Improving single-sode VCSEL performance by introducing a long monolithic cavity," *IEEE Photon. Technol. Lett.*, vol. 12, no. 8, pp. 939–941, 2000.

[4] A. Fischer, K. Choquette, W. Chow, A. Allermann, and K. Geib, "5.2 mW single-mode power from a coupled-resonator vertical-cavity Laser," in *IEEE LEOS 2000 Lasers and Electro-Optics Society, 13th Annual Meeting, Rio Grande, Puerto Rico*, pp. 802–803, 2000.

[5] M. Miller, M. Grabherr, R. King, R. Jäger, R. Michalzik, and K. Ebeling, "Improved output performance of high-power VCSELs," *IEEE J. Select. Topics Quantum Electron.*, vol. 7, no. 7, pp. 210–216, 2001.

[6] M. Sagawa, T. Toyonaka, K. Hiramoto, K. Shinoda, and K. Uomi, "High-power highly-reliable operation of 0.98-μm InGaAs-InGaP strain-compensated single-quantum-well Lasers with tensile-strained InGaAsP barriers," *IEEE J. Select. Topics Quantum Electron.*, vol. 1, no. 2, pp. 189–195, 1995.

[7] E. Schiehlen, M. Golling, and P. Unger, "Diode-pumped semiconductor disk laser with intra-cavity frequency doubling using lithium triborate (LBO)," *IEEE Photon. Technol. Lett.*, vol. 14, no. 6, pp. 777–779, 2002.

[8] M. Raya, S. Brueck, M. Osinski, C. Schaus, J. McInerney, and T. Brennan, "Resonant periodic gain surface-emitting semiconductor lasers," *IEEE J. Quantum Electron.*, vol. 25, no. 6, pp. 1500–1512, 1989.

[9] S. Corzine, R. Geels, J. Scott, R.-H. Yan, and L. Coldren, "Design of fabry-perot surface-emitting lasers with a periodic gain structure," *IEEE J. Quantum Electron.*, vol. 25, no. 6, pp. 1513–1524, 1989.

Vertical-Extended-Cavity Surface-Emitting Lasers

Ihab Kardosh and Vincent Voignier

We present first results on electrically pumped vertical-extended-cavity surface-emitting lasers (VECSELs). Experimental characterization of VECSELs with an external mirror and theoretical investigation of devices with an integrated on-substrate mirror are discussed.

1. Introduction

Applications like pumping of optical amplifiers or frequency doubling for visible laser light generation require high-power laser sources operating in a single transverse mode. Most efforts have concentrated on edge-emitting laser designs such as single-mode ridge waveguide lasers or broad-area lasers with various ways to overcome beam filamentation (e.g. master oscillator power amplifiers, unstable resonators).

However, in the past few years devices based on vertical-cavity surface-emitting laser (VCSEL) technology have appeared as a promising alternative to edge emitters. Since oxide-confined VCSEL emission becomes multimode when the active region diameter is larger than a few micrometers, their single-mode output power is restricted to a few mW [1]. The use of an external cavity defined by one distributed Bragg reflector (DBR) stack of the VCSEL chip and an external curved mirror allows to achieve lasing in a single optical mode with a beam diameter of tens of micrometers. Single-mode optical output powers of several hundreds of mW have been observed [2]. In the first part of this article, we describe the structure of an electrically pumped VECSEL and present our first characterization results.

An inherent drawback of external mirror VECSELs compared to usual VCSELs is given by the facts that they cannot be easily tested on chip level and that the formation of arrays is not possible. Furthermore, the alignment of the external mirror makes packaging a crucial step. One possibility to overcome this is to integrate the external mirror onto the substrate by using microlens technology [3, 4]. However, this comes with the penalty of reducing the optical mode diameter, thus reducing the output power. The second part of this report presents a feasibility study of VECSELs with on-chip integrated mirrors.

2. Device Structure and Principle of Operation

A VECSEL has a structure similar to that of a standard bottom-emitting VCSEL, as described in [5], except that it has a reduced n-DBR mirror stack. The main reason for using a bottom emitter (in which the output light is emitted through the substrate) for broad-area VCSELs is to obtain a uniform current distribution in the active region. A second advantage is the possibility to solder the device p-side down onto a heat sink, thus having the active region as close as possible to the heat sink. In the present devices, the n-DBR stack has only 14 layers, corresponding to a reflectivity of 97 %. Such a small reflectivity is not sufficient to observe lasing, i.e. the cavity defined by the p- and n-DBRs alone has a prohibitively high threshold gain. By placing an external mirror of adequate reflectivity in front of the output facet, thus feeding back laser emission into the active region, one obtains a three-mirror laser cavity whose threshold is much lower that of the solitary Fabry-Perot cavity. Thus for driving currents lying between these two threshold currents, only the optical modes of the three-mirror cavity will be lasing. Choosing a curved external mirror yields a stable cavity configuration and allows control of the transverse lasing mode.

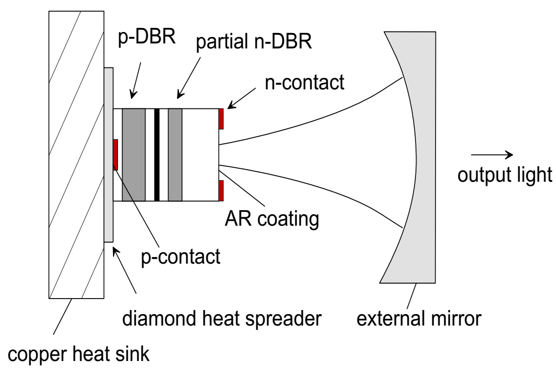

Fig. 1: Schematic drawing of the external mirror VECSEL. The chip is mounted p-side-down on a heat sink.

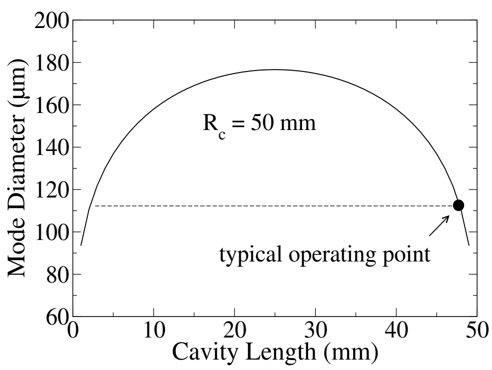

Fig. 2: Optical mode diameter in the active layer versus external cavity length for an external mirror with a radius of curvature of 50 mm. Typical operating cavity length is from 45 mm to 50 mm ($\lambda = 980$ nm).

Figure 1 shows a schematic drawing of the device. The VECSEL has no oxide aperture and is soldered p-side down onto a diamond heat spreader, which is attached to a copper heat sink. The diamond is metallized with AuSn solder. Soldering is achieved in a one-step heating process at a temperature of about 300 °C. The n-DBR selects a single longitudinal mode in the semiconductor cavity. Furthermore it confines most of the optical power density in the epitaxial layers, thus reducing the optical losses in the external cavity, namely the light absorption in the GaAs substrate. In order to avoid parasitic reflections from the substrate–air interface, a silicon nitride anti-reflection coating is deposited. Figure 2 shows the diameter $2w$ of an assumed Gaussian mode selected by the VECSEL for different external cavity lengths L_c and an external mirror radius of curvature of $R_c = 50$ mm.

The mode diameter is calculated from

$$w^2 = \frac{4\lambda L_c}{\pi}\sqrt{\frac{R_c - L_c}{L_c}}$$

with $\lambda = 980\,\mathrm{nm}$ and $R_c = 50\,\mathrm{mm}$.

3. Measurement Results

The results presented here have been obtained with a $125\,\mu\mathrm{m}$ p-contact diameter laser and an external mirror with $R_c = 50\,\mathrm{mm}$ and a reflectivity of 96 %. Figure 2 indicates a typical operating point. Lasing is observed for external cavity lengths ranging from 45 to 50 mm.

Figure 3 shows the L–I and I–V curves of the device in continuous waves (CW) operation. The threshold current is about 100 mA and the laser output power reaches a maximum of 6 mW at about 300 mA current, which is limited by thermal rollover. The optical spectrum in Fig. 3 shows a single laser line with a -10 dB width of about 0.09 nm for currents of roughly below 200 mA. For higher currents, the spectrum broadens with changes in modal structure and shifts toward longer wavelengths (thermally induced red-shift).

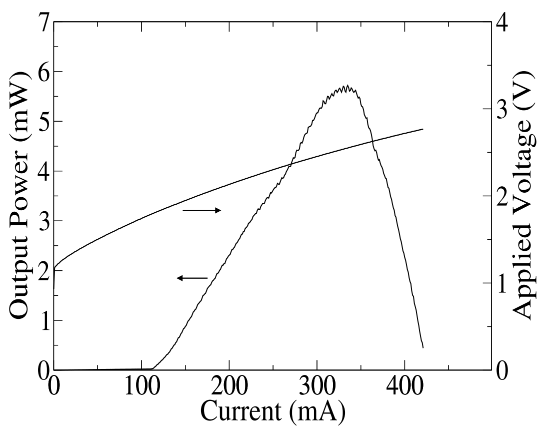

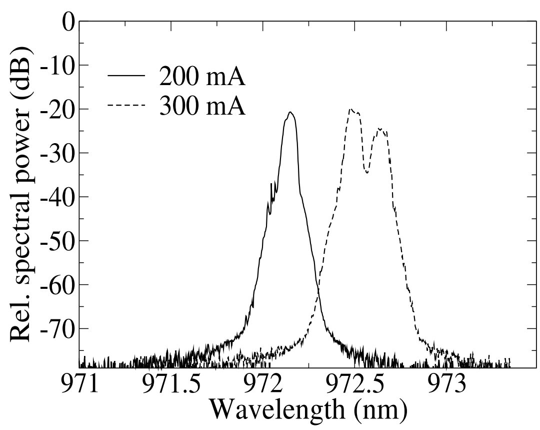

Fig. 3: *L–I–V* characteristics (left) and spectra for two driving currents (right) of a VECSEL with $125\,\mu\mathrm{m}$ p-contact diameter and 96 % external mirror reflectivity.

Since no oxide aperture is incorporated into the present design, current confinement is poor and efficiency is low. To get information about the epitaxial quality, we have processed standard broad-area VCSELs with the same fabrication procedure from epitaxial material with 21 instead of 14 n-DBR layer pairs. Much like the VECSELs before, these standard broad-area VCSELs exhibit poor output power, as can be seen in Fig. 4, which is also due to the lack of current confinement. This suggests that a next generation of devices with improved epitaxial quality and appropriate current confinement will show higher power output for the same geometry.

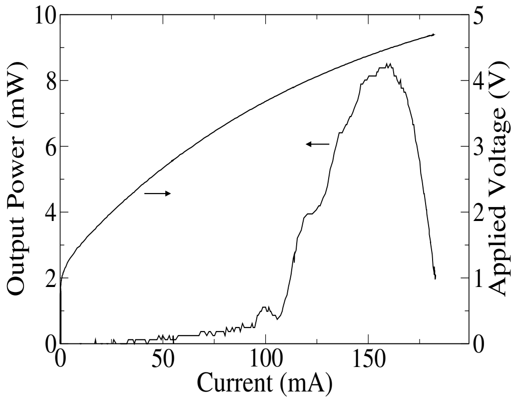

Fig. 4: *L–I–V* characteristics of a standard bottom-emitting VCSEL. The device is fabricated using epitaxial material similar to the VECSEL chip in Fig. 3, except for a higher number of 21 n-DBR layer pairs. The p-contact is 30 μm wide.

4. Design and Fabrication of Integrated External Mirrors

As a great advantage, the design presented above allows lasing in a broad (typically 100 μm) single transverse mode. However, the drawback of using an external mirror is the precise alignment required, which is a challenge for device packaging in view of large scale production.

The need for alignment during characterization or packaging can be eliminated if the mirror is integrated onto the substrate during fabrication. In what follows we present some preliminary tests and calculations relevant for the fabrication of such a VECSEL.

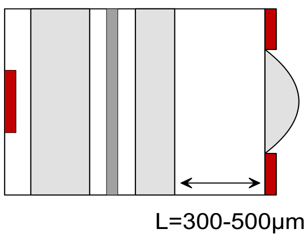

Fig. 5: Schematic drawing of an integrated mirror VECSEL device. Substrate thickness varies from 300 μm to 500 μm and defines the external cavity length.

Figure 5 illustrates a VECSEL chip with integrated micromirror. The mirror is fabricated using a technology developed for the realization of microlenses [6]. Photoresist is patterned into disks using a two-step lithographical process. As illustrated in Fig. 6, this is followed by a reflow process transforming the disks into lenses. The radius of curvature of the final lens depends on the diameter and the height of the initial disk.

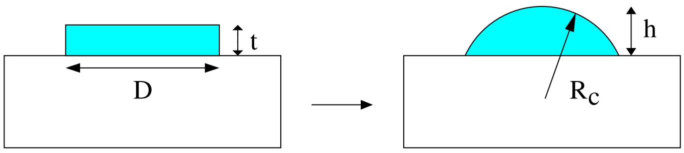

Fig. 6: Microlens fabrication using a reflow process. A patterned photoresist disk (diameter D, thickness t) takes a spherical lens shape (height h, radius of curvature R_c) after reflow.

We assume that the photoresist volume does not change during reflow. In this case the radius of curvature R_c can be expressed in terms of h and D by basic geometrical considerations as

$$R_c = \frac{h^2 + (D/2)^2}{2h} \ .$$

Experimentally, radii of curvature of a few millimeter can be achieved. Figure 7 shows a comparison between the calculation and fabricated lenses, where the differences arise from the fact that the lenses are not perfectly spherical in shape. Furthermore, fabrication of lenses with a large radius of curvature is limited by the effect that the photoresist takes a concave shape in its center when the diameter of the disk is too large or its thickness too small, as seen in Fig. 8.

Since the refractive index n_l of the photoresist used for the lens is different from the index of the substrate n_s (1.5 compared to 3.5), the effective radius of curvature to be considered to calculate the optical mode diameter is $n_s R_c / n_l$. Figure 9 shows the dependence of the mode diameter on the effective radius of curvature of the mirror for different substrate thicknesses.

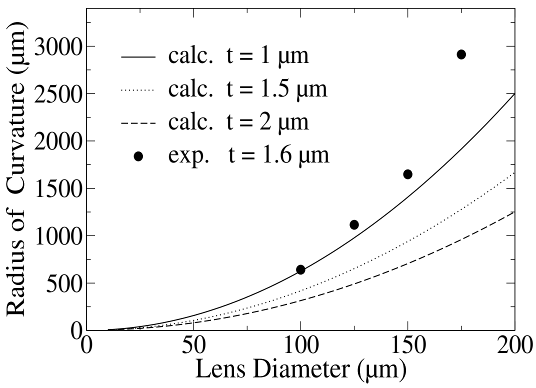

Fig. 7: Calculation and experimental results for the radius of curvature R_c as a function of lens diameter D for different photoresist thicknesses t.

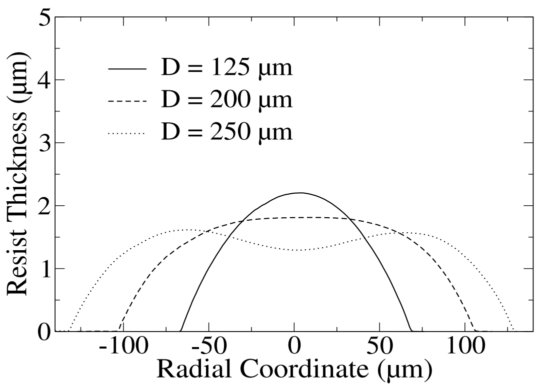

Fig. 8: Measured lens profiles for different lens diameters. For large lens diameters the radius of curvature becomes negative.

The external cavity length is fixed by the substrate thickness. Figure 9 shows that the optical mode diameter, considering the achievable effective radius of curvature, lies in the range of 20 to 25 μm.

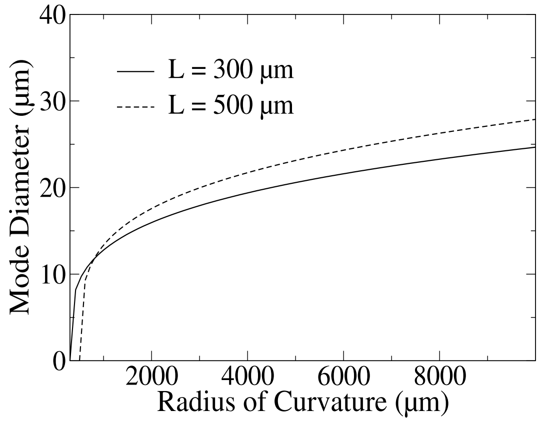

Fig. 9: Mode diameter versus effective radius of curvature for different substrate thicknesses L.

The microlens is later to be covered with a high reflectivity coating to form the external mirror. A simple calculation allows the estimation of the coating reflectivity needed. The three-mirror cavity is, for the purpose of the threshold current calculation, equivalent to a two-mirror cavity, one with the p-DBR reflectivity, and one with an effective reflectivity R_{eff} given by

$$R_{\text{eff}} = \left(\sqrt{R_{\text{n}}} + \frac{T_{\text{n}}\sqrt{R_{\text{ext}}}}{1 + \sqrt{R_{\text{n}} R_{\text{ext}}}} \right)^2$$

with R_{n} and R_{ext} as the reflectivities of the n-DBR and the external mirror, respectively, and T_{n} as the intensity transmission coefficient of the n-DBR. This relationship is plotted in Fig. 10.

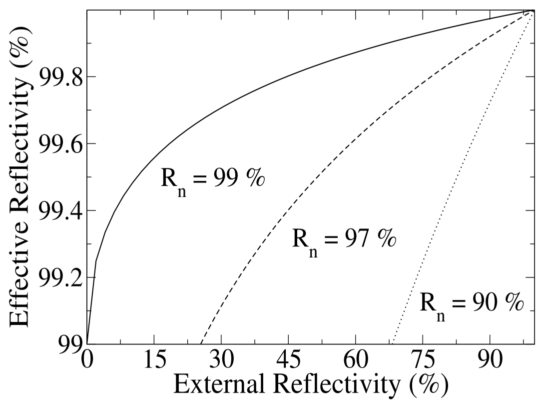

Fig. 10: Effective reflectivity of the extended cavity as a function of the external mirror reflectivity for different lossless n-DBRs with reflectivities R_{n}.

As can be seen, for a required reflectivity $R_{\text{eff}} = 99.6\,\%$ and $R_{\text{n}} = 90\,\%$ for the built-in n-DBR, an external mirror with $R_{\text{ext}} = 86\,\%$ is required, where a lossless n-DBR has been assumed.

5. Conclusion

We have fabricated and characterized electrically pumped VECSELs operating in continuous wave. The devices deliver single-mode output powers of about 3 mW and maximum output powers of about 6 mW. Relatively low power and efficiency are due to the lack of current confinement. Preliminary theoretical investigations of integrated mirrors for monolithic devices are presented and show that a single transverse optical mode of 20 to 25 μm diameter can be achieved.

References

[1] H.J. Unold, W.Z. Mahmoud, R. Jäger, M. Grabherr, R. Michalzik, and K.J. Ebeling, "Large-area single-mode VCSELs and the self-aligned surface relief," *IEEE J. Sel. Top. Quantum Electron.*, vol. 7, no. 2, pp. 386–392, 2001.

[2] M. Kuznetsov, F. Hakimi, R. Sprague, and A. Mooradian, "Design and characteristics of high-power (>0.5-W CW) diode-pumped vertical-external-cavity surface-emitting semiconductor lasers with circular TEM_{00} beam," *IEEE J. Sel. Top. Quantum Electron.*, vol. 5, no. 3, pp. 561–573, 1999.

[3] F. Nikolajeff, T.A. Ballen, J.R. Leger, A. Gopinath, T.-C. Lee, and R.C. Williams, "Spatial-mode control of vertical-cavity lasers with micromirrors fabricated and replicated in semiconductor materials," *Appl. Optics*, vol. 38, no. 14, pp. 3030–3038, 1999.

[4] K.S. Kim, Y.H. Lee, B.Y. Jung, and C.K. Hwangbo, "Single mode operation of a curved-mirror vertical-emitting laser with an active distributed Bragg reflector," *Jap. J. Appl. Phys.*, vol. 41, no. 7B, pp. L827–L829, 2002.

[5] M. Miller, M. Grabherr, R. King, R. Jäger, R. Michalzik, and K.J. Ebeling, "Improved output performance of high-power VCSELs," *IEEE J. Sel. Top. Quantum Electron.*, vol. 7, no. 2, pp. 210–216, 2001.

[6] Sinzinger and Jahns, *Microoptics*, ch. 4. Weinheim: WILEY-VCH, 1999.

Polarization-Stable Elliptically Surface-Etched VCSELs

Heiko J. Unold

1. Introduction

With conventional oxidized vertical cavity surface-emitting lasers (VCSELs) firmly established in the datacom market, more and more smaller-volume applications are beginning to crop up where these inexpensive and versatile devices are considered as alternatives to LEDs or edge-emitting lasers. However, both for datacom and many of the new applications, emission in one single transverse mode and polarization can be crucial for the performance, e. g. when polarization-dependent elements are present in the system setup. In order to meet this demand for advanced VCSELs, solutions need to be found which provide reliable single-polarization emission in combination with simple practical fabrication techniques.

2. Device Fabrication

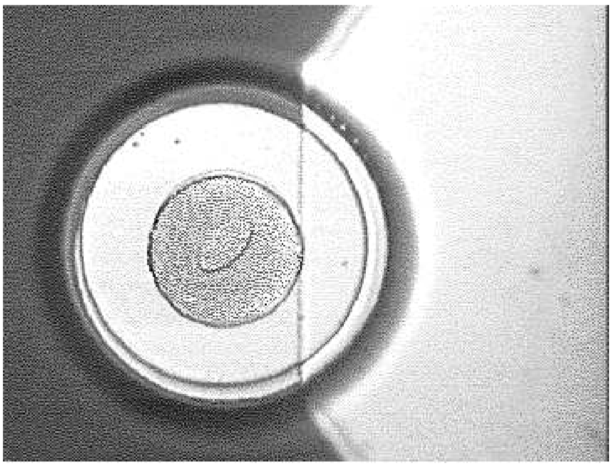

Fig. 1: Top-view photograph of a self-aligned elliptically surface-etched VCSEL. Ellipse size is $3.2 \times 6.4\,\mu$m.

Self-aligned surface etching has already been shown to provide strong mode control [1] and the possibility of influencing the polarization direction of the emitted light [2] while requiring only one simple additional processing step. A top-view photograph of such an elliptically surface-etched device is shown in Fig. 1. Any standard VCSEL layer structure can be used for this process, although increased freedom is provided in the choice of etch depth if an additional low-aluminum content $\lambda/2$-layer is added on top of the structure. We employ an 850 nm-wavelength structure using three 8 nm GaAs quantum wells embedded in $Al_{.25}Ga_{.75}As$, $Al_{.9}Ga_{.1}As/Al_{.15}Ga_{.85}As$-mirrors with 34.5 n-doped pairs and 27 p-pairs including an $Al_{.98}Ga_{.02}As$ oxide aperture in the field null above the active region. In the processing, the surface etch shape is defined in a first lithography step which simultaneously defines the device mesa and thus the alignment to the oxide aperture formed later. Surface etching is done wet chemically to a depth of about $\lambda/4$ with an accuracy in the nm-range and good homogeneity. Different aspect ratios and orientations of the ellipses as well as mesa diameters are provided on the mask in order to extract the influence of these parameters on the polarization behavior.

3. Measurements and Modeling

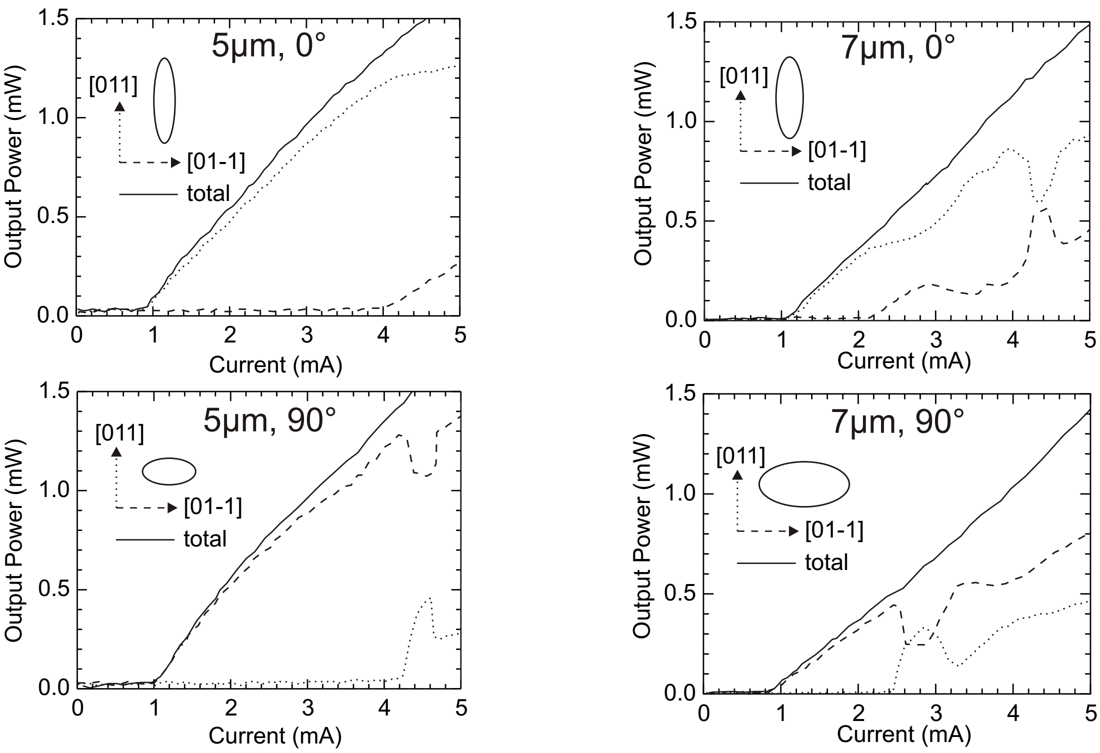

Fig. 2: Polarization-resolved LIV-characteristics of 0 and 90°-etched 5 and 7 μm-devices, insets illustrating orientation and dimensions of the etched ellipses.

Figures 2 and 3 display the influence of the fabrication parameters on polarization, measured cw at room temperature; the best effect is achieved for 5 and 7 μm-diameter oxide aperture devices depicted in these figures. All of the ellipse aspect ratios investigated with values between 0.25 and 0.5 achieve polarization pinning along the major ellipse axis as long as the ellipses are aligned along one of the major crystal axes. Unetched reference devices only maintain single-mode emission for a very small current range and thus possess no significant polarization preference. Etch ellipses oriented at 45° angles provide single-mode ranges comparable to the ones aligned to the crystal axes, but the polarization state of the fundamental mode tends to switch within this range. Detailed oxide aperture shape measurements reveal that especially for small devices, oblong diamond-shapes are formed due to a slightly anisotropic oxidation process. The deviations from the crystal axes in Fig. 3 can therefore be explained by additional small nonuniformities in oxidation. For simulation, we employ a fully vectorial model [3] taking both oxide shape and surface etch ellipse into account by coupled-mode theory. Figure 4 shows that both dichroism and birefringence are influenced such that the polarization along the major ellipse axis is preferred, dichroism obviously having much stronger impact.

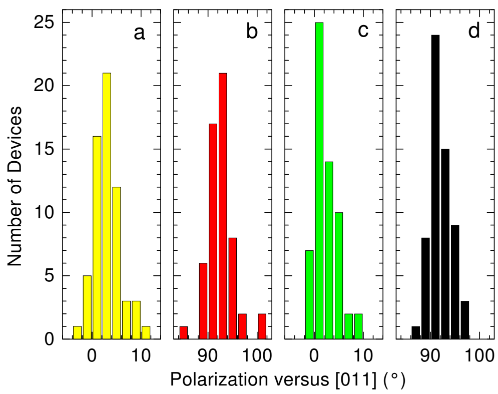

Fig. 3: Polarization angle histogram for about 60 devices each of 0 and 90°-etched 5 μm-devices (a and b) and 7 μm-devices (c and d).

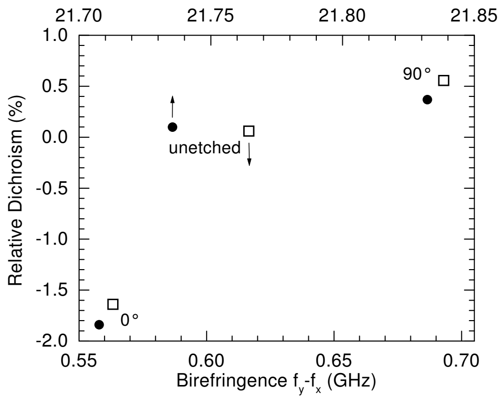

Fig. 4: Simulated dichroism versus birefringence for an unetched and 0 and 90°-etched 5 μm-devices with (top axis, circles) and without electro-optic effect (bottom axis, squares).

4. Conclusion

We have successfully fabricated and modeled elliptically surface-etched oxide-confined VCSELs for high single-mode polarization-stable operation. From our results, the two possible polarization directions seem to be determined by anisotropies in the oxidation process but can be selected by the orientation of the etched ellipse. Investigations with different mirror reflectivities and more finely varied ellipse shapes will lead to design rules for optimum performance.

References

[1] H.J. Unold, S.W.Z. Mahmoud, R. Jäger, M. Grabherr, R. Michalzik, and K.J. Ebeling, "Large-area single-mode VCSELs and the self-aligned surface relief," *IEEE J. Select. Topics Quantum Electron.*, vol. 7, pp. 386–392, 2001.

[2] H.J. Unold, M.C. Riedl, R. Michalzik, and K.J. Ebeling, "Polarization control in VCSELs by elliptic surface etching," *Electron. Lett.*, vol. 38, pp. 77–78, 2002.

[3] P. Debernardi, G.P. Bava, C. Degen, I. Fischer, and W. Elsäßer, "Influence of Anisotropies on Transverse Modes in Oxide-Confined VCSELs," *IEEE J. Quantum Electron.*, vol. 38, no. 1, pp. 73–84, 2002.

Bistability in Bipolar Cascade VCSELs

Thomas Knödl

Measurement results on the formation of bistability loops in the light versus current and current versus voltage characteristics of two-stage bipolar cascade VCSELs are presented. It is observed that the bistable behavior is the more pronounced the more the cavity resonance is blue-shifted with respect to the gain maximum of the quantum wells. Additionally, the slope efficiency increases by more than a factor of 1.5 compared to conventional VCSELs due to carrier recycling.

1. Introduction

Bistability in vertical-cavity surface-emitting lasers (VCSELs) offers attractive applications in the area of high density optical memory and signal processing such as optical switching. Several mechanisms have been reported which favor bistable output behavior in VCSELs, such as polarization state changes [1], [2], index variations under optical injection [3], [4], transverse mode hopping [5], and saturable absorption [5], [6], [7]. For the first time to our knowledge, in this article, measurement results are reported on the bistable behavior of bipolar cascade VCSELs, exploiting the saturable absorption effect. Bipolar cascade VCSELs, in general, have been successfully demonstrated to overcome the bottleneck of limited roundtrip gain in vertical laser resonators due to carrier recycling [8]. However, since the active regions in cascade lasers are electrically coupled, current spreading in the cavity leads to non-homogeneously pumped stages which can favor bistable behavior. It is observed that bistability loops continuously expand with increased detuning between cavity resonance and gain maximum.

2. Device Structure

Figure 1 shows a schematic cross-section of an investigated selectively oxidized two-stage bipolar cascade VCSEL grown by molecular beam epitaxy (MBE).

The design consists of two densely stacked active pn-junctions, each of which comprises three undoped 8 nm thick $In_{0.2}Ga_{0.8}As$ quantum wells separated by 10 nm thick GaAs barriers. Both active regions are placed in the antinodes of the standing wave pattern and are electrically coupled by a highly doped reverse-biased GaAs tunnel junction in between. The p-type top and n-type bottom Bragg reflector stacks consist of 19 and 32.5 $Al_{0.9}Ga_{0.1}As$/GaAs layer pairs, respectively. Current confinement is achieved by mesa

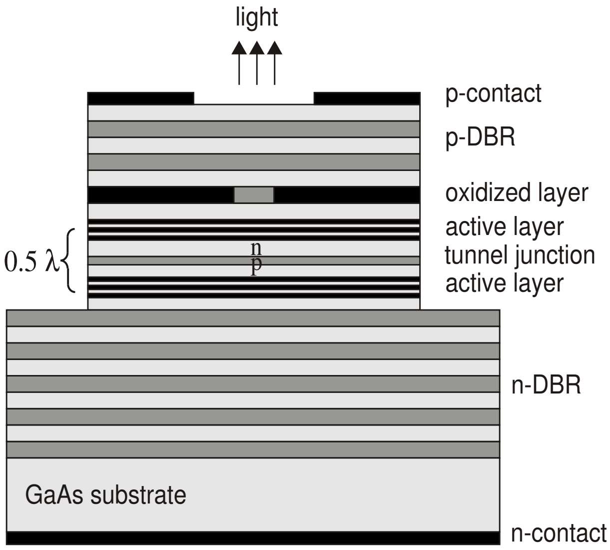

Fig. 1: Schematic cross-section of a fabricated two-stage bipolar cascade VCSEL.

etching and subsequent selective oxidation of a 30 nm thick AlAs layer incorporated in the node of the standing wave pattern above the upper active region. For the p- and n-type doping we use C and Si, respectively. Finally, a ring contact deposited on the mesa allows for top surface emission.

3. Experimental Results

For research purposes we have chosen a substrate position in the MBE chamber which yields a strong gradient in layer thicknesses and therefore a shift of the cavity resonance of almost 80 nm between the center and edge of a two-inch wafer. The gain maximum, on the other hand, shifts only by about 3 nm as measured from edge-emitting lasers fabricated from the VCSEL material. Thus, such a wafer allows to investigate the device performance with respect to the detuning between cavity resonance and gain maximum. The oxide aperture of the devices under test is about 3 to 4 μm in diameter, resulting in single-mode emission. All presented measurement data are obtained from continuous wave operation at room temperature.

Figure 2 shows light versus current (L–I) characteristics of two-stage cascade VCSELs with different emission wavelengths. The lasers are driven in 1 μA steps by a precision current source which also monitors the voltage. It is clearly seen that bistable behavior is more and more pronounced in shorter wavelength devices, where no hysteresis loops are found at wavelengths longer than 980 nm. The observed hysteresis width ranges up to about 0.57 mA in current with an optical power discontinuity of more than 960 μW at the turn-on switching point at 938 nm wavelength. This bistable behavior can be explained by the wavelength and carrier density dependent absorption coefficient of the active stages. Firstly, due to only one oxide aperture, current spreading is present in the

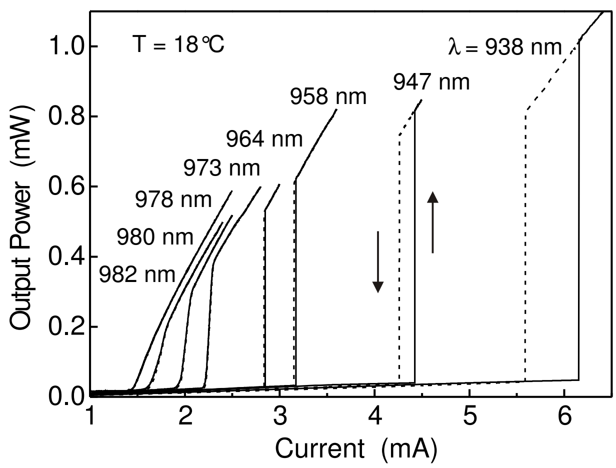

Fig. 2: Emission wavelength dependent formation of *L–I* bistability loops. The gain maximum is fixed at about 973 nm.

cavity which leads to a reduced carrier density in the bottom compared to the top stage. Thus, the bottom active region acts like a tunable absorber in the first place. Secondly, the wavelength dependent absorption coefficient decreases with longer wavelength, in particular at the long wavelength side of the gain maximum ($\lambda \geq 973$ nm here), which explains the disappearance of bistability.

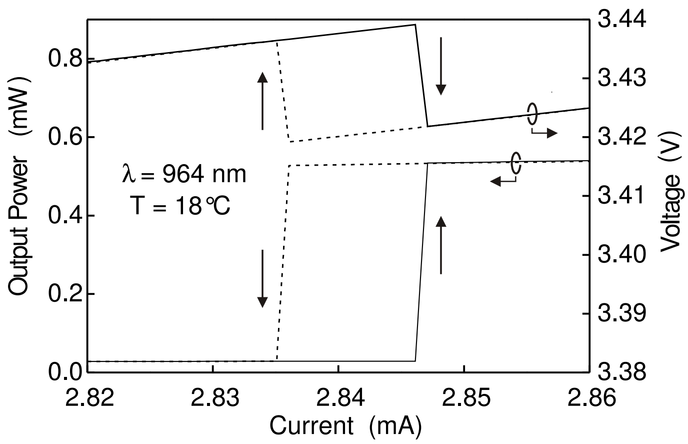

Fig. 3: Bistable *L–I* and *I–V* characteristics of the 964 nm wavelength bipolar cascade VCSEL from Fig. 2.

All optical bistability loops shown in Fig. 2 are accompanied by a corresponding hysteresis in the current versus voltage (I–V) characteristic. This observation is explicitly shown in Fig. 3 for the device emitting at 964 nm wavelength. Here, the hysteresis width and output power discontinuity are 11 μA and 510 μW, respectively. The corresponding voltage discontinuity of about 17 mV occurs at the switching points and can be explained by the sudden change in carrier density in the active regions due to the abrupt optical turn-on and turn-off behavior.

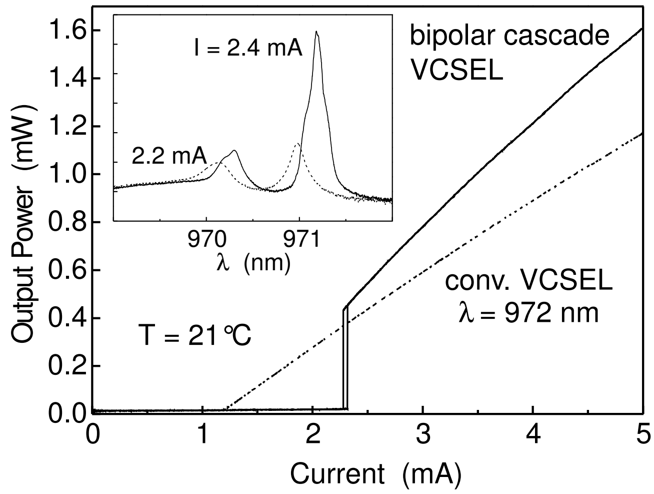

Fig. 4: *L–I* characteristic of a conventional VCSEL and of a two-stage cascade device at 972 nm wavelength. The inset shows the spectra of the cascade VCSEL around the bistability point on a 70 dB vertical scale.

As a direct effect of carrier recycling the investigated single-mode cascade devices exhibit slope efficiencies of about 33 to 38 % that are significantly higher than those measured for conventional one-stage reference VCSELs (21 to 23 %). For comparison, Fig. 4 shows the typical *L–I* characteristic of a conventional one-stage VCSEL and of a two-stage bipolar cascade VCSEL at about 972 nm emission wavelength. The increase in differential quantum efficiency indicates that both active regions in the cascade VCSELs contribute to lasing. Thus, the presented design can combine bistability and increased roundtrip gain.

4. Conclusion

We have presented data on bipolar cascade VCSELs which exhibit optical and electrical bistability loops due to saturable absorption. The bistability strongly depends on the detuning between resonance wavelength and gain maximum that is attributed to the wavelength and carrier density dependent absorption coefficient. Moreover, the presented cascade VCSELs also provide additional roundtrip gain compared to conventional one-stage lasers. Therefore, applications such as optical switching and optical memory may also arise for bipolar cascade VCSELs. In future, we will investigate the bistability loops with respect to temperature as well as cascade VCSEL design variations.

References

[1] Z.G. Pan, S. Jiang, M. Dagenais, R.A. Morgan, K. Kojima, M.T. Asom, R.E. Leibenguth, G.D. Guth, and M.W. Focht, "Optical injection induced polarization bistability in vertical-cavity surface-emitting lasers," *Appl. Phys. Lett.*, vol. 63, no. 22, pp. 2999–3001, 1993.

[2] H. Kawaguchi, I.S. Hidayat, Y. Takahashi, and Y. Yamayoshi, "Pitchfork bifurcation polarisation bistability in vertical-cavity surface-emitting lasers," *Electron. Lett.*, vol. 31, no. 2, pp. 109–111, 1995.

[3] F. Jeannés, G. Patriarche, R. Azoulay, A. Ougazzaden, J. Landreau, and J.L. Oúdar, "Submilliwatt optical bistability in wafer fused vertical cavity at 1.55 μm wavelength," *IEEE Photon. Technol. Lett.*, vol. 8, no. 4, pp. 539–541, 1996.

[4] M.J. Bohn and J.G. McInerney, "Bistable output of an optically pumped vertical-cavity surface-emitting laser," *J. Opt. Soc. Am. B*, vol. 14, no. 12, pp. 3430–3436, 1997.

[5] X. Tang, J.P. van der Ziel, B. Chang, R. Johnson, and J.A. Tatum, "Observation of bistability in GaAs quantum-well vertical-cavity surface-emitting lasers," *IEEE J. Quantum Electron.*, vol. 33, no. 6, pp. 927–932, 1997.

[6] S.F. Lim, J.A. Hudgings, G.S. Li, W. Yuen, K.Y. Lau, and C.J. Chang-Hasnain, "Self-pulsating and bistable VCSEL with controllable intracavity quantum-well saturable absorber," *Electron. Lett.*, vol. 33, no. 20, pp. 1708–1710, 1997.

[7] A.J. Fischer, K.D. Choquette, W.W. Chow, A.A. Allerman, and K.M. Geib, "Bistable output from a coupled-resonator vertical-cavity laser diode," *Appl. Phys. Lett.*, vol. 77, no. 21, pp. 3319–3321, 2000.

[8] T. Knödl, A. Straub, M. Golling, R. Michalzik, and K.J. Ebeling, "Scaling behavior of bipolar cascade VCSELs," *IEEE Photon. Technol. Lett.*, vol. 13, no. 9, pp. 930–932, 2001.

Flip-Chip Integration of 2-D 850 nm Backside Emitting Vertical Cavity Laser Diode Arrays

Hendrik Roscher

Two-dimensional (2-D) arrays of 850 nm substrate side emitting oxide-confined vertical-cavity lasers are fabricated at a 250 µm pitch. They are designed to provide high frequency modulation capability targeting serial data rates of up to 10 Gbit/s. The arrays are directly hybridized onto silicon fanouts by means of an indium solder bump flip-chip technology. Coplanar transmission lines provided on the fanouts allow for individual addressing of each of the array's elements. The performance of assembled 8 × 8 laser modules is demonstrated by their basic electro-optical and thermal characteristics.

1. Introduction

While the TMT (Telecommunications, Media and Technology) sectors are severely affected by the current economic slump, bandwidth-hungry applications such as streaming video, e-commerce, and so on still hold the promise of lasting strong profit margins. Therefore, further escalating data traffic levels are predicted. Optical networking will eventually be the only feasible solution to support this continuous growth of data rates well into the future. The increase in throughput of the fiber-equipped long-haul backbones has shifted the bandwidth bottleneck upstream, i.e. deeper into the network. There, in the central offices, the limitations of electrical interconnects create the demand for ultra dense, high data rate, power and cost efficient short-reach optical interconnects between routers and switches in major hubs, and all the way down to the inter-board, inter-chip and even intra-chip levels. Since the component count soars the deeper the penetration into the network is, inexpensive and easily manufactured optical devices are required.

Vertical-cavity surface-emitting lasers (VCSELs), due to their surface-normal light emission, lend themselves to the design of massively parallel optical transmitters implemented as two-dimensional array configurations. Due to their silicon IC compatible low-cost wafer scale manufacturing and testing, VCSELs have the potential to significantly reduce the cost of active optical network components. The circular low divergence output beam shape facilitates light launching to optical interfaces without the need for complicated optics. High power conversion efficiencies complement other integration-friendly properties of high-performance VCSELs and lead to reduced heating in densely packed transceiver modules. In consequence, 2-D VCSEL arrays enable network equipment designers to consolidate and save space, while making their infrastructure as high-performance and cost-efficient as possible.

In this report, 2-D optical high-speed transmit modules for multimode fiber based short haul links are presented. Fabrication details are given and basic characterization of the finished modules is provided in terms of their electrical and optical properties as well as the heat management of the assembly.

2. Device Structure and Fabrication

Oxide-confined VCSEL arrays with backside emission at the standardized 850 nm wavelength are implemented in a flip-chip ready configuration. In a real world application, these would typically be hybridized to an ASIC driver chip performing the required logic functions. In this work, the carrier substrate is a silicon fanout on which low loss coplanar transmission lines serve to separately address the individual devices with high frequency signals. The VCSEL arrays are directly attached to the fanouts by indium solder bump bonding. This technology provides high-speed, high signal integrity (e.g. low parasitics) electrical interfaces potentially supporting serial data rates up to 10 Gbit/s.

2.1 Flip-chip ready VCSEL arrays and the silicon fanout

The schematic cross section of Fig. 1 represents one unit cell of the emitter arrays. The two storied wet etched mesa is the actual laser. It is a generic VCSEL structure made up of three active quantum wells sandwiched between top and bottom Bragg stacks. Lateral current and optical confinement is achieved by selective wet oxidation of a 30 nm thick AlAs film inserted in the first quarter wavelength layer above the p-type cladding of the inner cavity.

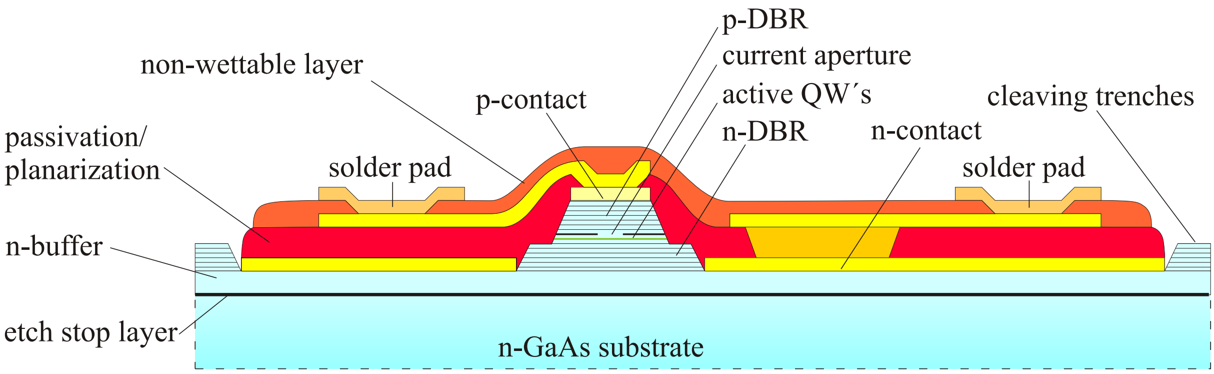

Fig. 1: Schematic cross section of one array unit cell depicting the flip-chip ready VCSEL design. The cleaving trenches around each cell allow the finished VCSEL wafer to be diced into any desired array size. The array dimensions are therefore not predetermined by the layout.

Since light emission is through the n-mirror, the current can be injected through a full size Ti/Pt/Au metalization covering the entire contact area of the p-mesa where low mobility hole conduction prevails. Flip-chip bonding requires the n-contact to be fabricated on the top side as well. Ge/Au/Ni/Au metalization surrounding the mesa ensures a low resistance contact to the highly n-doped $3\,\mu$m thick AlGaAs buffer layer through which electrons are laterally fed to the active region. In this flip-chip ready design, n- and p-solder pads are formed at the same elevation, on top of the polyimide passivation. Lateral transmission lines connect these bond pads to their respective VCSEL contacts. This necessitates an additional polyimide non-wettable layer which restricts the solder flow to the circular pads during the subsequent flip-chip bonding process.

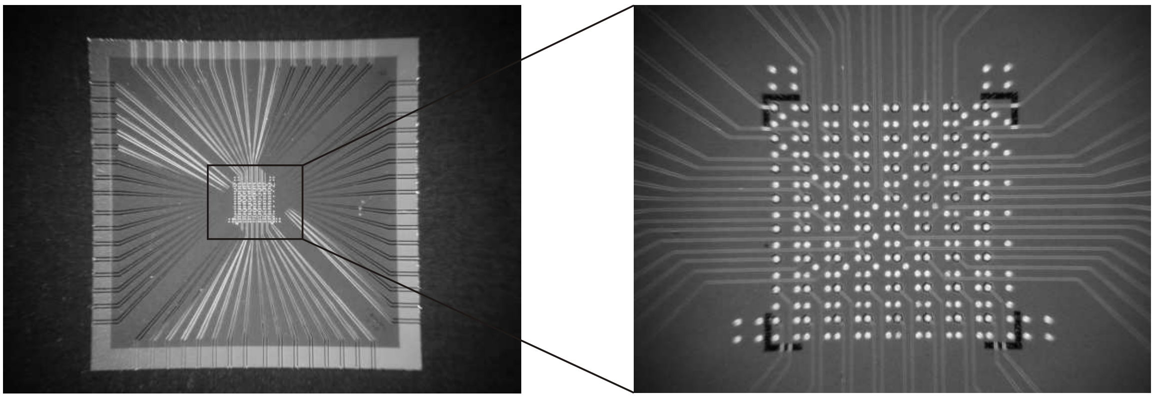

Fig. 2: *Left:* $15\times15\,\mathrm{mm}^2$ silicon fanout on which $50\,\Omega$ coplanar transmission lines allow separate addressing of the individual devices in the array with high-frequency signals. *Right:* closeup of the center region showing the solder pad configuration.

The photographs of Fig. 2 show the silicon fanout to which 8×8 VCSEL arrays can be hybridized. The 64 coplanar transmission lines of $50\,\Omega$ characteristic impedance, defined by standard lithography and lift-off, are used for high-frequency signal transmission. A 250 nm thick intermediate dielectric (SiO_2) on top of the semi-insulating silicon substrate minimizes otherwise noticeable leakage currents. Just like on the VCSEL chip, a polyimide protective coating is applied to most of the subcarrier's top surface. Its primary function is, however, the confinement of the indium solder to the bond pads during reflow in the center region. Low-loss contacts can be established to the transmission lines around the circumference of the $15 \times 15\,\mathrm{mm}^2$ chip using commercial microwave probe heads. Thick electroplated nickel was used for the bond pads since it is an effective diffusion barrier for the indium solder, and is also well wettable by it. Every 4 of these pads belong to one cell since multiple n-contacts have been implemented in an effort to promote heat transport away from the active device. As is visible in the right part of Fig. 2, there are elbow marks aiding coarse pre-alignment and pads for monitor bumps in every corner.

2.2 Flip-chip joining and final preparation

The indium bumps can be formed on either of the two substrates to be flip-chip joined. Solder deposition by evaporation offers, in contrast to electroplating, better height control as well as the additional degree of freedom to vary the bump sizes, if needed, by utilizing more or less of the area between the bond pads. The bonding process proved to be simple and reliable since, the solder being a pure metal, no alloy related problems like decomposition leading to brittle high resistivity connections can occur.

The pre-alignment of the approximately $2\times2\,\mathrm{mm}^2$ laser chip to the fanout is done manually by coarsely placing it face down on the bumps and then pushing it to a pre-aligned position under a microscope. During the high-temperature bonding process, the restoring force exerted by the surface tension of the molten solder moves the VCSEL array into a nearly perfectly aligned position. This self-alignment mechanism, which starts working once the indium wets the bond pads, was found to be a useful indicator for the establishment of the bonds. Up to 100 % bonding yield is achieved with the method described. Figure 3 displays a VCSEL array bonded to a fanout chip. The state shown is prior to underfill injection, and, therefore, the GaAs substrate is not yet removed.

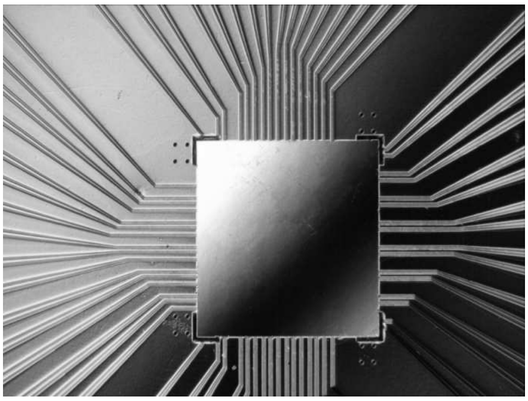

Fig. 3: Flip-chip bonded VCSEL array prior to underfill injection and substrate removal. It is aligned to the elbows on the fanout by the restoring force of the molten solder.

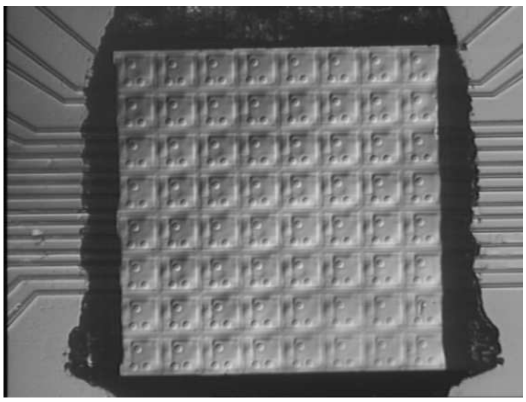

Fig. 4: Completed 64 channel transmit module. All that remains of the VCSEL wafer is a fragile sheet of epitaxial layers of $3\,\mu$m thickness, except for the thicker mesas.

After the two substrates are flip-chip joined, the gap between them is filled with an epoxy adhesive to provide environmental protection and mechanical stability to the module. Reliability is improved this way by reducing the thermal stresses imposed on the solder joints and thus mitigating creep and whisker growth, the two problems frequently associated with indium solder.

For the light generated in the GaAs active region of the bottom-emitting VCSELs to be able to actually escape, the GaAs substrate, which is highly absorptive at the operating wavelength, has to be removed before the module can be put to use. GaAs substrate removal is done successively in the course of the fabrication. The VCSEL wafer is pre-thinned down to 200 μm by chemical mechanical polishing before the arrays are singularized and flip-chip bonded. However, the substrate cannot be fully taken off until the module is stabilized by the underfill. The remainder of the substrate is removed with a selective spray etch process that stops at the etch stop layer (ref. to Fig. 1). Finally, this etch stop layer is wet chemically removed. The result, a completed 64-channel transmit module, is presented in Fig. 4. The $2 \times 2\,\mathrm{mm}^2$ VCSEL chip is thinned down to a sheet of only 3 μm thickness. All that remains of the VCSEL wafer are the epitaxial layers. Due to partial transparency, the bottom surface is visible and each $250 \times 250\,\mu\mathrm{m}^2$ VCSEL cell in the array can be distinguished. The dark frame surrounding the array is the cured underfill.

3. Basic Characteristics

A complete LIV (optical output power, driving current and voltage) characterization was done for all channels of a finished module. The results are shown in Fig. 5. The basic VCSEL performance as well as array homogeneity can be accordingly assessed. Lasing of the 10 μm current aperture devices sets in consistently at 1 mA and 1.8 V. An optical output power of 1 mW is reached at 2.7 mA and 1.9 V. The curves exhibit rather good homogeneity except for the one outlier with substantially enhanced output power for unclear reasons. The shorted VCSEL could well be caused by faulty transmission lines on this particular early fabricated fanout chip.

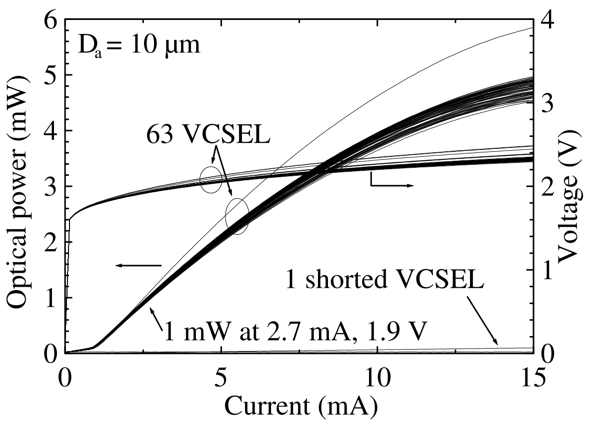

Fig. 5: VCSEL cw operation characteristics of all 64 channels of a finished module.

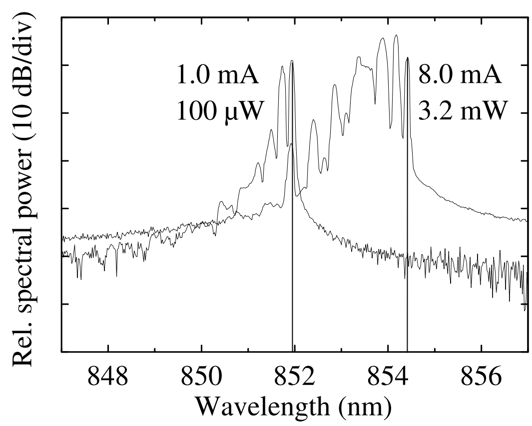

Fig. 6: Optical spectra of one of the VCSELs at two different operating points.

The exemplary spectra of Fig. 6 at two different operating points as indicated in the graph reveal a pronounced red-shift. It corresponds to a thermal resistance of about 2.6 K/mW. Hence, the devices heat up significantly at higher driving currents. This is partly responsible for the low value of the differential resistance of about 25 Ω. Thermal emission of charge carriers across the heterojunctions in the mirrors account for a large portion of the thermal resistance, which is enhanced at elevated temperatures. However, higher operating temperatures are in general detrimental to the long-term reliability of the devices.

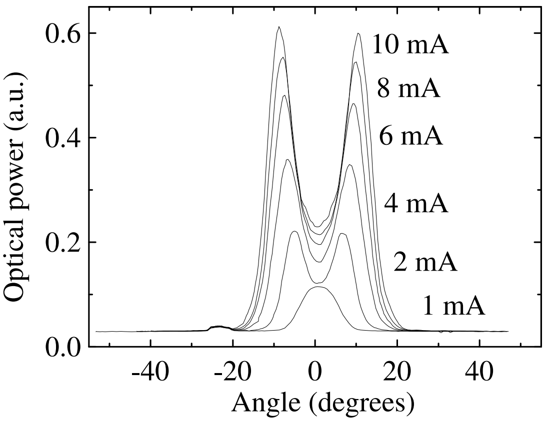

Fig. 7: Typical far-field intensity distributions at different operating currents.

Typical far-fields at different operating currents are given in Fig. 7. Owing to the position of the oxide layer within the p-mirror, the mode pattern experiences strong index guiding. As a result, many higher order transverse modes can oscillate simultaneously (as is evident in Fig. 6). The sheet resistance of the n-buffer layer leads to current crowding near the edge of the oxide aperture. This enhances the effect of spatial hole burning and favors those higher order modes as they better overlap with the lateral gain profile. They therefore take over at higher currents. The result is a donut-like intensity distribution particularly at higher currents which, in conjunction with a relatively large divergence angle of about $25\,^\circ$ (FWHM), complicates light coupling to fibers.

4. Conclusion

64-channel optical transmit modules were successfully fabricated by hybridizing 8×8 VCSEL arrays to fanout chips employing an indium solder bump flip-chip bonding technology. While quite favorable cw operation characteristics of great consistency throughout the arrays were obtained, small signal modulation along with data transmission remain to be examined. A thermally optimized VCSEL design is to be implemented aiming at significantly lower thermal resistance values. Furthermore, work also has to be done to reduce the divergence angle of the donut-shaped far-field.

5. Acknowledgement

This work is being done in close collaboration with U-L-M photonics GmbH, especially R. King, S. Intemann, and D. Wiedenmann. Funding of this work by the German Research Foundation (DFG) is also gratefully acknowledged by the author.

Cold-Cavity Theoretical Investigation of Transverse Modes in VCSELs with Incorporated Two-Dimensional Photonic Crystals

Pavel S. Ivanov

The theoretical aspect of single transverse mode operation in photonic crystal surface-emitting lasers (PCSELs) is presented. The methodology of mode analysis outlined here is based on the computation of normalized modal propagation constants B which directly defines the number of guided modes. The computed results allow to identify geometrical parameters of photonic crystals enhancing single-mode oscillation and it is shown that such lasers are easily accessible to modern fabrication processes.

1. Introduction

Modern vertical-cavity surface-emitting lasers (VCSELs) operate in a single longitudinal cavity mode. However, they still have one serious drawback which is critical in optical communication systems: in most cases, VCSELs oscillate on multiple transverse modes. This property of the laser cavity incurs increased noise and decreases the coupling efficiency of the connection between VCSEL and some optical fibers. A number of practical approaches to enforce single-mode lasing have been investigated [1]. Perhaps the most interesting and novel method suggests the application of photonic crystals (PCs) for light localization by creating a waveguiding structure in the longitudinal direction of the optical cavity [2]. This is in analogy to holey fibers, where single-mode operation has already been observed [3]. The present contribution focuses on theoretical considerations concerning single-mode operation in VCSELs with incorporated photonic crystals — photonic crystal surface-emitting lasers (PCSELs).

In the most common case, mode analysis is performed by splitting the total field into a transverse and a longitudinal part. Then, the transverse mode properties in the photonic crystal waveguiding structure can be described by estimating the effective value of the normalized frequency parameter V [4] initially introduced for the description of optical fiber modes. A critical problem in this approach is the definition of the effective V value [5], which can lead to several possible V's for the same photonic crystal waveguide.

The topics of this article are the definition and investigation of single-mode conditions resulting from the incorporation of a PC. To avoid the above problem we do not operate with V in the present work. Instead, to define guiding conditions, we calculate the normalized propagation constants B of the guided transverse modes.

2. Numerical Model and Investigated Structure

For simplicity, we chose the relatively simple PCSEL structure with incorporated two-dimensional photonic crystal presented in Fig. 1, which is similar to that in [2]. This structure might be fabricated by dry etching a hexagonal hole pattern in the longitudinal direction of the optical cavity through both mirrors and the active area. The central hole or a group of holes is left out in this pattern and thus conditions for light localization are created. This modification changes the nature of the cavity by including an additional resonance system for the optical field in the laser cavity. In other words, the optical confinement is now composed of the reflection from the mirrors and the effect of the photonic crystal area. By assuming the refractive index of the GaAs semiconductor material to be constant in the considered wavelength range [6] and the refractive index to be constant in the z-direction between mirrors, the electrical field can be separated in longitudinal and transverse parts [7].

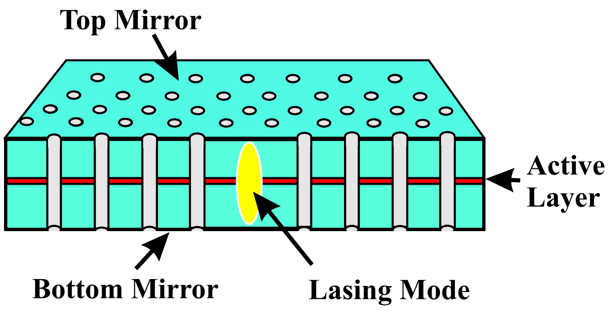

Fig. 1: Investigated layout of a photonic crystal surface-emitting laser.

Based on the aforementioned assumptions, we focus our attention on the transverse field behavior since the photonic crystal provides a periodic index modulation within the transverse plane. Therefore, this modulation mainly affects the transverse part of the j-th optical mode $\psi_j(x,y)$ [3, 7] and the normalized mode propagation constants B_j can be calculated from the solution of

$$\nabla_{\mathrm{t}}^2 \psi_j(x,y) + \left(\bar{n}^2(x,y)\,\frac{\omega_j^2}{c^2} - \beta_j^2\right)\psi_j(x,y) = 0 \ , \tag{1}$$

where

$$B_j = \frac{\beta_j^2 - \beta_{\mathrm{clad}}^2(\lambda)}{\beta_{\mathrm{core}}^2 - \beta_{\mathrm{clad}}^2(\lambda)} \ . \tag{2}$$

In (1), ∇_{t}^2 is the transverse Laplacian, $\bar{n}(x,y)$ is the transverse distribution of the refractive index within the structure, ω_j is the angular frequency of the mode, c is the vacuum velocity of light, and β_j is the respective mode propagation constant. In (2), $\beta_{\mathrm{clad}}(\lambda)$ is the propagation constant in the photonic crystal region (acting as a cladding), which depends on the wavelength λ, and β_{core} is the propagation constant in the core region.

From (2) it follows that B is positive for a guided optical mode. Based on the computation of B we define the number of guided modes in the investigated PCSEL structures. To identify the single-mode regime, we have computed the number of modes for different values of the hole diameter d and the hole pitch Λ. It is assumed that the core region is formed by removing one hole. A group of points where the second mode starts to oscillate has been extracted. All those points define a 'border' line in the d–Λ plane. Such 'border' lines have been computed for two vacuum wavelengths and are displayed in Fig. 2. It is seen that single-mode behavior can be expected for hole diameter to pitch ratios smaller than 0.40 . . . 0.46 depending on pitch and vacuum wavelength.

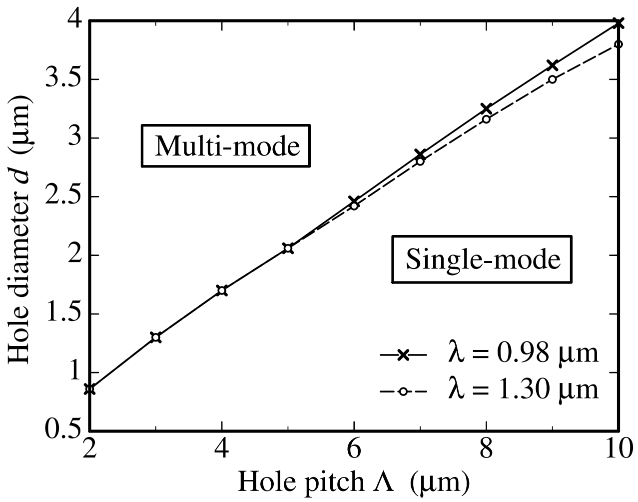

Fig. 2: The 'border' line for single-mode oscillation at 0.98 μm and 1.3 μm wavelength.

The mode behavior has been investigated also for different samples as a function of the vacuum wavenumber $k = 2\pi/\lambda$. Sample data are summarized in Tab. 1. Figure 3 shows the influence of k on the B parameter for samples with different geometrical parameters of the photonic crystal cladding region. All samples demonstrate single-mode operation in the investigated k range, but they have different levels of field penetration into the cladding region. In sample 1 the radiation is concentrated more in the photonic crystal region, and it moves more into the core with increasing hole size or decreasing pitch.

Tab. 1: Geometrical parameters of investigated PCSEL structures.

Sample	Core formed by:	Pitch Λ (μm)	Hole diameter d (μm)	d/Λ
1	one missing hole	3.4	0.75	0.22
2	one missing hole	3.4	1.40	0.41
3	one missing hole	2.0	0.75	0.37
4	7 missing holes	3.4	0.75	0.22

Figure 4 shows the same characteristics for samples 1 and 4 (samples with different core sizes). Sample 1, in which the defect is formed by only one missing hole, shows single-mode behavior over the entire investigated k interval, but laser structure 4, which has a bigger core formed by omitting 7 holes, is multi-mode starting from $k \approx 0.9\,\mu\mathrm{m}^{-1}$. Both the LP_{01} and the LP_{11} mode are concentrated more inside the core region compared to sample 1.

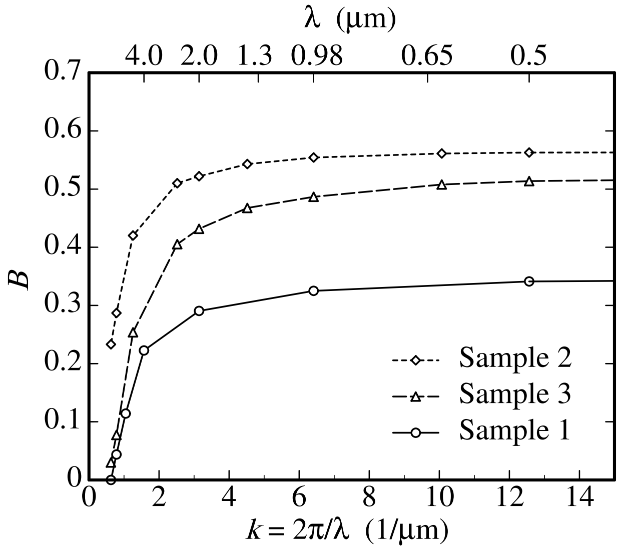

Fig. 3: B–k diagrams for the LP_{01} mode in samples 1 to 3 from Tab. 1.

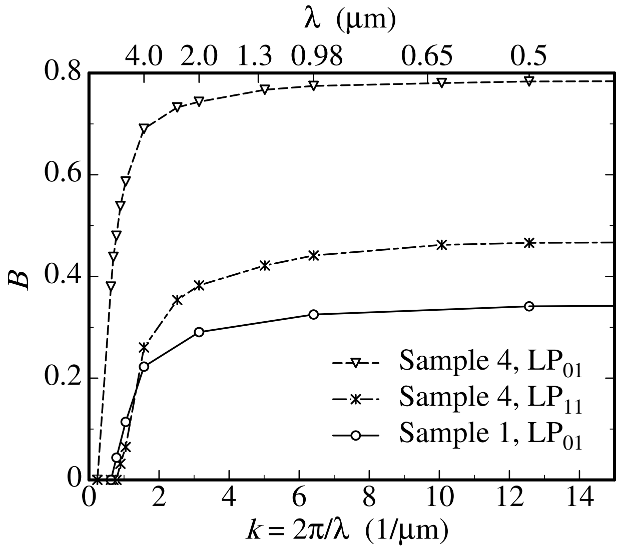

Fig. 4: B–k diagrams for PCSELs with different core size, namely one (sample 1) or seven (sample 4) missing holes.

3. Conclusion

We have theoretically investigated conditions of transverse single-mode operation in vertical-cavity surface-emitting lasers with incorporated two-dimensional photonic crystals. Direct numerical solution of the Helmholtz equation has provided both the effective indices of the modes themselves and those of the photonic crystal region as a function of wavelength. From these data the normalized propagation constant B has been computed, which allowed us to circumvent an estimation of single-mode conditions based on the effective frequency parameter V whose definition is still under discussion.

The results have shown the principal possibility of single-mode emission from PCSELs. Strongly supported fundamental mode guiding is predicted for PCSEL waveguides in which the core is formed by one removed hole. In the investigated structures, the critical parameter for single-mode behavior is the hole diameter to pitch ratio d/Λ in analogy to photonic crystal fibers. Depending on wavelength, single-mode operation is obtained for $d/\Lambda \leq 0.4$ which is the 'border value'. We also expect that single-mode operation in a sample with the core being formed by removing a whole group of holes is possible at a much smaller fraction d/Λ in comparison with a cavity featuring a single center defect.

To achieve transverse single-mode operation, the most promising way seems to be the fabrication of a two-dimensional photonic crystal in the laser cavity with parameters such as $d/\Lambda \approx 0.38$ and a core with just one missing hole. This should provide single-mode guiding together with a maximum confinement level of the LP_{01} mode in the central core region, which is important for a high modal gain. Theoretically, single-mode operation can be achieved even for relatively large diameters of the central region of, e.g., $20\,\mu$m.

References

[1] H.J. Unold, S.W.Z. Mahmoud, R. Jäger, M. Golling, M. Kicherer, F. Mederer, M.C. Riedl, T. Knödl, M. Miller, R. Michalzik, and K.J. Ebeling, "Single-mode VCSELs," in *Vertical-Cavity Surface-Emitting Lasers VI,* C. Lei and S.P. Kilcoyne (Eds.), Proc. SPIE, vol. 4649, pp. 218–229, 2002.

[2] O. Painter, A. Husain, A. Scherer, P.T. Lee, I. Kim, J.D. O'Brian, and P.D. Dapkus, "Lithographic tuning of a two-dimensional photonic crystal laser array," *IEEE Photon. Technol. Lett.*, vol. 12, no. 9, pp. 1126–1128, 2000.

[3] T.A. Birks, J.C. Knight, and P.St.J. Russell, "Endlessly single-mode photonic crystal fiber," *Opt. Lett.*, vol. 22, pp. 961–963, 1997.

[4] P.S. Ivanov, H.J. Unold, R. Michalzik, J. Maehnss, K.J. Ebeling, and I.A. Sukhoivanov, "Single mode conditions in photonic crystal vertical cavity surface-emitting lasers," in Proc. *Workshop on Laser and Fiber-Optical Networks Modelling, LFNM'2002*, Kharkiv, Ukraine, pp. 141–144, 2002.

[5] M. Koshiba, "Full-vector analysis of photonic crystal fibers using the finite element method," *IEICE Trans. Electron.*, vol. E85-C, pp. 881–888, 2002.

[6] E.D. Palik (Ed.), *Handbook of Optical Constants of Solids.* Orlando, FL, USA: Academic Press, Inc., 1985.

[7] J.Y. Law and G.P. Agrawal, "Effects of spatial hole burning on gain switching in vertical-cavity surface-emitting lasers," *IEEE J. Quantum Electron.*, vol. 33, no. 3, pp. 462–468, 1997.

10 Gbit/s Data Transmission Experiments over Optical Backplane Waveguides with 850 nm Wavelength Multimode VCSELs

Martin Stach *

An optical backplane concept based on polymer waveguides, well suited to overcome the communication bottleneck caused by conventional printed circuit boards is investigated. Attenuation coefficients are determined for several waveguides on different backplanes and it is shown that 10 Gbit/s data transmission at a bit error rate of 10^{-12} is possible both for waveguides of large ($250 \times 200\,\mu m^2$) and smaller core size ($100 \times 100\,\mu m^2$).

1. Motivation for Optical Data Transmission

With permanently increasing microprocessor clock frequencies (outreaching 2.5 GHz), this speed enhancement becomes more and more challenging for the periphery. On the high-speed chips themselves parasitics rise with the signal frequency and attenuation increases due to the skin effect,which leads to distortions of pulse shapes and limits transmission lengths. On printed circuit boards, microprocessors are interconnected over relatively great distances, entailing a bottleneck for the outgoing data due to the limited bandwidth-length-product of conventional wire lines. Still using electronic data transmission, one would have to distribute higher data rates to a corresponding number of parallel input and output lines, being followed by a growing terminal density and increasing production costs. However, the main point is that the clock frequency will continue to rise, making high-speed data transmission, e.g. to memory chips, more and more difficult, because the pin density can hardly be increased any further. The use of optical data transmission is one possibility to overcome those disadvantages. Due to photon transmission, one gets a significantly higher bandwidth-length-product, eliminates radio frequency interference, and – with proper design – there are less problems concerning crosstalk, transmission losses and pulse distortion. In ultra-short range optical datacom, distinctions are usually made between inter-rack, inter-board, inter-MCM (multi-chip module), inter-chip and intra-chip interconnection levels [1]. This contribution deals with the characterization of high-bandwidth optical waveguides to be employed in hybrid electrical-optical backplanes for inter-board communications.

*Work performed in collaboration with the DaimlerChrysler Research Center Ulm.

2. Optical Backplane Concept

Polymer waveguide technology can be used for transmitting data via optical waveguides both on one single opto-electronic processor board and for backplane interconnects. One possibility of implementation is the concept of the optical backplane being shown in Fig. 1.

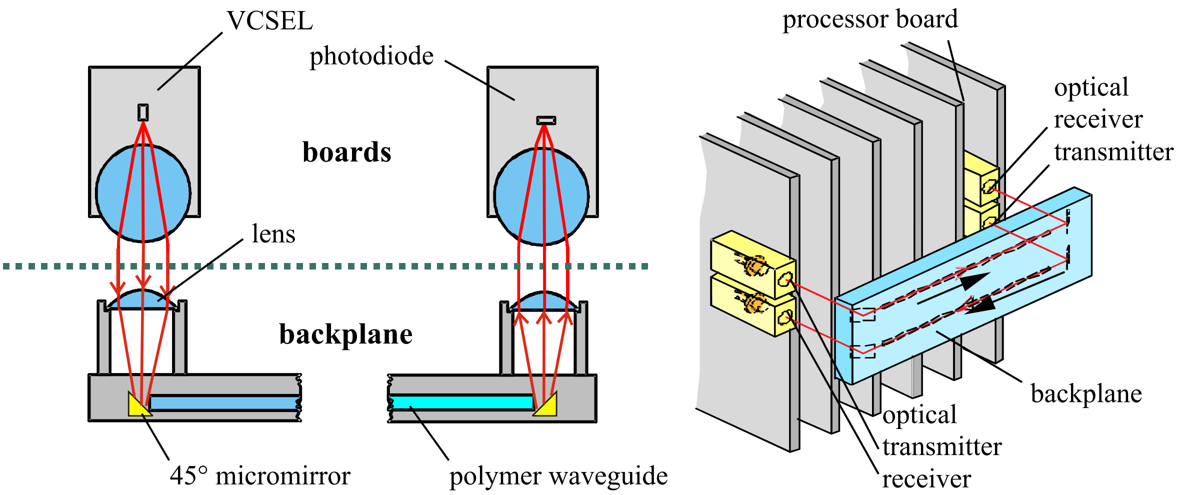

Fig. 1: Concept of the optical backplane developed by DaimlerChrysler and example of implementation [2].

The left part of Fig. 1 depicts the principle of the optical backplane: The main components are at first low-loss polymer waveguides which can be fabricated, e.g. from foil layers on arbitrary substrates (e.g. aluminum) by the hot embossing technique [3] or by laser writing so that the refractive index of the waveguides is increased in comparison to the surrounding material. Next there are integrated highly reflective micromirrors each with a tilt angle of 45°. The transmitter contains a vertical-cavity surface-emitting laser diode (VCSEL), where the divergent light beam is focused on one micromirror via a suitable lens system. On the opposite side the beam leaving the second micromirror has to be guided to a receiver, which contains a large-area but sufficiently fast metal-semiconductor-metal (MSM) photodiode. Using large core multimode waveguides, e.g. $250 \times 200\,\mu\mathrm{m}^2$, with integrated mirrors and lenses, a high alignment tolerance in excess of $\pm 500\,\mu$m for 1 dB loss has been achieved [2], which helps to reduce cost and increase system reliability. VCSELs are ideal transmitters for such short-distance optical interconnects due to several advantages in comparison to edge emitters, in particular circular near field, low beam divergence and inexpensive fabrication. These laser diodes show excellent modulation behaviour, low threshold current, high wallplug efficiency, operation over a wide temperature range and the possibility of heterogeneous integration with electronics and micro-optics.

3. Parameters of the Laser Diode Transmitter

Top-emitting GaAs based 852 nm emission wavelength transverse multimode VCSELs fabricated by solid source molecular beam epitaxy are used for the transmission experiments. An AlAs layer included in the top mirror is selectively oxidized to define a current aperture of 12 μm. As seen in Fig. 2, threshold current and threshold voltage are 1.8 mA and 1.7 V, respectively. The differential resistance at 10 mA current amounts to 60 Ω and the maximum output power at a bias current of 18.3 mA is 7.1 mW. The output spectra for a CW driving current of 9 mA and under modulation with a 10 Gbit/s $2^7 - 1$ pseudo random bit sequence (PRBS) signal are highly multimode and centered around 852 nm. In both cases the root mean square spectral width is less than 0.4 nm. The measured 3 dB bandwidth is 8.6 GHz at 9 mA which makes the device capable for 10 Gbit/s data transmission.

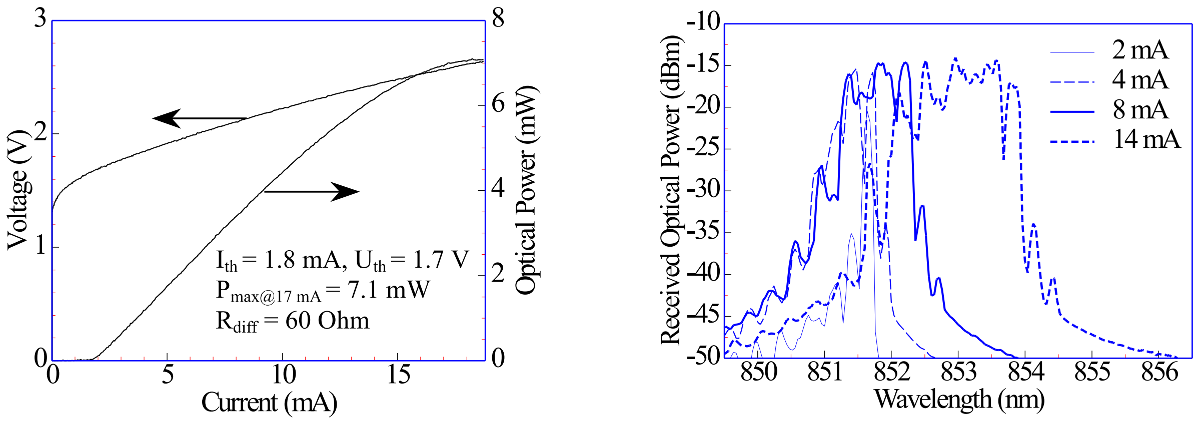

Fig. 2: Operation characteristics of a 850 nm wavelength multimode VCSEL (left) and spectra at CW operation with different bias currents (right).

4. Dimensions of the Optical Backplanes

Three optical backplanes provided by the DaimlerChrysler Research Center have been investigated. The backplane *sample A* has a total width of 12.5 cm and a length of 35.8 cm. The cross-sectional area of the waveguide core is 250 × 200 μm^2. There are four different waveguide types, all with a numerical aperture (NA) of 0.35. Backplane *sample B* has a total length of 191.5 cm and a width of 15.0 cm. As on *sample A*, some of the waveguides are intersecting, and cross-section and NA of all waveguides are as mentioned before. On the backplane itself one can find five different waveguide types. Finally an optical backplane *sample C* with a spiral waveguide was investigated. The core area of this 1 m-long waveguide is only 100 × 100 μm^2, NA is 0.3 and the minimum radius of curvature is about 4 cm.

5. Measurement Results

5.1 Waveguide attenuation

Since the waveguides are optimised for wavelengths around 850 nm, a VCSEL as described in Sect. 3 was used for attenuation measurements. The attenuation is determined with optimum coupling of the VCSEL light via two lenses and with a large-area photodetector placed directly above the output port. Figure 3 shows the attenuation values of the waveguides on backplane *samples A* and *B*.

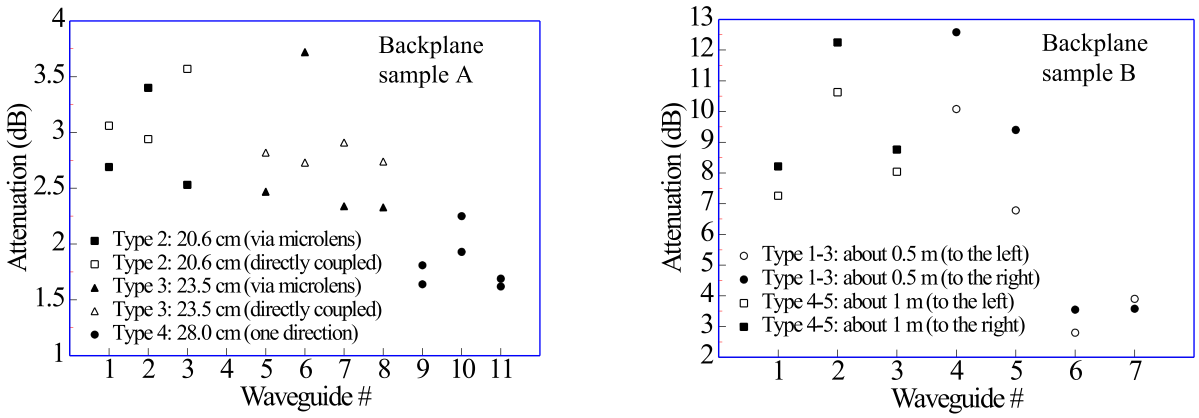

Fig. 3: Attenuation values of waveguides of backplane *sample A* (left) and *sample B* (right) at 850 nm wavelength.

The observations can be summarised as follows:

Sample A: The longest waveguides (type 4) incorporate no bends and microlenses and thus show the lowest attenuation (< 2.25 dB). Assuming an insertion loss of 0.5 dB per mirror [2], the measured minimum attenuation coefficient is as low as 2.2 dB/m.
Sample B: Except for waveguide #7, the attenuation is higher or lower if the light is coupled into the left or right waveguide end, respectively, which can be explained from the mirror fabrication process. The straight waveguide #6 of 50 cm length shows the minimum attenuation of 2.8 dB, which results in an attenuation coefficient of 3.6 dB/m if the insertion loss of two times 0.5 dB is taken into account.
Sample C (spiral waveguide): The attenuation coefficient is the lowest one being measured here because of an improved fabrication process. The attenuation of 3 dB results in an attenuation coefficient of only 2 dB/m. This value is even smaller than the total loss of 5 dB of a comparable 1 m-long spiral with $250 \times 200\,\mu\text{m}^2$ core size [4].

5.2 Digital data transmission

For data transmission the VCSEL was driven at 9 mA bias. Transmission experiments have been carried out with a PRBS non-return-to-zero signal of $2^7 - 1$ word length (peak-to-peak voltage: 0.8 V; Bessel lowpass filter: $f_c = 7$ GHz) at a data rate of 10 Gbit/s.

An InGaAs (p-i-n)-photoreceiver with either 50.0 μm or 62.5 μm multimode fiber (MMF) input was employed, where the larger fiber provides a higher coupling efficiency. The influence of backreflection is negligible with measured average backreflection levels on *sample A* of -15.1 dB and -14.7 dB with and without microlenses, respectively. The mean backreflection levels on backplane *sample B* and on the backplane spiral are -15.7 dB. The eye diagrams are very similar for all experiments, so that the diagram corresponding to the transmission over the backplane spiral is quite representative (Fig. 4). The eye is wide open and essentially does not differ from the recorded eye diagram of the back-to-back (BTB) measurement. In both cases the received optical power is -13.7 dBm entailing a bit error rate of BER $< 10^{-12}$.

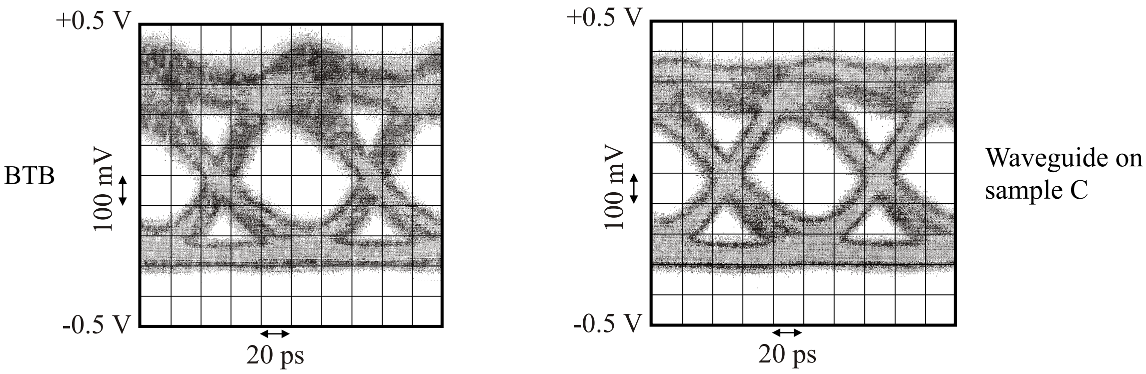

Fig. 4: Eye diagrams recorded for a BER $< 10^{-12}$ at 10 Gbit/s data rate for BTB transmission (left) and over the backplane spiral (right).

In Fig. 5 BER curves are depicted for several different waveguides.

Sample A ($250 \times 200\,\mu\mathrm{m}^2$): The lowest observed power penalty compared to the BTB measurement is 0.3 dB for waveguide #7 (23.5 cm) and for one of the waveguides #9 (28 cm). The required optical power is -14.9 dBm and -15.7 dBm for waveguide #7 and for the straight waveguide #9, respectively.
Sample B ($250 \times 200\,\mu\mathrm{m}^2$): The power penalty is 0.9 dB both for the straight waveguide #6 and for waveguide #7.
Sample C (spiral waveguide, $100 \times 100\,\mu\mathrm{m}^2$): 10 Gbit/s transmission was possible over even 1 m length which is consistent with a bit rate-length-product of more than 10 Gbit/s·m as extracted from small-signal measurements. The power penalty of 1.5 dB is relatively high compared to only 0.5 dB for the $250 \times 200\,\mu\mathrm{m}^2$ spiral in [4].

6. Conclusion

The attenuation and data transmission characteristics of polymer waveguides for optical backplane applications have been investigated. Quasi error-free transmission of a 10 Gbit/s PRBS over 50 cm and 1 m-long waveguides has been demonstrated. The power penalty at a BER of 10^{-12} compared to BTB transmission was 0.9 dB for the larger

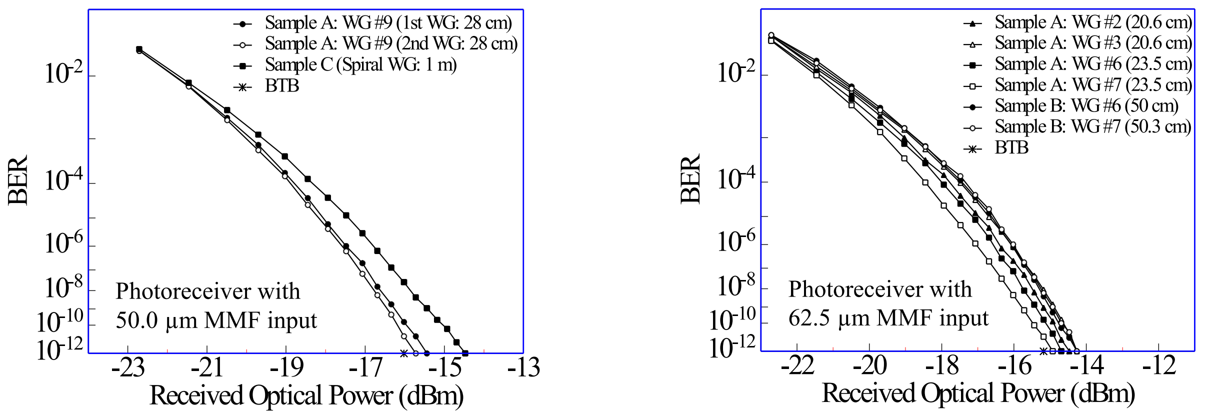

Fig. 5: BER characteristics for $2^7 - 1$ word length PRBS transmission at 10 Gbit/s data rate over several waveguides (WGs), employing two different photoreceivers.

core waveguide and 1.5 dB for the smaller core waveguide. The attenuation of the spiral waveguide has been the lowest one of all measured waveguides and is only about 2 dB/m at 850 nm wavelength. With regard to regular backreflection, no impact on the data transmission characteristics has been observed at measured backreflection levels below -14.7 dB.

References

[1] R. Michalzik, "Optical backplanes, board and chip interconnects," ch. 6 in *Fiber Optic Data Communication: Technological Trends and Advances,* C. DeCusatis (Ed.), San Diego: Academic Press, pp. 216–269, 2002.

[2] J. Moisel, J. Guttmann, H.-P. Huber, O. Krumpholz, and M. Rode, "Optical backplanes with integrated polymer waveguides," *Opt. Eng.*, vol. 39, no. 3, pp. 673–679, 2000.

[3] S. Lehmacher and A. Neyer, "Integration of polymer optical waveguides into printed circuit boards (PCB)," *Electron. Lett.*, vol. 36, no. 12, pp. 1052–1053, 2000.

[4] F. Mederer, R. Michalzik, J. Guttmann, H.-P. Huber, B. Lunitz, J. Moisel, and D. Wiedenmann, "10 Gbit/s data transmission with TO-packaged multimode GaAs VCSELs over 1 m long polymer waveguides for optical backplane applications," *Opt. Comm.*, vol. 206, pp. 309–312, 2002.

Data Transmission with 1.55 μm Wavelength InGaAlAs VCSELs

Felix Mederer, Robert Shau and Markus Ortsiefer *

We investigate high bit rate data transmission behavior of buried tunnel junction single-mode, linearly-polarized InGaAlAs VCSELs for 1.55 μm wavelength. The devices show output powers of 0.73 mW and maximum modulation bandwidths of 5.9 GHz. We demonstrate 5 Gbit/s data rate over 20.5 km standard single-mode fiber as well as 10 Gbit/s for back-to-back transmission.

1. Introduction

Vertical-cavity surface-emitting lasers emitting at 850 nm wavelength are currently used as transmitters for serial and parallel optical links over multimode fibers [1]. The advantages of VCSELs are their high beam quality, longitudinal and transverse single-mode operation, low power consumption and the possibility of array arrangements. Additionally easy on-wafer testing leads to low production and packaging costs. At 1.55 μm wavelength standard single-mode fibers (SSMF) with high bandwidth length products and low optical dispersion and attenuation can be used. Taking into account that the eye safety restrictions at an emission wavelength of 1.55 μm are relaxed by a factor of about 100 compared to 850 nm wavelength [2], the maximum interconnect length can be up 80 km of SSMF [3, 4]. The technological challenges of monolithically grown 1.55 μm wavelength VCSELs are the poor thermal conductivity and low reflectivities of InP-based Bragg mirrors. Additionally a natural oxidation process for current confinement is not yet known. As an alternative to Bragg mirrors active regions on GaAs, metamorphic growth or wafer bonding techniques are conceivable. Using a substrate removal technique and bottom dielectric mirrors in combination with a buried tunnel junction (BTJ) for current confinement, a significant improvement with respect to single-mode power and operation temperature has been demonstrated [5]. In this paper we present the static and significantly improved dynamic characteristics of InGaAlAs-based BTJ-VCSELs emitting at 1.55 μm wavelength. For the first time we demonstrate 5 Gbit/s data transmission over 20.5 km SSMF as well as 10 Gbit/s for back-to-back (BTB) operation. This shows the excellent performance of 1.55 μm VCSELs for Metropolitan Area Network applications.

*The devices have been fabricated at the Walter Schottky Institut, Munich. M. Ortsiefer and R. Shau are now with VertiLas GmbH,Munich.

2. 1.55 μm Wavelength InGaAlAs VCSEL Layout

Figure 1 shows a schematic cross-sectional view of the BTJ-VCSEL.

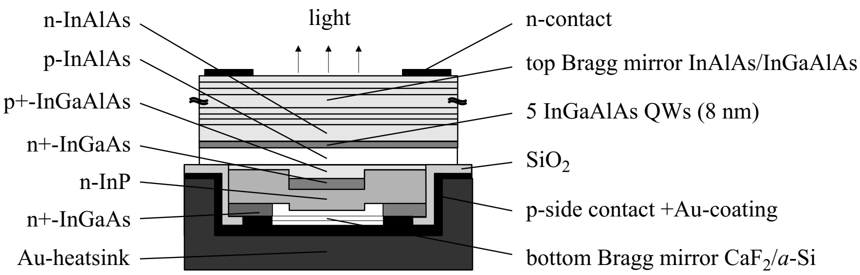

Fig. 1: Schematic layout of 1.55 μm InGaAlAs VCSELs.

The use of the BTJ leads to self-adjusted current confinement as well as optical confinement. Applying highly conductive n-doped spreading layers rather than highly resistive p-doped material, a low series resistances with associated small internal heating is obtained. The front and back mirrors consist of 34.5 pairs of epitaxial InGaAlAs and 2.5 pairs of dielectric CaF_2/a-Si stacks, respectively. The InP substrate on top of the upside-down mounted structure is completely removed. Despite of substrate removal, an electroplated layer at the bottom ensures mechanical stability and additionally acts as an excellent heatsink.

3. Static Characteristics

Figure 2 shows typical room temperature, continuous wave (CW) output characteristics of 1.55 μm BTJ-VCSELs with an elliptic aperture of $3{\times}4\,\mu m^2$.

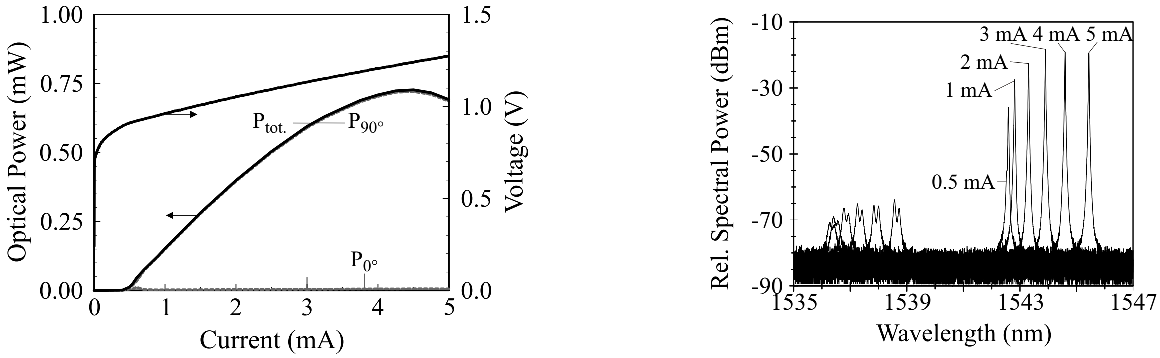

Fig. 2: Operation characteristics of 1.55 μm InGaAlAs-VCSELs with an aperture size of $3{\times}4\,\mu m^2$ (left) and spectra for different driving currents (right).

As shown on the left-hand side of Fig. 2, the maximum output power of this single-mode, single polarization device is 0.73 mW at 4.7 mA. The threshold voltage and threshold current are as low as 0.91 V and 0.4 mA, respectively, while the differential series resistance is 78 Ω. The right-hand side of Fig. 2 shows the high resolution emission spectra of single-mode BTJ-VCSELs under CW operation. It is important to note that single-mode emission with at least 30 dB side-mode suppression-ratio (SMSR) can be observed over the entire current range. Due to internal heating, the peak wavelength shifts from 1542.6 nm at 0.5 mA current to 1545.4 nm at 5 mA.

4. Dynamic Characteristics

The left-hand side of Fig. 3 shows the small-signal frequency responses of single-mode BTJ-VCSELs for various bias currents.

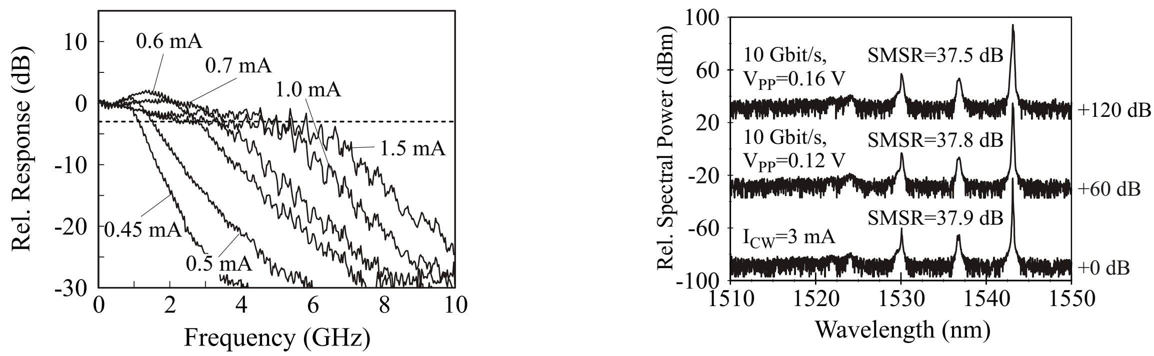

Fig. 3: Modulation response (left) and spectra for CW operation and with 10 Gbit/s modulation (right) of 1.55 μm InGaAlAs VCSELs with an aperture size of $3\times4\,\mu\text{m}^2$.

The maximum measured 3 dB modulation frequency of 5.9 GHz at 1.5 mA is limited by external parasitics, indicating necessary optimizations toward a high-frequency capable electrical VCSEL layout. The right-hand side of Fig. 3 shows the emission spectra for CW operation as well as for 10 Gbit/s modulation with $V_{\text{pp}} = 0.12\,\text{V}$ and $V_{\text{pp}} = 0.16\,\text{V}$. The peak wavelengths for all cases are around 1543.1 nm, and SMSRs of more than 37 dB are observed. The spectral width increases from $\delta\lambda_{\text{RMS,CW}} = 0.0167\,\text{nm}$ for CW operation to $\delta\lambda_{\text{RMS,V}_{\text{pp}}=0.16\,\text{V}} = 0.0567\,\text{nm}$.

5. Data Transmission over Standard Single-Mode Fibers

The 10 Gbit/s eye diagram on the left-hand side of Fig. 4 was recorded for BTB transmission with 3 mA bias current and a modulation with $V_{\text{pp}} = 0.15\,\text{V}$. Even for very high bit rates of 10 Gbit/s, wide openings can be observed. As shown on the right-hand side of Fig. 4, error-free data transmission with bit error rates (BER) of better than 10^{-12} is obtained up to data rates of 10 Gbit/s. For BTB operation at 5, 8 and 10 Gbit/s the minimum received optical power is −18.6 dBm, −15.4 dBm and −11.4 dBm, respectively. The measured power penalty for 5 Gbit/s data transmission over 20.5 km SSMF is about 1 dB, while for 8 Gbit/s over 10.5 km SSMF the power penalty is only 0.4 dB.

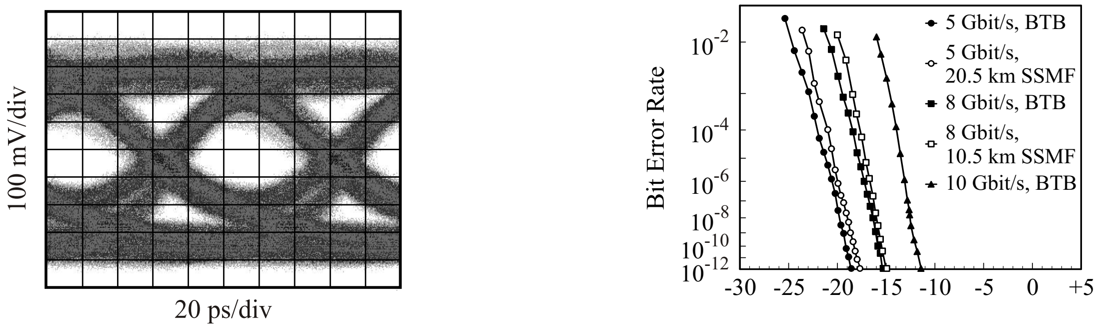

Fig. 4: 10 Gbit/s eye diagram after BTB transmission with 3 mA bias current and a modulation with $V_{pp} = 0.15$ V (left) and bit error rates for 5, 8 and 10 Gbit/s data rates with 3 mA bias current and a modulation voltage of $V_{pp} = 0.15$ V (right).

6. Conclusion

We have demonstrated excellent output performance of single-mode, single polarization BTJ InGaAlAs VCSELs emitting at 1.55 μm wavelength for MAN applications. Measured output power of 0.73 mW as well as a maximum modulation bandwidth of 5.9 GHz makes these VCSELs capable to transmit 5 Gbit/s over 20.5 km SSMF and 8 Gbit/s over 10.5 km SSMF with power penalties of only 1 dB and 0.4 dB, respectively. BTB transmission of 10 Gbit/s was demonstrated for the first time with 1.55 μm VCSELs.

References

[1] Infineon Technologies AG, “Parallel Optical Links (PAROLI),” Jan. 2003. Online: http://www.infineon.com/cgi/ecrm.dll/ecrm/scripts/prod_cat.jsp?oid=-8222.

[2] Berufsgenossenschaft der Feinmechanik und Elektrotechnik, “BG-Vorschriften / Unfallverhütungsvorschriften, B 2, Laserstrahlung,” Berufsgenossenschaft der Feinmechanik und Elektrotechnik, Referat Strahlenschutz, Januar 1993.

[3] 10GE Alliance, “10 Gigabit Ethernet Technology Overview White Paper, Revision 2, Draft A.” 10gea_white_paper_0502.pdf, 10 April 2002. Online: http://www.10gea.org/.

[4] American National Standards Institute, Committee T1, “Synchronous Optical Network (SONET) – Physical Layer Specification (Revision of ANSI 1.106-1988):T1.105.06-1996,” American National Standards Institute, Committee T1X1, Mar. 1996.

[5] R. Shau, M. Ortsiefer, J. Rosskopf, G. Böhm, F. Köhler, and M.-C Amann, “Vertical-Cavity Surface-Emitting Laser Diodes at 1.55 μm with Large Output Power and High Operation Temperature,” *Electron. Lett.*, vol. 37, pp. 1295–1296, Oct. 2001.

Ph.D. Theses

1. Stefan Bader,
   Entwicklung und Charakterisierung einer GaN-basierenden Laserdiode
   Work performed at OSRAM Opto Semiconductors, Regensburg, Germany
   04.03.2002

2. Safwat W.Z. Mahmoud,
   Static and dynamic transverse mode characteristics of vertical-cavity surface-emitting semiconductor lasers
   10.06.2002

3. Michael Miller,
   Aufbautechnik, Leistungsskalierung und Strahlformung oberflächenemittierender Halbleiterlaser
   Mounting technique, scaling of optical output power, and beam shaping of surface-emitting semiconductor laser diodes
   29.06.2002

4. Gunther Steinle,
   Neuartige monolithische InAlGaAsN Vertikallaserdioden
   Work performed at Infineon Technologies AG, München, Germany
   01.07.2002

5. Roland Jäger,
   Molekularstrahleptiaxie hocheffizienter Leucht- und Laserdioden
   29.07.2002

6. Ulrich Martin,
   Emissions- und Alterungsverhalten von transversal einmodigen, kantenemittierenden Halbleiter-Laserdioden
   15.11.2002

Diploma and Master Theses

1. Barbara Neubert,
   Optimierung der Prozesstechnologie zur Herstellung von getaperten InAlGaP Leuchtdioden
   Diploma thesis, Optoelectronics Department, January 2002

2. Hendrik Roscher,
   Prozessentwicklung für die Flip-Chip Montage von Vertikallaserdiodenmatrizen mit Emissionswellenlängen von 850 nm
   Diploma thesis, Optoelectronics Department, March 2002

3. Martin Stach,
   Charakterisierung von optischen Datenübertragungsstrecken mit sichtbaren und infraroten Vertikallaserdioden
   Diploma thesis, Optoelectronics Department, April 2002

4. Eduardo Gomez-Henning,
   Fabrication and characterization of single-mode ridge-waveguide semiconductor lasers
   Master thesis in Communications Technology, Optoelectronics Department, April 2002

5. Michael Furitsch,
   Charakterisierung auf InAlGaP basierender Hochleistungs-Kantenemitter
   Diploma thesis, Osram Opto Semiconductors, July 2002

6. Ferdous Karim Khan,
   Design, fabrication, and characterization of surface-etched polarization-stable single-mode VCSELs
   Diploma thesis, Optoelectronics Department, September 2002

7. Karl Felix Antritter,
   Charakterisierung von optisch gepumpten Halbleiter-Scheibenlasersystemen
   Diploma thesis, Optoelectronics Department, October 2002

Semester Projects

1. Philipp Gerlach,
   Aufbau eines nach der Feedforward-Methode linearisierten Lasersystems
   February 2002

2. Stefan Buntz,
   Aufbau und Inbetriebnahme eines Messplatzes zur Analyse der spektralen Eigenschaften von Vertikallaserdioden unter Großsignalmodulation
   May 2002

3. Martin Fuchs,
   Aufbau eines 10BaseT-kompatiblen Freistrahl-Datenübertragungssystems mit Vertikallaserdioden
   May 2002

4. Peter Brückner,
   Herstellung und Untersuchung von InGaAlP Leuchtdioden mit variierenden Taperwinkeln
   July 2002

5. Lothar Schlafer,
   Berechnung von Eigenwellen in Multi-Mode-Glasfasern mit Gradientenindexprofil
   August 2002

6. Christoph Schleifer,
   Aufbau einer modularen Messeinheit zur Charakterisierung von Vertikallaserdioden
   September 2002

7. Markus Thal,
   Entwicklung und Aufbau eines temperaturgeregelten Heiztisches für die On-Wafer Charakterisierung von optoelektronischen Halbleiterbauelementen
   November 2002

8. Michael Schumann,
   Messungen zur Modenausbreitung in mehrmodigen Glasfasern mit dem Differential-Mode-Delay Verfahren
   December 2002

Talks

[1] F.S. Habel and M. Seyboth, "Defektanalyse von GaN-ELOG Strukturen mit Hilfe von HCl-Ätzprozessen," *17. Workshop Epitaxie von III/V-Halbleitern, DGKK 2002*, Magdeburg, Germany, Dec. 2002.

[2] T. Knödl, M. Golling, A. Straub, R. Michalzik, and K.J. Ebeling, "Multi-stage VCSELs: theory and experiment," *Infineon Technologies*, Munich, Germany, July 2002.

[3] T. Knödl, M. Golling, A. Straub, R. Michalzik, and K.J. Ebeling, "Development and investigation of bipolar cascade VCSELs," *Institute of Quantum Electronics, ETH Zurich*, Zurich, Switzerland, Nov. 2002.

[4] R. Michalzik, I. Kardosh, M. Kicherer, F. Mederer, M. Riedl, H. Roscher, M. Stach, H.J. Unold, and K.J. Ebeling, "VCSEL arrays for high-speed interconnect and high-power applications," *Edith Cowan University, School of Engineering and Mathematics*, Joondalup, Western Australia, Nov. 2002.

[5] R. Michalzik, I. Kardosh, M. Kicherer, T. Knödl, F. Mederer, M. Riedl, H. Roscher, M. Stach, H.J. Unold, and K.J. Ebeling, "VCSEL-related research at the University of Ulm," *Sony Corporation, Atsugi Technology Center*, Kanagawa, Japan, Oct. 2002.

[6] R. Michalzik, I. Kardosh, M. Kicherer, F. Mederer, M. Riedl, H. Roscher, M. Stach, H.J. Unold, and K.J. Ebeling, "Optical interconnect research activities at Ulm University," *Nippon Telegraph and Telephone Corporation, NTT Microsystem Integration Laboratories*, Kanagawa, Japan, Oct. 2002.

[7] R. Michalzik, I. Kardosh, M. Kicherer, T. Knödl, F. Mederer, M. Riedl, H. Roscher, M. Stach, H.J. Unold, and K.J. Ebeling, "Short-wavelength VCSEL applications: datacom and more," *Tokyo Institute of Technology, Precision & Intelligence Laboratory*, Yokohama, Japan, Oct. 2002.

[8] P. Unger, "Halbleiterlaser und optoelektronische Systeme," *Halbleiterkolloquium der Technischen Universität Braunschweig*, Braunschweig, Germany, Jan. 2002.

[9] P. Unger, "Halbleiterlaser und optoelektronische Systeme," *Kolloquium "Optoelektronische Bauelemente" der Technischen Universität Dresden*, Dresden, Germany, Feb. 2002.

[10] P. Unger, "Halbleiterlaser für hohe optische Ausgangsleistung," *Kolloquium "Strahlwerkzeuge" der Universität Stuttgart*, Stuttgart, Germany, Apr. 2002.

[11] P. Unger, "Optisch gepumpte Halbleiter-Scheibenlaser," *Oberseminar des Physikalischen Institutes der Universität Stuttgart*, Stuttgart, Germany, June 2002.

Publications and Conference Contributions

[1] E. Deichsel, R. Jäger, and P. Unger, "High-brightness unstable-resonator lasers fabricated with improved dry-etching technology for ultra-smooth laser facets," *Jpn. J. Appl. Phys.*, vol. 41, pp. 4279–4282, 2002.

[2] E. Deichsel, R. Jäger, and P. Unger, "5 W in a multi-mode fiber from a single 980-nm-emitting laser diode," in Proc. *European Conference on Optical Communication, ECOC 2002*, vol. 3, Copenhagen, Denmark, poster P2.22, Sep. 2002.

[3] E. Deichsel and P. Unger, "Semiconductor unstable-resonator laser diodes for high-power and high-brightness applications," in *Semiconductor Lasers and Applications,* Y. Luo and Y. Nakano (Eds.), Proc. SPIE, vol. 4913, pp. 90–97, 2002.

[4] E. Deichsel and P. Unger, "Dry-etching in optoelectronic device fabrication using chemically-assisted ion-beam etching," in Tech. Digest *Compound Semiconductor Manufacturing Expo, CS-MAX 2002*, San Jose, CA, USA, pp. 29–31, Nov. 2002.

[5] I. Ecker, S. Menzel, J. Joos, I. Kardosh, R. Michalzik, and K.J. Ebeling, "Growth of GaAsSb/GaAs double quantum well lasers emitting near 1.3 μm," in Proc. *44th Electronic Materials Conf., EMC 2002*, Santa Barbara, CA, USA, p. 6, June 2002.

[6] P.S. Ivanov, H.J. Unold, R. Michalzik, F. Mederer, J. Maehnss, K.J. Ebeling, and I. Sukhoivanov, "Theoretical investigation of transverse modes in photonic crystal surface-emitting lasers," in Proc. *4th Int.'l Conf. on Transparent Optical Networks, ICTON 2002*, vol. 2, Warsaw, Poland, pp. 136–139, April 2002.

[7] P.S. Ivanov, H.J. Unold, R. Michalzik, J. Maehnss, K.J. Ebeling, and I. Sukhoivanov, "Application of photonic crystal effective index model for defining single-mode conditions in PCSELs," in Proc. *IEEE Lasers and Electro-Opt. Soc. Ann. Meet., LEOS 2002*, vol. 1, Glasgow, Scotland, pp. 221–222, Nov. 2002.

[8] P.S. Ivanov, H.J. Unold, R. Michalzik, J. Maehnss, K.J. Ebeling, and I. Sukhoivanov, "Single-mode conditions in photonic crystal vertical-cavity surface-emitting lasers," in Proc. *Workshop on Laser and Fiber-Optical Networks Modelling, LFNM 2001*, Kharkov, Ukraine, pp. 141–144, June 2002.

[9] P.S. Ivanov, H. Unold, A.V. Shulika, A.V. Kublik, and I.A. Sukhoivanov, "Light localization in a defect of the photonic crystal," *Radioelektronika i informatika* (in Russian), pp. 42–45, 2002.

[10] P.S. Ivanov, H. Unold, V.V. Lysak, and I.A. Sukhoivanov, "Using photonic crystals in optical communication systems," *Radioelektronika i informatika* (in Russian), pp. 34–37, 2002.

[11] M. Kicherer, A. Fiore, U. Oesterle, R.P. Stanley, M. Ilegems, and R. Michalzik, "Data transmission using GaAs-based InAs-InGaAs quantum dot LEDs emitting at 1.3 μm wavelength," *Electron. Lett.*, vol. 38, pp. 906–907, 2002.

[12] T. Knödl, M. Golling, M. Kicherer, R. Michalzik, and K.J. Ebeling, "Three-terminal dual-stage vertical-cavity surface-emitting laser," *Electron. Lett.*, vol. 38, pp. 278–280, 2002.

[13] T. Knödl, M. Golling, R. Michalzik, and K.J. Ebeling, "Bistability in bipolar cascade VCSELs," *Electron. Lett.*, vol. 38, pp. 370–371, 2002.

[14] T. Knödl, R. Michalzik, M. Golling, and K.J. Ebeling, "Current-spreading-induced bistability in bipolar cascade vertical-cavity surface-emitting lasers," *Appl. Phys. Lett.*, vol. 81, pp. 583–585, 2002.

[15] F. Mederer, I. Ecker, R. Michalzik, G. Steinle, H. Riechert, K.J. Ebeling, B. Lunitz, J. Moisel, and D. Wiedenmann, "VCSEL transmitters for 10-Gigabit Ethernet: 1.3 μm wavelength VCSELs for metropolitan-area-networks and TO-packaged 850 nm wavelength VCSELs for data transmission over multimode fibers and optical backplane-waveguides," in Proc. *52nd Electronic Components & Technology Conference, ECTC 2002*, San Diego, CA, USA, pp. 5–11, May 2002.

[16] F. Mederer, R. Michalzik, J. Guttmann, H.P. Huber, B. Lunitz, J. Moisel, and D. Wiedenmann, "10 Gb/s data transmission with TO-packaged multimode GaAs VCSELs over 1 m long polymer waveguides for optical backplane applications," *Optics Communications*, vol. 206, pp. 309–312, 2002.

[17] R. Michalzik, "Optical backplanes, board and chip interconnects," Chap. 6 in *Fiber Optic Data Communication: Technological Trends and Advances,* C. DeCusatis (Ed.), pp. 216–269, San Diego: Academic Press, 2002.

[18] R. Michalzik, K.J. Ebeling, M. Kicherer, T. Knödl, S.W.Z. Mahmoud, F. Mederer, M. Riedl, H. Roscher, M. Stach, and H.J. Unold, "VCSEL technologies for datacom," in Proc. *3rd Int.'l Conf. on Optics-Photonics Design & Fabrication, ODF 2002,* (invited), Tokyo, Japan, pp. 33–34, Oct. 2002.

[19] R. Michalzik, F. Mederer, H. Roscher, M. Stach, H. Unold, D. Wiedenmann, R. King, M. Grabherr, and E. Kube, "Design and communication applications of short-wavelength VCSELs ," in *Materials and Devices for Optical and Wireless Communications,* C.J. Chang-Hasnain, Y. Xia, and K. Iga (Eds.), (invited), Proc. SPIE, vol. 4905, pp. 310–321, 2002.

[20] D. Mistele, T. Rotter, K.S. Röver, S. Paprotta, M. Seyboth, V. Schwegler, F. Fedler, H. Klausing, O.K. Semchinova, J. Stemmer, J. Aderhold, and J. Graul, "First AlGaN/GaN MOSFET with photoanodic gate dielectric," *Mat. Sci. Eng.*, vol. B93, pp. 107–111, 2002.

[21] D. Mistele, T. Rotter, Z. Bougrioua, I. Moermann, K.S. Röver, M. Seyboth, V. Schwegler, J. Stemmer, F. Fedler, H. Klausing, O.K. Semchinova, J. Aderhold, and J. Graul, "AlGaN/GaN based MOSHFETs with different gate dielectrics and treatments," in Proc. *Mat. Res. Soc. Symp.*, vol. 693, Boston, MA, USA, pp. I6.51.1–I6.51.6, Nov. 2002.

[22] P. Unger, "High-power laser diodes and laser diode arrays," Chap. 2.4 in *Handbook of Lasers, Part B*, 2003, to be published by IOP Publishing.

[23] M. Scherer, B. Neubert, S.S. Schad, W. Schmid, C. Karnutsch, W. Wegleiter, A. Plössl, and K.P. Streubel, "Efficient InAlGaP light-emitting diodes using radial outcoupling taper," in *Light-Emitting Diodes: Research, Manufacturing and Applications VI,* E.F. Schubert and H.W. Yao (Eds.), Proc. SPIE, vol. 4641, pp. 31–41, 2002.

[24] E. Schiehlen, M. Golling, and P. Unger, "Diode-pumped semiconductor disk laser with intracavity frequency doubling using Lithium Triborate (LBO)," *IEEE Photon. Technol. Lett.*, vol. 14, pp. 777–779, 2002.

[25] E. Schiehlen and P. Unger, "Diode-pumped vertical external cavity surface emitting laser," in Proc. *Second Joint Symposium on Opto- & Microelectronic Devices and Circuits, SODC 2002*, Stuttgart, Germany, pp. 104–109, Mar. 2002.

[26] M. Seyboth, S.S. Schad, M. Scherer, F. Habel, C. Eichler, M. Kamp, and V. Schwegler, "Substrates for wide bandgap nitrides," *J. Mat. Sci.: Materials in Electronics*, vol. 13, pp. 659–664, 2002.

[27] M. Stach, F. Mederer, R. Michalzik, B. Lunitz, J. Moisel, and D. Wiedenmann, "10 Gbit/s data transmission experiments over optical backplane waveguides with 850 nm wavelength multimode VCSELs," in Proc. *7th Workshop of Optics in Computing Technology, ORT 2002*, Mannheim, Germany, pp. 47–54, Sep. 2002.

[28] H.J. Unold, S.W.Z. Mahmoud, R. Jäger, M. Golling, M. Kicherer, F. Mederer, M.C. Riedl, T. Knödl, M. Miller, R. Michalzik, and K.J. Ebeling, "Single-mode VCSELs," in *Vertical-Cavity Surface-Emitting Lasers VI,* C. Lei and S.P. Kilcoyne (Eds.), Proc. SPIE, vol. 4649, pp. 218–229, 2002.

[29] H.J. Unold, M.C. Riedl, R. Michalzik, and K.J. Ebeling, "Polarization control in VCSELs by elliptic surface etching," *Electron. Lett.*, vol. 38, pp. 77–78, 2002.

[30] H.J. Unold, P. Debernardi, R. Michalzik, F.K. Khan, and K.J. Ebeling, "Design and modeling of polarization-stable surface-etched VCSELs," in Proc. *18th IEEE Int.'l Semiconductor Laser Conference, ISLC 2002*, Garmisch-Partenkirchen, Germany, pp. 15–16, Sep./Oct. 2002.

[31] S. Barland, J.R. Tredicce, M. Brambilla, L.A. Lugiato, S. Balle, M. Giudici, T. Maggipinto, L. Spinelli, G. Tissoni, T. Knödl, M. Miller, and R. Jäger, "Cavity solitons as pixels in semiconductor microcavities," *Nature*, vol. 419, pp. 699–702, 2002.

[32] B. Corbett, P. Lambkin, J. Justice, E. Deichsel, and P. Unger, "Internal focus 980 nm unstable resonator laser diodes," in Proc. *IEEE Lasers and Electro-Opt. Soc. Ann. Meet., LEOS 2002*, vol. 2, Glasgow, Scotland, pp. 649–650, Nov. 2002.

[33] A. Knigge, M. Zorn, H.J. Unold, F. Mederer, M. Weyers, and G. Tränkle, "High-performance vertical-cavity surface-emitting lasers with emission wavelengths from 650 nm to 670 nm," in Proc. *18th IEEE Int'l Semiconductor Laser Conference, ISLC 2002*, Garmisch-Partenkirchen, Germany, pp. 7–8, Sep./Oct. 2002.

[34] M. Ortsiefer, R. Shau, F. Mederer, R. Michalzik, J. Roßkopf, G. Böhm, F. Köhler, C. Lauer, M. Maute, and M.C. Amann, "High-speed data transmission with 1.55 μm vertical-cavity surface-emitting lasers," in Proc. *28th European Conference on Optical Communication, ECOC 2002,* post-deadline paper PD4.9, Copenhagen, Denmark, Sep. 2002.

[35] M. Ortsiefer, R. Shau, F. Mederer, R. Michalzik, J. Rosskopf, G. Böhm, F. Köhler, C. Lauer, M. Maute, and M.C. Amann, "High-speed modulation up to 10 Gbit/s with 1.55 μm wavelength InGaAlAs VCSELs," *Electron. Lett.*, vol. 38, pp. 1180–1181, 2002.

[36] S. Riyopoulos and H. Unold, "Theoretical interpretation of the enhanced single-mode stability in extended cavity VCSELs," *IEEE J. Lightwave Technol.*, vol. 20, pp. 1173–1181, 2002.

[37] W. Schmid, M. Scherer, C. Karnutsch, A. Plößl, W. Wegleiter, S.S. Schad, B. Neubert, and K. Streubel, "High efficiency, red and infrared light-emitting diodes using radial outcoupling taper," *IEEE J. Select. Top. Quantum Electron.*, vol. 8, pp. 256–263, 2002.

[38] B. Stegmüller, E. Baur, and M. Kicherer, "1.55 μm and 1.3 μm DFB lasers integrated with electro absorption modulators for high-speed transmission systems," in Proc. *Second Joint Symposium on Opto- & Microelectronic Devices and Circuits, SODC 2002*, Stuttgart, Germany, pp. 95–99, Mar. 2002.

[39] B. Stegmüller, E. Baur, and M. Kicherer, "15-GHz modulation performance of integrated DFB laser diode EA modulator with identical multiple-quantum-well double-stack active layer," *Photon. Technol. Lett.*, vol. 14, pp. 1647–1649, 2002.